# INCLUSIVE J/$\psi$ PRODUCTION AT DØ

Christopher R. Murphy

Submitted to the faculty of the University Graduate School
in partial fulfillment of the requirements
for the degree
Doctor of Philosophy
in the Department of Physics,
Indiana University

April, 1995

Accepted by the Graduate Faculty, Indiana University, in partial fulfillment of the requirements for the degree of Doctor of Philosophy.

Daria Zieminska, Ph.D.

John Challifour, Ph.D.

Doctoral Committee

Harold Ogren, Ph.D.

Andrzej Zieminski, Ph.D.

April 25, 1995

This thesis is dedicated
to my Parents
who with loving patience
have waited for this longer than I have

**Acknowledgements**

This thesis would not have been possible if Daria and Andrzej had not caught me "on the way out the door" and been kind enough to offer me a second chance. Together they have been a resourceful, patient, and supportive influence in directing my research efforts. Their knowledge and discipline have been a continual source of inspiration for me. I consider myself lucky to have been able to work with them.

One person I owe an immense thanks to is my erstwhile roommate - Gene Alvarez. At various times Gene provided taxi service, moving service, secretarial service (lip service!), and most importantly friendship. It couldn't have been easy living with a grumpy old man - but Gene never "really" complained. Often he would put important things off for himself just to help me whenever I needed it. He is one of the most generous people I have ever had the pleasure to meet. His few rough edges caused more laughs than friction, and besides I could always count on him to point out a few rough edges of my own! His tireless efforts for the B-Physics group and for the Indiana group in particular made life a lot easier for the rest of us. Thanks for all the help "hermano".

Susumu Igarashi was the person kind and patient enough to help me get started with the real details of my analysis and I thank him for that. I have benefited from the frequent and valuable help of Ken Johns and have always admired his capacity for hard work, his willingness to help, and his many thoughtful criticisms and suggestions. Dan Green and Dave Hedin provided between them an encyclopedic breadth of knowledge and penetrating insight that was available at all times for us struggling grad students and I thank them for all the help they have offered. Kamel Bazizi was always there whenever I needed him and I was lucky enough to benefit from his many helpful suggestions as well. Amber Boehnlein went out of her way to be of asistance on many occasions and was an immense help in getting me started with the trigger simulator.

The entire Arizona group (Dave Fein, Eric James, and Alex Smith) was always willing to share their considerable expertise in many areas and I have benefited greatly from their numerous efforts. Alex Smith especially, was always kind enough to help out in a pinch and provide valuable information whenever it was needed. Similarly Thorsten Huehn was unfortunate enough to be such a helpful font of technical information and friendly advice, that I pestered him on an almost daily basis. Myungyun Pang was extremely helpful in getting me started with his impact parameter analysis package, without which this document might be half its present size! Jim Cochran was a valuable source of help and information on many occasions. Finally, thanks to those many members of the entire DØ collaboration whose considerable efforts made it possible to do analysis at all.

# INCLUSIVE $J/\psi$ PRODUCTION AT DØ

Christopher R. Murphy

*Physics Department, Indiana University*
*Bloomington, Indiana 47405*

**Abstract**

We present results on inclusive $J/\psi$ and $b$-quark production in $p\bar{p}$ collisions at $\sqrt{s} = 1.8\ TeV$. The results are based on data collected at the DØ experiment during the 1992-1993 FermiLab collider run. There is excellent agreement between the differential $J/\psi$ cross section measured at DØ and that measured at the CDF detector. A measurement of the fraction of $J/\psi$ events due to $b$-quark decays is presented and we extract from this a measurement of the integrated $b$-quark cross section. The radiative decays of $\chi_c$ charmonium states into the $J/\psi$ is discussed and we present results on the fraction of $J/\psi$ mesons that are due to $\chi_c$ decays. We also observe that a fraction of promptly produced $J/\psi$ mesons is larger than the measured fraction of $J/\psi$s due to $\chi_c$ decays and is not accounted for by existing charmonium production models.

Daria Zieminska, Ph.D. | John Challifour, Ph.D.

Harold Ogren, Ph.D. | Andrzej Zieminski, Ph.D.

# Contents

# List of Figures

# List of Tables

# Chapter 1

# Introduction

## 1.1 The Standard Model

An impressive number of observations and calculations have compelled physicists to believe that, at present, essentially all of the phenomenology of high energy particle interactions may be successfully described in terms of a physical model referred to as the 'Standard Model'. At its heart, the Standard Model is a Lagrangian Quantum Field Theory based upon the idea of local gauge invariance [1] [2]. The gauge symmetry group of the Standard Model is $SU(3)_C \times SU(2)_L \times U(1)_Y$. $SU(3)_C$ is the symmetry group describing the strong (color) interactions, whereas $SU(2)_L \times U(1)_Y$ represents the symmetry group of the electro-weak sector describing the weak and electromagnetic interactions. The particle content of the model may be broadly classified in terms of two groups, namely the fundamental fermions (spin $\frac{1}{2}$) and the gauge vector bosons (spin 1). The fundamental fermions are in turn subdivided into two parallel classes of particles called quarks and leptons. There are believed to be six different kinds of quarks (referred to as quark flavors: up($u$), down($d$), charm($c$), strange($s$), top($t$), and bottom($b$)), with each type of quark exhibiting a further internal degree of

| Quark Flavor | Quark Charge | Quark Mass (GeV/$c^2$) |
|---|---|---|
| Up | $+2/3$ | 0.002-0.008 |
| Down | $-1/3$ | 0.005-0.015 |
| Charm | $+2/3$ | 1.3-1.7 |
| Strange | $-1/3$ | 0.1-0.3 |
| Top | $+2/3$ | $174. - 199.$ |
| Bottom | $-1/3$ | 4.7-5.3 |

Table 1.1: Properties of Quarks in the Standard Model

| Lepton | Charge | Mass (MeV/$c^2$) |
|---|---|---|
| $\nu_e$ | 0 | $< 7.3 \times 10^{-3}$ |
| $e$ | $-1$ | 0.511 |
| $\nu_\mu$ | 0 | $< 0.27$ |
| $\mu$ | $-1$ | 105.658 |
| $\nu_\tau$ | 0 | $< 35.$ |
| $\tau$ | $-1$ | 1784.1 |

Table 1.2: Properties of Leptons in the Standard Model

freedom called color. Each quark flavor may exist in one of three possible color states. Table 1.1 shows the properties of the quarks as described by the Standard Model.

The leptons come in three different families or generations and include: the electron, the muon, the tau, and their corresponding neutrinos. Table 1.2 lists the known leptons as described in the Standard Model.

The forces between these particles are mediated by the gauge vector bosons. The strong or color force interaction between quarks is described in terms of the gauge particles of $SU(3)_C$. These gauge vector bosons are $3^2 - 1 = 8$ in number and are called gluons. Because the $SU(3)_C$ symmetry of the color interaction is believed to be exact, the gluons are massless particles. However, the non-abelian nature of the color symmetry allows for these gluons to interact among themselves as well as mediate the strong nuclear force between the quarks. This sector of the theory is referred to as Quantum Chromodynamics (QCD) [4]. The strongly interacting particles actually observed in nature are composites of the quarks and are collectively referred to as hadrons. Again, the hadrons are further classified as being either mesons (composed of a quark and an anti-quark) or baryons (comprised of three quarks). Since no free quarks have ever been observed, it is postulated that only color-singlet states ( the composite hadrons) can exist in nature. It is believed (though not yet rigorously proved) that QCD implies this requirement, known as color confinement. The strength of the strong interaction is quantified in terms of the strong interaction coupling constant, $\alpha_s$. Unlike the situation in Quantum Electrodynamics (QED), which is an abelian gauge field theory, an important consequence of the non-abelian nature of QCD is that $\alpha_s$ actually decreases with decreasing distance between strongly interacting partons (a generic term used to refer collectively to the quarks and gluons). This color anti-screening effect is called asymptotic freedom and allows for the possibility of performing reliable perturbative calculations in QCD. Conversely, as the separation between interacting partons increases, $\alpha_s$ also increases, thereby lending support to the conjecture that quarks are permanently bound within the hadrons.

The Electro-Weak sector of the Standard Model is referred to as the Glashow-Weinberg-Salam Model (in honor of the main architects of the theory)[3]. It is a gauge theory that unites the weak and electromagnetic interactions. The gauge symmetry group $SU(2)_L \times U(1)_Y$ requires $(2^2 - 1) + (1^2) = 4$ massless gauge vector bosons. However, in order to describe weak interaction phenomenology, it

| Gauge Boson | Charge | Mass (GeV/$c^2$) |
|---|---|---|
| *gluons* | 0 | 0 |
| $\gamma$ | 0 | 0 |
| $W^{\pm}$ | $\pm 1$ | 80.22 |
| $Z^0$ | 0 | 91.17 |

Table 1.3: Properties of Gauge Bosons in the Standard Model

is required that the vector bosons mediating this force acquire a non-zero mass. This is accomplished through the process of spontaneous symmetry breaking [6], which is implemented via the so-called Higgs Mechanism [7]. The Higgs Mechanism requires the introduction of complex scalar fields. By allowing the scalar field to acquire a non-zero vacuum expectation value, 3 of the 4 gauge vector bosons acquire a mass and these are identified with the $W_\mu^+$, $W_\mu^-$ (mediating charged-current weak interactions), and the $Z_\mu^0$ (mediating the neutral-current weak interactions). The remaining massless gauge vector boson is identified with the photon, $A_\mu$ (mediating the electromagnetic interactions). There remains one neutral scalar field which is called the Higgs Boson. To date, this particle has not been observed experimentally. Table 1.3 presents a summary of the gauge vector bosons involved in the Standard Model.

Although the Standard Model successfully describes many aspects of high energy interactions, it is felt that the model as it stands is still incomplete. Aside from the fact that the Higgs boson has not yet been verified experimentally, the model contains a large number (20) of free parameters. Further, the Standard Model itself does not unite the strong interactions with the weak and electromagnetic in the same way that the Glashow-Weinberg-Salam model has united the weak and electromagnetic forces. The Standard Model exists as an amalgam or juxtaposition of QCD on the one hand, and the electro-weak sector on the other.

There have been many attempts to unite all these forces into one so-called Grand Unified Theory (GUT) [8]. In this sense, the Standard Model is viewed as the low energy manifestation of some more fundamental theory which should take over at much shorter distances (higher energies).

## 1.2 The $J/\psi$

Historically, the $J/\psi$ has played an important role in the development and evolution of the Standard Model. Prior to 1964 particle physicists were attempting to explain the phenomenology of particle interactions in terms of just the lightest quarks $u$, $d$, $s$, and the known leptons - which were arranged into families or generations of left-handed doublets, namely $\begin{pmatrix} \nu_e \\ e^- \end{pmatrix}_L$ and $\begin{pmatrix} \nu_\mu \\ \mu^- \end{pmatrix}_L$. On the basis of aesthetic considerations there was felt the need to have a fourth quark, the charmed quark $c$, in order to maintain a parallelism between the leptons and the quarks. Thus one could construct two quark doublets $\begin{pmatrix} u \\ d_C \end{pmatrix}_L$ and $\begin{pmatrix} c \\ s_C \end{pmatrix}_L$, where the subscript C denoted Cabibbo mixtures of $s$ and $d$ quarks. A more pressing reason for introducing the charmed quark, however, was the need to supress unwanted strangeness-changing neutral currents. The simplest scheme for accomplishing this was developed by Glashow, Iliopoulis, and Maiani and has been referred to as the GIM mechanism [5]. Further, theorists were beginning to realize that the introduction of the charmed quark could also alleviate certain technical problems such as the triangle anomalies which threatened to destroy the renormalizability of gauge theories of the weak interactions. Finally, the ratio $R = \frac{\sigma(e^+e^- \to hadrons)}{\sigma(e^+e^- \to \mu^+\mu^-)}$ showed a rise in the neighborhood of $2m_c$ when plotted versus

$E_{CM}$. If the mass of the charmed quark, $m_c$, was taken to be $\sim 1.5\ GeV/c^2$, and the charge of the charmed quark was taken to be $Q_c = +2/3$, then the predicted value of R was consistent with that observed in the region of charmed threshold pair production.

For all these reasons, the discovery of the $J/\psi$ particle in November of 1974 caused great excitement in the physics community (Indeed, this period has often been referred to as the 'November Revolution'). The $J/\psi$ was immediately interpreted as a bound state of $c\bar{c}$. A bound state of a quark and its corresponding anti-quark is generically referred to as quarkonium. In the case of the $J/\psi$ , the bound system is called charmonium. Two experiments were the first to observe the $J/\psi$. A group at Brookhaven [9] observed it as a narrow resonance in the $e^+e^-$ mass spectrum in the reaction $p + Be \rightarrow e^+e^- + X$. They called it the J particle. A second group at SLAC [10] observed it simultaneously in the reaction $e^+e^- \rightarrow hadrons$. They dubbed it the $\psi$ - hence the dual appelation $J/\psi$. The $J/\psi$ had a very small total width of $\Gamma_{Tot} \sim 67\ keV$ at a mass of $M_{J/\psi} = 3.097\ GeV/c^2$. Because the $J/\psi$ appeared with such a large cross section in the $e^+e^-$ channel, it was natural to suppose that its $J^{PC}$ quantum numbers were $J^{PC} = 1^{--}$, the same as the photon.

Regarding its various decay modes, we note that, as mentioned previously, the $J/\psi$ was interpreted as the first manifestation of a $c\bar{c}$ bound state occuring below the threshold for charmed particle production (hidden charm). The lightest charmed meson, the $D^0$, has a mass of $1.863\ GeV/c^2$ so that the $J/\psi$ lies just below the threshold for decay into $D^0\bar{D}^0$. Therefore, by energy and momentum conservation, the $J/\psi$ can decay hadronically only through OZI suppressed channels. This is thought to be the reason for the small width of the $J/\psi$. These

| | |
|---|---|
| Mass | $3.09693 \pm 0.00009\ GeV/c^2$ |
| $\Gamma_{full\ width}$ | $86 \pm 6\ keV$ |
| $\Gamma_{\mu\mu}$ | $5.36 \pm 0.29\ keV$ |
| $J^{PC}$ | $1^{--}$ |
| $I^G$ | $0^-$ |

Table 1.4: Properties of the $J/\psi$

OZI suppressed decay channels have gluonic intermediate states . Single gluon exchange is not possible because both the initial and final states are color singlets whereas the gluons carry color. Also two-gluon exchange is not possible for a $J^{PC} = 1^{--}$ state since a two-gluon color singlet state must have even charge conjugation parity. The lowest gluonic intermediate state which can couple to a $J^{PC} = 1^{--}$ state is one with three gluons. Thus the dominant hadronic decay channel for the $J/\psi$ proceeds through a 3-gluon intermediate state.

Compared with its hadronic decay width, the leptonic decay width of the $J/\psi$ is rather small, $\Gamma_{l^+l^-} \sim 5.4\ keV$. However the cleanliness of this decay channel at hadron colliders makes it the preferred means of studying the $J/\psi$. In this thesis we shall consider only the leptonic decay of the $J/\psi$ into $\mu^+\mu^-$ pairs.

In terms of spectroscopic notation $(n^{2s+1}L_J)$ the $J/\psi$ is the $1^3S_1$ state of the charmonium system. The charmonium system has a rich spectroscopic structure that is detailed in Fig.1.1. Table 1.4 summarizes the main properties of the $J/\psi$. In table 1.5 we list some of the important branching ratios associated with the $J/\psi$. The data appearing in these tables is taken from the Particle Data Group [11].

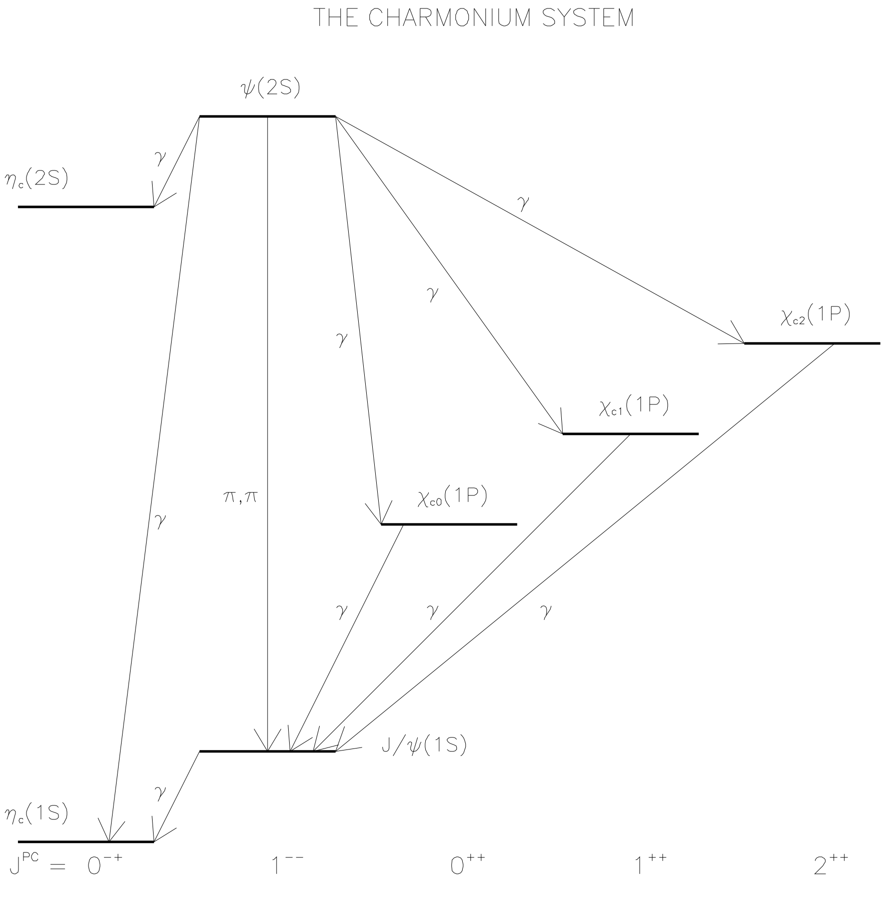


Figure 1.1: Spectroscopy of the Charmonium System

| Process | Branching Ratio |
|---|---|
| $\chi_{c_0} \to J/\psi + \gamma$ | $6.6 \pm 1.8 \times 10^{-3}$ |
| $\chi_{c_1} \to J/\psi + \gamma$ | $27.3 \pm 1.6\%$ |
| $\chi_{c_2} \to J/\psi + \gamma$ | $13.5 \pm 1.1\%$ |
| $B \to J/\psi + X$ | $1.30 \pm 0.17\%$ |
| $J/\psi \to \mu^+\mu^-$ | $5.97 \pm 0.25\%$ |

Table 1.5: Important Branching Ratios associated with the $J/\psi$

## 1.3 Purpose and Outline of this Thesis

During the 92-93 collider run at FermiLab's Tevatron approximately 13 $pb^{-1}$ of data were collected on $p\bar{p}$ collisions at the DØ detector. Out of the approximately 13 million events recorded, it has been determined that about 1000 of these involve $J/\psi$ particles detected through their decays into $\mu^+\mu^-$ pairs. It is the main purpose of this thesis to describe the measurements made on a data sample of dimuon events and to extract from this sample the cross section for inclusive $J/\psi$ production in $p\bar{p}$ collisions at $\sqrt{s} = 1.8\ TeV$.

Chapter 2 discusses the theory of hadroproduction of charmonium with emphasis on the $J/\psi$. Chapter 3 presents the details of the DØ detector used to observe particle production and decay at the Tevatron. In chapter 4 we discuss the specifics of event reconstruction and Monte Carlo simulation. Chapter 5 reviews the different Monte Carlo data sets used in simulations of the various physics processes associated with $J/\psi$ production as well as those processes that constitute the accompanying background. Chapter 6 details the efficiencies involved in $J/\psi$ detection and also discusses the acceptance calculations. Chapter 7 deals with the selection criteria used in obtaining the dimuon data sample that formed the basis for our subsequent measurements and studies, and then presents the analyses that were carried out on the dimuon data sample, and the methods employed in extracting the inclusive $J/\psi$ production cross section. In chapter 8 we present our attempts to separate the various mechanisms that are thought to contribute to $J/\psi$ production. Finally, chapter 9 summarizes the main results of our analysis and presents conclusions that may be validly inferred based upon our study of the data.

# Chapter 2

# Hadroproduction of Charmonium States

## 2.1 Perturbative QCD and the Parton Model

The Parton Model in conjunction with QCD (and the Standard Model) forms the underlying basis for the description and interpretation of essentially all high energy hadronic interactions. The experimental basis for the Parton Model originated in large part from the famous SLAC-MIT deep inelastic scattering experiments of the late 1960's [12].

The essential idea of the parton model is that hadrons are composed of point-like particles called partons, and that within the hadrons these partons behave as essentially free particles. The scattering amplitude of a particle by a hadron is the incoherent sum of the scattering amplitudes of this particle by the individual partons. This picture was developed by Feynman [13]. Within the context of QCD and the Standard Model these partons may be identified with the quarks and gluons. The Parton Model relates physically measureable high energy cross sections between interacting hadrons to theoretically calculable partonic cross sections through a set of parton distribution functions. The latter serve to describe the density distribution of the partons within the interacting hadrons.

If hadron $A$ with momentum $p$ collides with hadron $B$ having momentum $p\prime$ then the parton model cross section for the process in which some desired final state is formed is given by

$$\sigma_{AB}(p,p\prime) = \sum_{ab}\int_0^1 dx_a dx_b \hat{\sigma}_{ab}(x_a p, x_b p\prime) f_{a/A}(x_a) f_{b/B}(x_b) \qquad (2.1)$$

The sum is over all partons of type $a$ and $b$ that contribute to the process for producing the desired final state. Here $x_a$ represents the fraction of momentum of parton $a$ within hadron $A$, and similarly for parton $b$ and hadron $B$. $\hat{\sigma}_{ab}$ is the corresponding cross section for the scattering of partons $a$ and $b$ to produce the chosen final state.

In an analogous fashion, if $C$ represents a final state hadron with momentum $k$, then the hadronic and partonic cross sections are related by

$$d\sigma_C(k) = \sum_c \int_0^1 dz d\hat{\sigma}_c(k/z) D_{c/C}(z) \qquad (2.2)$$

where $D_{c/C}(z)$ is the fragmentation function that describes the probability for parton $c$, with momentum $k^\mu/z$ to produce a hadron $C$ with momentum $k^\mu$ in the final state.

In considering high $p_T$ inclusive single particle production in hadronic collisions, the above formulae may be combined. In the reaction $A+B\rightarrow C+X$ let $p_A$ and $p_B$ represent the momentum of the initial state hadrons $A$ and $B$ respectively. Similarly, let $p_C$ denote the momentum of the observed final state hadron $C$. The invariant cross section for the process may then be written as

$$E_C \frac{d\sigma}{d^3 p_C} = \sum_{abc} \int dx_a dx_b \frac{dz}{z} f_{a/A}(x_a) f_{b/B}(x_b) |\vec{k}_c| \frac{d\hat{\sigma}}{d^3 k_c} (\frac{p_C}{z}) D_{c/C}(z) \tag{2.3}$$

The hard scattering function $|\vec{k}_c|\frac{d\hat{\sigma}}{d^3k_c}$ is for the scattering $a+b \rightarrow c+X$ at the parton level. Again $z$ represents the fractional momentum of the measured final state hadron $C$ relative to its parent parton $c$, that is, $p_C = zk_c$.

To characterize the strength of the hard scattering a parameter $Q$ is introduced such that $Q^2$ represents a scale that is characteristic of the large invariants among $p_A \cdot p_B$, etc..., that describe the interaction. For example, in deep inelastic lepton-hadron scattering $l(k) + h(p) \rightarrow l\prime(k\prime) + X$ we may take $Q^2 = -q^2$ where $q$ represents the spacelike momentum transfer between the lepton and hadron, that is, $q^\mu = k^\mu - k\prime^\mu$.

The above discussion of the Parton Model is referred to as the "Naive Parton Model". In this approximation it is assumed that exact scaling holds. By this it is meant that the stucture and fragmentation functions are independent of $Q^2$. The "QCD Improved Parton Model" takes account of the fact that as $Q^2$ increases, scaling violations begin to occur. The stucture and fragmentation functions now acquire a $Q^2$ dependence. The $Q^2$ dependence of these functions are described by the Altarelli-Parisi evolution equations [14]. In essence these equations serve to represent the radiative corrections which must be introduced due to the constituent quarks and gluons interacting among themselves. If $\Phi_{i/h}(x)$ represents a generic parton distribution or fragmentation function for partons of type $i$ relative to hadrons $h$, then the evolution equations can be written as

$$\mu \frac{d}{d\mu} \Phi_{i/h}(x,\mu) = \sum_j \int_x^1 \frac{d\xi}{\xi} P_{ij}(\frac{x}{\xi}, \alpha_s(\mu)) \Phi_{j/h}(\xi,\mu) \tag{2.4}$$

Here the $Q^2$ dependence has been re-expressed in terms of a "factorization scale" dependence denoted by $\mu$. What has happened is that the parton level scattering cross section $\hat{\sigma}_{ij}$ develops higher order corrections involving logarithms or other sensitive functions of ratios such as $Q/m$. These long distance pieces are removed and factored instead into the parton and fragmentation functions. The factorization scale $\mu$ is an arbitrary parameter, however it is generally chosen to be of the order of the hard scale $Q$ which characterizes the parton-parton interactions. The remaining short-distance cross section $\hat{\sigma}_{ij}$ is so-called "infra-red safe" and is calculable in perturbation theory because of asymptotic freedom. If we know $\Phi_{j/h}(\xi, \mu)$ for $\xi > x$ at some initial scale $\mu = Q_0$, then the evolution equations allow us to calculate $\Phi_{j/h}(x, \mu)$ at a higher scale $\mu = Q$. The evolution kernels $P_{ij}(x)$ are referred to as splitting functions and are given by perturbative expansions in $\alpha_s$.

Regarding $\alpha_s$ we note that higher order corrections also involve Ultraviolet Divergences which must be removed by the usual renormalization procedures. This introduces another arbitrary parameter, namely the renormalization scale parameter $\mu_r$. Observable quantities such as cross sections should not depend on the renormalization subtraction point $\mu_r$. By means of renormalization group techniques all of the characteristic $Q^2/\mu_r^2$ scale dependence of quantities such as cross sections may be expressed in terms of a renormalized or "running" coupling constant $\alpha_s$. For example, at the one-loop level we have

$$\alpha_s(Q) = \frac{\alpha_s(\mu_r)}{1 + \frac{1}{4\pi}[11 - \frac{2}{3}n_f]\alpha_s(\mu_r)\ln(\frac{Q^2}{\mu_r^2})} \tag{2.5}$$

where $n_f$ represents the number of active flavors.

In general the renormalization and factorization scales are taken to be the same, and both are chosen to be of the order $Q$. The above shows that as $Q^2$ increases $\alpha_s(Q)$ decreases. This important property, known as asymptotic freedom, was first recognized by Gross, Wilczek, and Politzer [15] as being a consequence of the non-abelian nature of QCD.

In the remaining sections of this chapter we discuss the hadronic production of charmonium states in terms of the fundamental concepts of QCD introduced above.

## 2.2 Direct Charmonium Production

The "classical" approach to the model of Direct Charmonium Production (CPM) was pioneered by Baier and Rückl [16]. In the CPM model it is assumed that the production of quarkonium states proceeds essentially via a short distance mechanism. The heavy quark and anti-quark are created with transverse separations on the order of $1/p_T$, where $p_T$ denotes the transverse momentum (with respect to the beam direction) of the quarkonium state produced. For sufficiently heavy quarks and for large enough $p_T$ it is assumed that soft gluon and other non-perturbative effects may be neglected. Under these assumptions quarkonium production can be calculated in QCD perturbation theory.

To leading order, contributions to the hard scattering cross sections for quarkonium production come from $\mathcal{O}(\alpha_s^2)$ and $\mathcal{O}(\alpha_s^3)$ processes. In lowest order $\mathcal{O}(\alpha_s^2)$ one has only the gluon fusion process shown in Fig. 2.1. This mechanism produces only low $p_T$ quarkonium states, with the mean $p_T$ determined by the primordial transverse motion of the gluon constituents in the colliding hadrons.

In order $\mathcal{O}(\alpha_s^3)$ one has many more contributing processes, the most important of which are the two-to-two hard scattering diagrams depicted in Fig. 2.2. In these

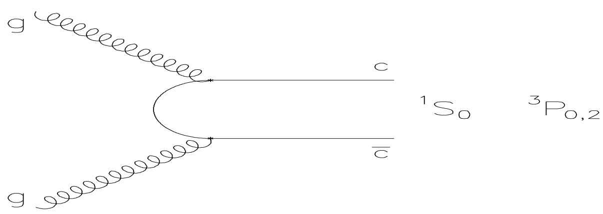


Figure 2.1: Lowest order $\mathcal{O}(\alpha_s^2)$ gluon fusion quarkonium production

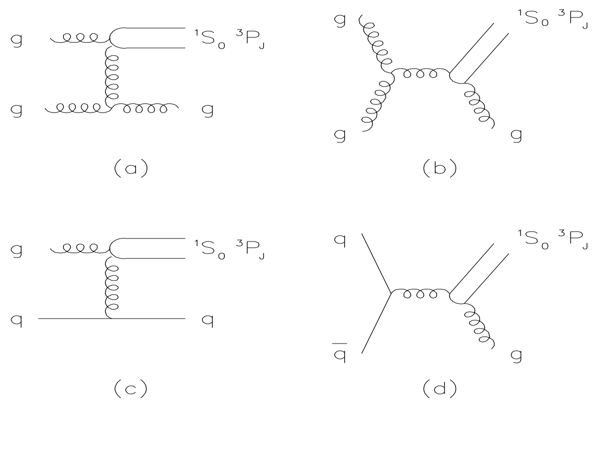


Figure 2.2: Higher order $\mathcal{O}(\alpha_s^3)$ CPM quarkonium production processes

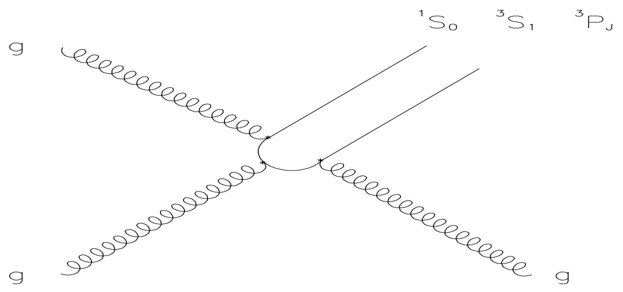


Figure 2.3: Typical CPM $J/\psi$ production process.

processes one has either a quark or gluon recoiling off of the heavy quarkonium resonance thereby leading to higher $p_T$ quarkonium states. Direct production of the $J/\psi$ occurs via the gluon-gluon fusion process shown in Fig.2.3.

The orbitally excited charmonium states, that is the $\chi_c$ states, are the $^3P_J$ states (J=0,1,2). $J/\psi$ states are produced from the $\chi_c$ states via the radiative process $\chi_c \rightarrow J/\psi + \gamma$. This produces soft photons in the vicinity of the $J/\psi$. If one detects the $J/\psi$ via its decay into $J/\psi \rightarrow \mu^+\mu^-$, then $\chi_c$ production may be inferred by looking at the quantity $\Delta \equiv M(\mu^+\mu^-\gamma) - M(\mu^+\mu^-)$. This difference in the invariant masses produces a distribution that is peaked near $\Delta = 0.40\ GeV$ and represents the characteristic energy of the photon produced in the frame of the decaying $\chi_c$.

$J/\psi$'s produced via the CPM mechanism are expected to exhibit an event topology in which there is very little hadronic activity in the vicinity of the $J/\psi$.

In particular, one does not expect to see a significant amount of Jet production in the neighborhood of the $J/\psi$. On the contrary, the only nearby activity is expected to be the presence of soft photons produced in the radiative decay of the $\chi_c$ state. However the detection of such soft photons, especially in the presence of the underlying event, can prove to be quite difficult as the energy spectrum of these photons peaks in the range of about $1-2\ GeV$ due to detector threshold and resolution effects.

To calculate inclusive cross sections for hadroproduction of Charmonium states one must relate the quark-gluon dynamics at the parton level to the corresponding dynamics of the participating hadrons involved in the scattering process. To achieve this we must calculate the amplitude $\mathcal{A}$ for quarkonium production at the parton level and link this quantity with the inclusive hadronic formalism discussed earlier.

Since quarkonium is a bound state of a quark with its corresponding anti-quark, we must relate the amplitude $\mathcal{A}$ for quarkonium production to the amplitude $\mathcal{M}$ for free quark and anti-quark production. Let $Q$ and $\bar{Q}$ denote the heavy quark involved. Assume $m$ is the mass of quark $Q$. In the case of zero binding energy, the mass $M$ of the quarkonium state, represented by $(Q\bar{Q})$, is $M = 2m$. Let $c$ and $d$ represent the 4-momenta of $Q$ and $\bar{Q}$. Suppose we choose a frame in which $c = (\frac{M}{2}, \vec{k})$ and $d = (\frac{M}{2}, -\vec{k})$. Define the pair of variables $p$ and $q$ by $p = c+d = (M, \vec{0})$ and $q = c-d = (0, 2\vec{k})$. Then the amplitude $\mathcal{A}$ for quarkonium production from $Q\bar{Q}$ is given by

$$\mathcal{A}(p) = \int \frac{d^4q}{(2\pi)^4}\mathcal{M}(p,q)\Phi(p,q) \tag{2.6}$$

where $\Phi(p,q)$ is the Bethe-Salpeter wave function of the bound $(Q\bar{Q})$ state produced. The amplitude $\mathcal{M}(p,q)$ for free $Q\bar{Q}$ production in a given initial state is given by

$$\mathcal{M}(p,q) = \bar{u}(\frac{p}{2}+q,s)\mathcal{O}_F v(\frac{p}{2}-q,\bar{s}) = Tr(\mathcal{O}_F v\bar{u}) \tag{2.7}$$

where $u$ and $v$ are the spinors representing $Q$ and $\bar{Q}$, while $s$ and $\bar{s}$ denote their spins respectively. $\mathcal{O}_F$ denotes a generic momentum space spinor operator which must be chosen appropriately for the specific processes that contribute to a given case of free $Q\bar{Q}$ production. In general the spinor operator $v\bar{u}$ is absorbed into the Bethe-Salpeter wave function and the combination is re-expressed in terms of non-relativistic wave functions and appropriate spin-projection operators that represent the various ${}^{2s+1}L_J$ states of quarkonia.

In all of these calculations it is assumed that quarkonium states may be treated in a non-relativistic fashion. The $Q\bar{Q}$ pairs are assumed to form bound quarkonium states with a probability determined by the appropriate non-relativistic bound state wave functions. In this regard various non-relativistic potential models are used to help calculate the wave functions involved. Representative among these is the Cornell Potential Model [19]. From the analogous description of positronium as a bound state, one guesses that at short distances the $Q\bar{Q}$ interaction is approximately Coulombic, while QCD arguments concerning quark confinement suggest that at large distances the interaction potential should rise. Thus the form of the potential for bound $(Q\bar{Q})$ quarkonium is taken to be

$$V(r) = -\frac{\alpha_s}{r} + \frac{\alpha_s r}{a^2} \tag{2.8}$$

This gives rise to a bound state level spectrum broadly similar to that observed for positronium, namely the existence of narrow closely spaced states that are connected by various multipole $\gamma$ radiative transitions subject to certain selection rules which govern the allowed transitions among the various states.

Having obtained the amplitude $\mathcal{A}$ for $Q\bar{Q}$ production the parton level differential cross section for $\mathcal{O}(\alpha_s^3)$ scattering processes are calculated from

$$\frac{d\hat{\sigma}}{d\hat{t}}(ab \rightarrow^{2s+1} L_J c) = \frac{1}{16\pi \hat{s}^2} \sum |\mathcal{A}|^2 \tag{2.9}$$

Calculations of specific amplitudes in this CPM model may be found in Refs.[17] and [18]. The inclusive hadronic cross sections are calculated as convolutions of these short-distance QCD parton level cross sections with the appropriate structure functions that represent the momentum distributions of the parton constituents within the colliding hadrons. For example, the $\mathcal{O}(\alpha_s^3)$ invariant cross section for inclusive hadroproduction of a $Q\bar{Q}$ bound state is given by

$$E\frac{d^3\sigma}{d^3p}(^{2s+1}L_J) = \sum_{ab} dx_a dx_b f_a(x_a) f_b(x_b) \frac{\hat{s}}{\pi}\frac{d\hat{\sigma}}{d\hat{t}}(ab \rightarrow^{2s+1} L_J c)\delta(\hat{s} + \hat{t} + \hat{u} - M^2) \tag{2.10}$$

Fig.2.4 shows the inclusive $J/\psi$ $p_T$ distribution predicted for the various charmonium resonances on the basis of this CPM model [68]. As can be seen from the figure, at sufficiently high $p_T$, charmonium production of $\chi_1$ is expected to dominate, followed closely by $\chi_2$ resonance production. Direct production of $J/\psi$ in the CPM model is expected to contribute only a small fraction to the total charmonium production cross section.

## 2.3 Bottom Production of Charmonium States

In a series of papers in 1979 Fritzsch [20] argued that another significant source of $J/\psi$ production would be the weak decay of B hadrons into $J/\psi$'s and asso-

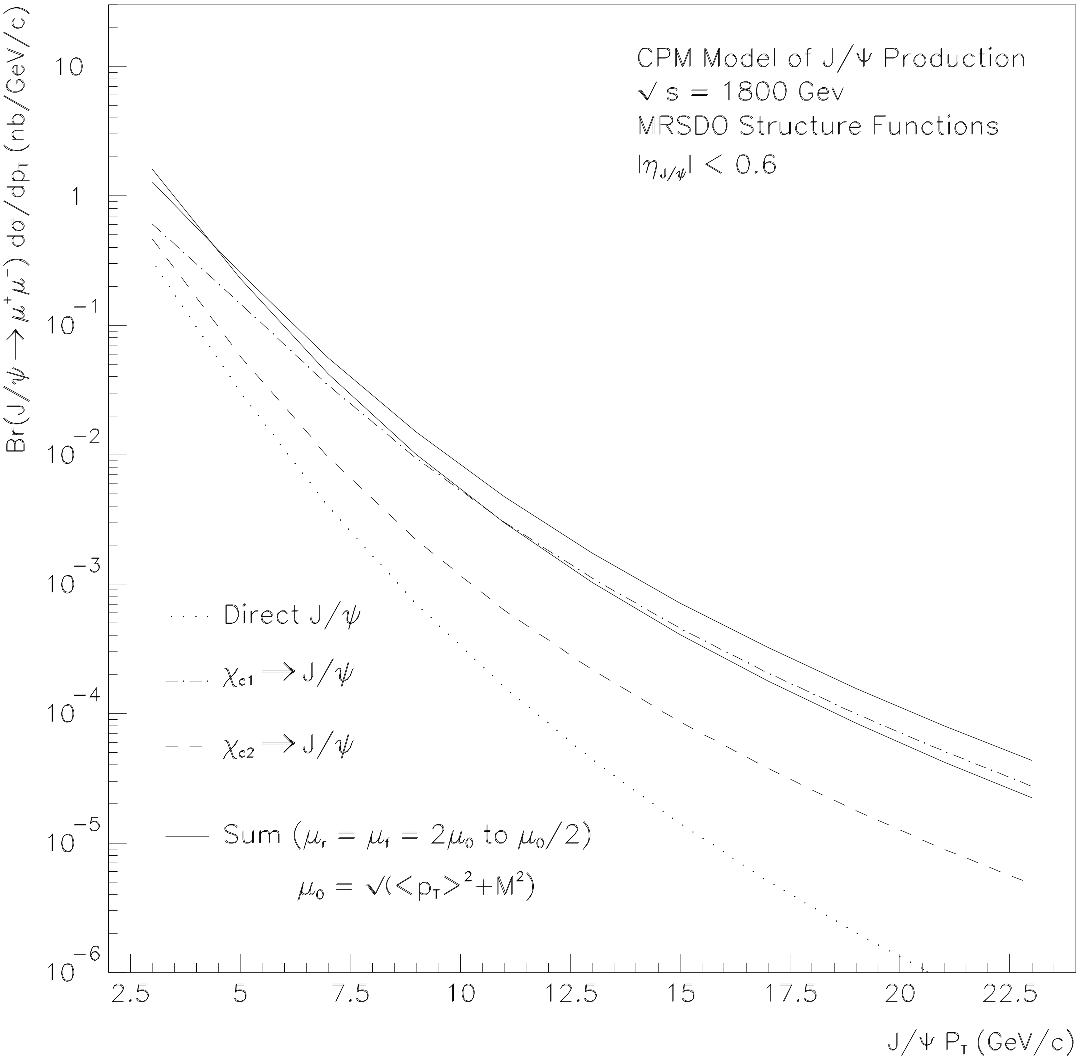


Figure 2.4: CPM model predictions of $J/\psi$ $p_T$ spectra

ciated strange hadronic states. We shall refer to this model of $J/\psi$ production as the BPM (B Production Model) mechanism. As with the CPM mechanism discussed previously, the BPM mechanism is another essentially short distance model. Calculations by Glover, Halzen, Martin and others [21] have shown that hadroproduction of $J/\psi$'s via the BPM mechanism is indeed a significant source of charmonium production at $p\bar{p}$ colliders.

The measured branching ratio of $B \rightarrow J/\psi + X$ is approximately 1.3%. However the cross section for $b$-quark production at $\sqrt{s} = 1.8\ TeV$ is expected to be on the order of 40 $\mu b$. Even allowing for detection of the $J/\psi$ in the muon channel only (branching ratio for $J/\psi \rightarrow \mu^+\mu^-$ is 5.9%), the yield of $b$-produced $J/\psi$'s should be significant because of the large cross section for $b$-quark production. Both UA1 [22] and CDF [23] have measured the cross section for $J/\psi$ production via the BPM mechanism.

The main theoretical constructs that form the basis of the BPM model are:

- QCD calculations of heavy flavor production, in particular, $b\bar{b}$ production
- The spectator or valence quark approximation
- The weak decays of B mesons

Regarding heavy flavor production, we note that a full perturbative QCD calculation to order $\mathcal{O}(\alpha_s^3)$ has been carried out by Nason, Dawson, and Ellis (NDE) [24] and Mangano, Nason, Ridolfi (MNR) [25]. Fig.2.5 shows the MNR prediction for $J/\psi$ production due to the BPM mechanism [68].

Although the fragmentation of the $b$ quark into B mesons represents a non-perturbative effect, a good phenomenological parametrization for heavy quark fragmentation functions has been given by Peterson [26].

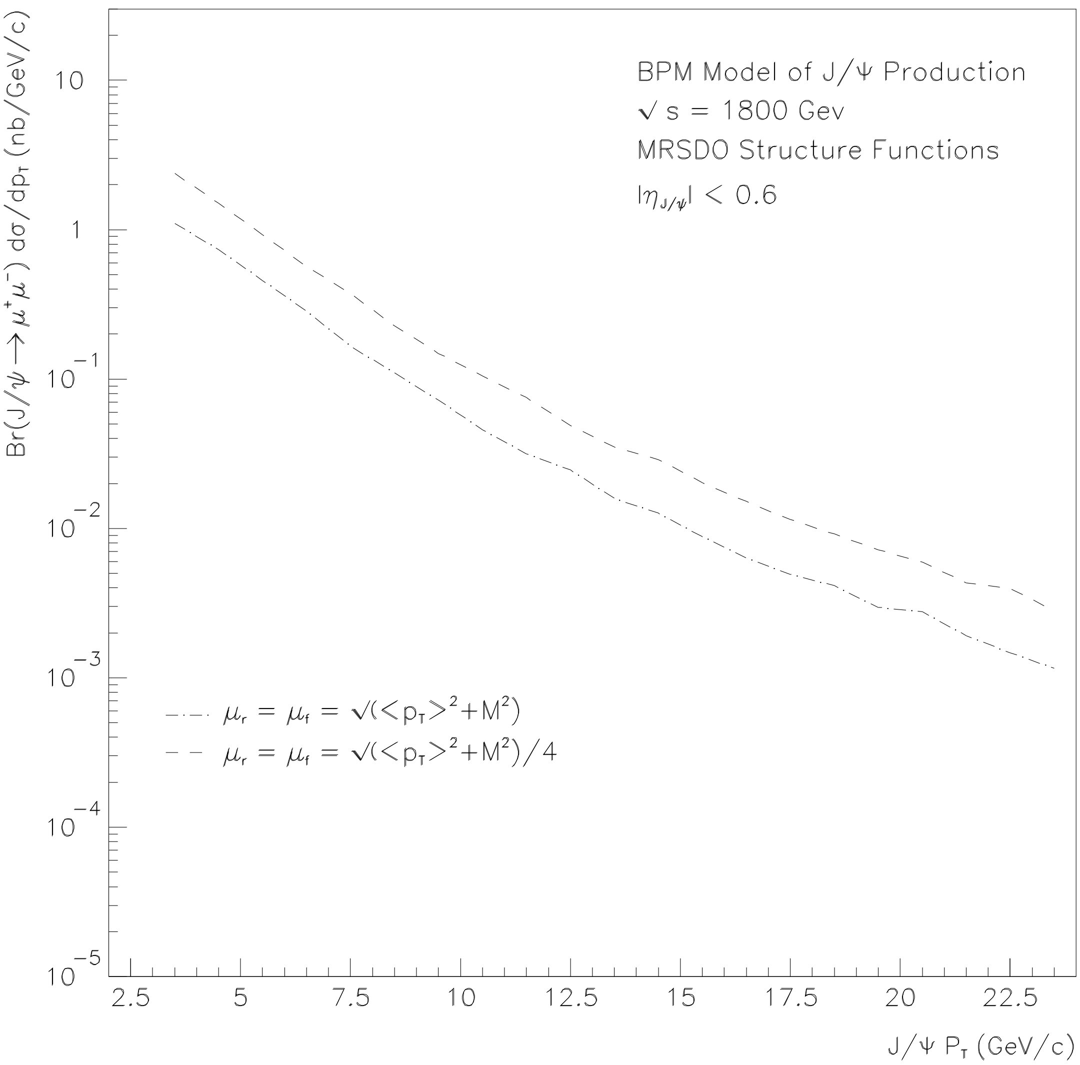


Figure 2.5: BPM predictions for $J/\psi$ production

The spectator approximation is usefull in considering the weak decays of heavy mesons such as the B meson. In these processes the heavy mesons contain a heavy quark and a lighter constituent quark. Because the energy released by the heavy quark when it decays into a lighter quark is much larger than typical quark binding energies, it is assumed that the heavy quark decays independently of the other constituents. Essentially, the lighter quark constituent acts only as a passive spectator. The approximation is expected to become better the heavier the quark.

In the BPM model for $J/\psi$ production we are considering the process $B \rightarrow J/\psi + X$. Since the B meson contains a heavy $b$ quark in addition to a lighter $u$ or $d$ quark (neglecting $B_s$ mesons), we may apply the spectator approximation and view the light $d$ or $u$ quark as merely "going along for the ride". The production of the $J/\psi$ in the non-leptonic weak decay of the B meson may be viewed as an example of an internal type of spectator process, wherein we actually only consider the following quark level process: $b \rightarrow c + W \rightarrow c + \bar{c}s$. The $c$ and $\bar{c}$ quarks combine to form a bound charmonium state, while the left over $s$ quark combines with the spectator $u$ or $d$ (and any other final state quarks) to produce a strange hadronic state denoted by $X$. We may have $X = K, K^{\star}, K\ \pi, K\ \pi\ \pi$, etc. Fig.2.6 shows the process of B-production of the $J/\psi$.

The theory of weak decays of heavy mesons can be described in terms of a short distance QCD-improved effective Lagrangian [27]. The form of the corrected effective weak Hamiltonian responsible for the transition $b \rightarrow c\bar{c}s$ is given by

$$H_{eff} = \frac{G_F}{\sqrt{2}} V_{cb} V_{cs}^{\star} [\frac{c_+ + c_-}{2} (\bar{c}b)(\bar{s}c) + \frac{c_+ - c_-}{2} (\bar{s}b)(\bar{c}c) + h.c.] \tag{2.11}$$

where $(\bar{q}q')$ stands for the color sum $\sum_a \bar{q}_a \gamma_\mu (1 - \gamma_5) q'_a$. $V_{cb}$ and $V_{cs}$ are the appropriate Cabibo-Kobayashi-Maskawa matrix elements. The parameters $c_\pm$ represent

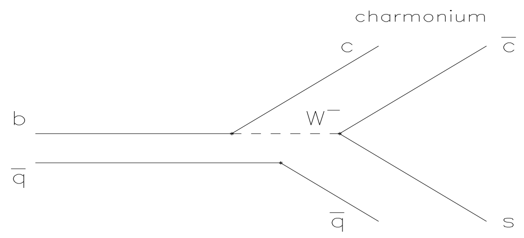


Figure 2.6: Mechanism for B-production of the $J/\psi$

strong interaction corrections brought about by virtual gluon exchanges.

By means of a Fierz transformation one may write

$$(\bar{c}b)(\bar{s}c) = \frac{1}{3}(\bar{s}b)(\bar{c}c) + \frac{1}{2}(\bar{s}\lambda_i b)(\bar{c}\lambda_i c)$$

where the $\lambda_i$ are the usual $SU(3)$ color matrices. Thus we have

$$H_{eff} = \frac{G_F}{\sqrt{2}} V_{cb} V_{cs}^{\star} [\frac{2c_+ - c_-}{3}(\bar{s}b)(\bar{c}c) + \frac{c_+ + c_-}{4}(\bar{s}\lambda_i b)(\bar{c}\lambda_i c)]$$

The matrix element for the decay $b \to [c\bar{c}]s$ is then given by

$$\begin{aligned} < s[c\bar{c}]|H_{eff}|b > &= \frac{G_F}{\sqrt{2}} V_{cb} V_{cs}^{\star} [\frac{2c_+ - c_-}{3} < s|(\bar{s}b)|b >< [c\bar{c}]|(\bar{c}c)|0 > \\ &+ \frac{c_+ + c_-}{4} < s|(\bar{s}\lambda_i b)|b >< [c\bar{c}]|(\bar{c}\lambda_i c)|0 >] \end{aligned}$$

Since the bound $[c\bar{c}]$ state is a color singlet whereas $(\bar{c}\lambda_i c)$ transforms as a color octet, we have that

$$< [c\bar{c}]|(\bar{c}\lambda_i c)|0 >= 0$$

and therefore

$$< s[c\bar{c}]|H_{eff}|b >= \frac{G_F}{\sqrt{2}} V_{cb} V_{cs}^{\star} \frac{2c_+ - c_-}{3} < s|(\bar{s}b)|b >< [c\bar{c}]|(\bar{c}c)|0 > \qquad (2.12)$$

In deriving this matrix element an important assumption was made, namely that of "factorization". A basic problem in non-leptonic B decays is how does one take matrix elements of an effective interaction between final hadronic states. The difficulties revolve around obtaining information about hadronic form factors such as $< H_k|J_\mu(0)|H_p' >$ where $H$ and $H'$ denote some hadrons. In the case of hadronic non-leptonic decays the effective interaction involves the product of two $V - A$ hadronic currents. To compute these matrix elements one assumes the property of factorizability, namely that "the most important contributions to the matrix element come from final state configurations such that the system on one side of the exchanged $W$ does not talk to that on the other"[28]. An example of this approach is given by the estimates for non-leptonic decays of charmed mesons [29]. A general treatment of the Semileptonic and Non-leptonic decays of heavy mesons is given in ref [30].

Concerning the BPM prediction for $J/\psi$ production, we note that the previously discussed matrix element contains the factor $\frac{2c_+ - c_-}{3}$. If short distance QCD corrections are neglected then $c_+ = c_- = 1$. The factor then becomes $\frac{1}{3}$ and thereby expresses the fact that only one in three $c\bar{c}$ pairs is in the desired color-singlet state. The rate of charmonium production in B decays is then expected to be "color-supressed", since the rate is reduced by a factor of $\frac{1}{9}$ [31]. If QCD corrections are taken into account the supression factor becomes even more severe.

To further evaluate the matrix element for B produced $J/\psi$'s we note that the factor $< s|(\bar{s}b)|b >$ may be approximated by the free valence quark expression, that is,

$$< X|(\bar{s}b)|B >=< s|(\bar{s}b)|b >= \bar{u}_s\gamma^\mu(1-\gamma_5)u_b$$

As with the general problem of weak B-decays it now becomes necesarry to evaluate the form factor $< [c\bar{c}]|(\bar{c}c)|0 >=<^{2s+1} L_J|(\bar{c}c)|0 >$. In general, such hadronic form factors are evaluated using Lorentz covariance arguments and dispersion relations. The latter are usually approximated by dominant pole contributions. In the present case however, the form factor can be evaluated using the wave functions of the charmonium model. The following results are obtained for the partial widths $\Gamma(B \rightarrow^{2s+1} L_J + X)$:

$$\Gamma(B \rightarrow^1 S_0 + X) = (\frac{2c_+ - c_-}{3})^2 36\pi \frac{|R_s(0)|^2}{M}\hat{\Gamma}\Phi_1$$

$$\Gamma(B \rightarrow^3 S_1 + X) = (\frac{2c_+ - c_-}{3})^2 36\pi \frac{|R_s(0)|^2}{M}\hat{\Gamma}\Phi_2$$

$$\Gamma(B \rightarrow^3 P_1 + X) = (\frac{2c_+ - c_-}{3})^2 27\pi \frac{|R'_p(0)|^2}{m_c^5}M^2\hat{\Gamma}\Phi_3$$

where

$$\hat{\Gamma} = |V_{cb}|^2|V_{cs}|^2\frac{G_F^2 m_b^5}{192\pi^3}$$

$R_s(0)$ and $R_p\prime(0)$ are the radial S-wave function and the derivative of the P-wave function at the origin. The various $\Phi_i$ $(i = 1, 2, 3)$ represent phase space factors involving the mass $M$ of the charmonium resonance and the effective quark masses $m_b$ and $m_s$. The radial S-wave function $R_s(0)$ may be evaluated from the measured leptonic width $\Gamma(^3S_1 \rightarrow e^+e^-)$. In lowest order one has

$$\Gamma(^3S_1 \rightarrow e^+e^-) = \frac{16\alpha^2|R_s(0)|^2}{9M^2} \approx 4.7\ keV$$

.

| Charmonium State | Interaction | Percentage Yield |
|---|---|---|
| $1^3S_1$ | $B \to J/\psi$ | 80% |
| $2^3S_1$ | $B \to \psi\prime \to J/\psi$ | 13% |
| $1^3P_1$ | $B \to \chi_{c1} \to J/\psi$ | 7% |

Table 2.1: Yields of B-produced Charmonium States in the BPM Model

It should be noted that among the P-wave charmonium resonances, only the $^3P_1$ (that is $\chi_{c1}$) state is accessible via B-decay in the BPM model. The predictions of this model concerning the percentage yield of B-produced charmonium states are summarized in Table 2.1. In total, the estimated branching ratio from the direct and cascade contributions is estimated at

$$Br(B \to J/\psi_{Tot} + X) = 1.6 - 2.4\%$$

QCD corrections for short distance gluon effects could further reduce the above estimate. Best guess estimates for $c_+$ and $c_-$ give values differing from unity and could reduce the branching ratio to $0.3 - 0.5\%$. Further refinements to this prediction [32] suggest a value of $Br(B \to J/\psi_{Tot} + X) = 0.44\%$.

Recent calculations of P-wave charmonium production in B-meson decays [33] suggest that the previous discussion of charmonium production in terms of a "color-singlet mechanism" may be insufficient when considering the production of P-wave charmonium. A second mechanism referred to as the "color-octet mechanism", may be a significant source of $\chi_{c_1}$ and $\chi_{c_2}$ production via B-decays. Here it is argued that there is a probability for a color-octet S-wave $c\bar{c}$ pair to radiate a soft gluon and thereby form a color-singlet P-wave bound charmonium state. These calculations imply a $\chi_{c_2}$ production rate that is comparable to that for $\chi_{c_1}$.

Estimates that include the color-octet mechanism give branching ratios of

$$0.71 \pm 0.20\ \% \quad for \quad J/\psi$$

$$0.50 \pm 0.21\ \% \quad for \quad \chi_{c_1}$$

$$0.46 \pm 0.20\ \% \quad for \quad \psi\prime$$

The Argus collaboration [34] has recently measured the branching ratio to be $Br(B \rightarrow \chi_{c_1} + X) = 1.05 \pm 0.35 \pm 0.25\ \%$

Concerning the recoiling hadronic state X, one expects that at the $J/\psi$ the mass of the recoiling hadronic system is

$$M_X = [M_B(M_B - m_b + \frac{m_s^2}{m_b}) + M_\psi^2(1 - \frac{M_B}{m_b})]^{1/2} \approx 0.7 - 1.2\ GeV/c^2 \quad (2.13)$$

Thus low multiplicity final hadronic states are expected to dominate. In contrast to $J/\psi$'s produced via the CPM mechanism, one therefore expects B-produced $J/\psi$'s to be non-isolated and accompanied by hadronic states that have an enhanced strangeness content.

Since the $J/\psi$ is a vector resonance one can expect some effects due to the polarization of the $J/\psi$. If $\theta$ is defined as the angle between the lepton momentum in the $J/\psi$ rest frame and the direction of flight of the $J/\psi$ in the B rest frame, then the lepton angular distribution is of the form

$$\frac{dN}{d\cos(\theta)} = 1 + A\cos^2(\theta) \quad (2.14)$$

Here $A$ is given by

$$A = \frac{1 - 3\frac{N_L}{N}}{1 + \frac{N_L}{N}}$$

where $\frac{N_L}{N}$ represents the relative number of longitudinally polarized $J/\psi$'s. The BPM model (color-singlet) predicts $A = -0.17\ to - 0.27$ and therefore suggets a fairly flat distribution of lepton pairs from the leptonic decay of the $J/\psi$.

## 2.4 Parton Fragmentation into Charmonium States

The CPM model discussed previously implies that the dominant contribution to the direct production of charmonium states at high $p_T$ comes from leading order gluon-gluon fusion diagrams. The observation by CDF of a higher than expected inclusive $J/\psi$ yield at $\sqrt{s} = 1.8\ TeV$ has prompted theorists to re-examine the process of direct charmonium production [35]. New calculations suggest that there is a fragmentation contribution to charmonium production. Here it is envisioned that a high $p_T$ quark or gluon fragments or decays into a charmonium state and other partons. In the fragmentation mechanism, the heavy $Q\bar{Q}$ pair is created with a separation of the order of $1/m_Q$. Generally the fragmentation contributions involve higher orders of the QCD coupling constant $\alpha_s$. However at sufficiently high $p_T$ the fragmentation mechanism should dominate over the short-distance mechanism because the latter models assume the heavy quark pairs are created with transverse separations of order $1/p_T$ and they are supressed by powers of $m_Q/p_T$. Fig.2.7 shows a schematic of the fragmentation mechanism.

The fragmentation process is described in terms of fragmentation functions $D(z)$ which give the probability for the splitting of a high $p_T$ parton into a hadron with longitudinal momentum fraction $z$. The calculations alluded to earlier show that fragmentation functions for the production of heavy quarkonium states can actually be calculated using perturbative QCD. These functions are called perturbative fragmentation functions (PFF's). The differential cross section for $J/\psi$ production via fragmentation can be written in a factorized form as

$$d\sigma(p\bar{p} \to J/\psi(p_T) + X) = \sum_i \int_0^1 dz d\sigma(p\bar{p} \to i(\frac{p_T}{z}) + x, \mu) D_{i\to J/\psi}(z, \mu) \quad (2.15)$$

where a sum over partons of type $i$ is included. $D_{i\to J/\psi}(z,\mu)$ is the PFF for partons of type $i$ to fragment into the $J/\psi$. The factorization scale parameter is denoted by $\mu$. The PFF's may be evolved to any scale via the Altarelli-Parisi evolution equations

$$\mu\frac{\partial D_{i\to J/\psi}(z,\mu)}{\partial\mu}=\sum_j\int_z^1\frac{dy}{y}P_{i\to j}(\frac{z}{y},\mu)D_{j\to J/\psi}(y,\mu) \tag{2.16}$$

The fragmentation functions $D_{g\to J/\psi}(z,\mu)$ and $D_{c\to J/\psi}(z,\mu)$ as well as $D_{g\to\chi_{c_J}}(z,\mu)$ and $D_{c\to\chi_{c_J}}(z,\mu)$ have been calculated to leading order in $\alpha_s$ [36].

An estimate of the crossover point in charmonium $p_T$, above which fragmentation dominates has been given as being on the order of $4m_c$ to $6m_c$. Thus, above $p_T$'s of about 6 $GeV/c$ one would expect the fragmentation mechanism to dominate over short distance mechanisms. Fig.2.8 shows the predictions for $J/\psi$ production via the fragmentation process [68].

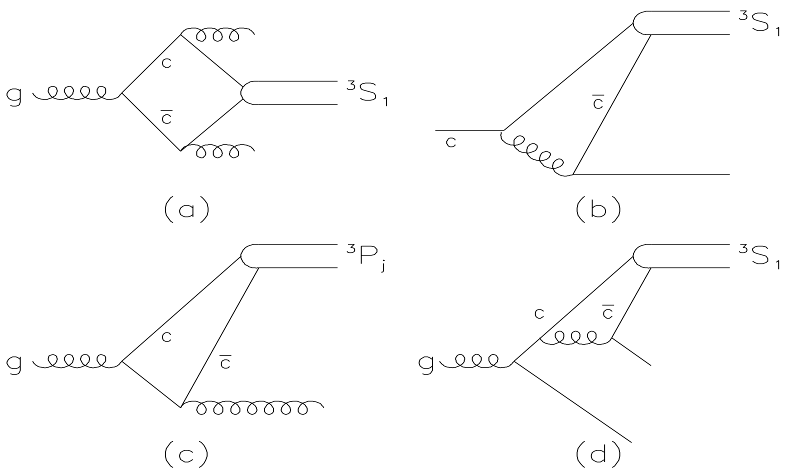


Figure 2.7: Fragmentation mechanism for production of Charmonium

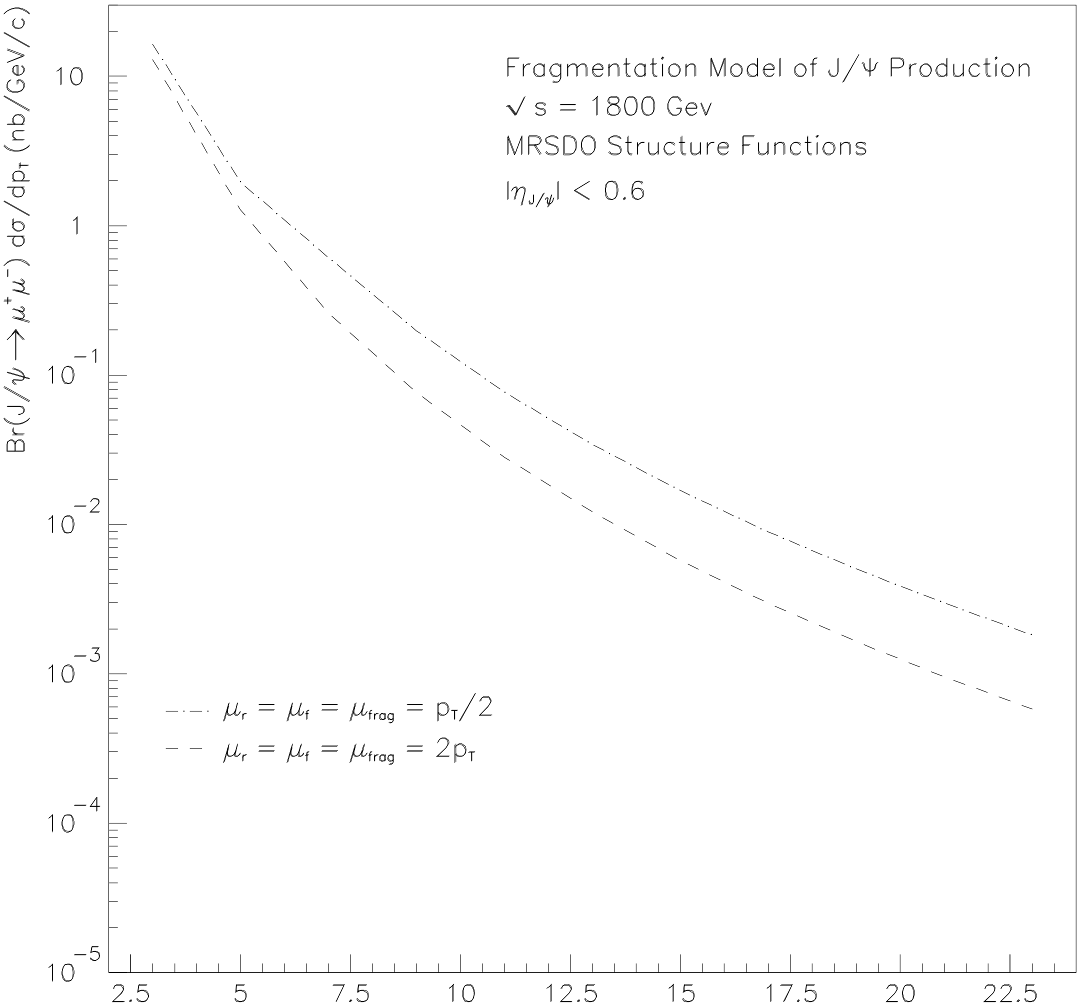


Figure 2.8: $p_T$ spectrum for $J/\psi$ production in the Fragmentation Model.

# Chapter 3

# The DØ Detector

## 3.1 The Tevatron

FermiLab's Tevatron is, at present, the world's largest particle accelerator. Its basic function is to collide protons and anti-protons at a center of mass energy of 1.8 TeV [37].

The Tevatron consists of a collection of various accelerators and other machines designed to work together to produce a stable particle beam of circulating protons and anti-protons that are brought together at specific places around the Tevatron ring to produce the desired $p - \overline{p}$ collisions.

The basic components of the Tevatron complex are: (1) A Cockroft-Walton Pre-Accelerator, (2) The Linac ( Linear Accelerator ), (3) The Booster Synchrotron, (4) The Main Ring Accelerator, (5) The Pbar Storage Rings ( Debuncher and Accumulator complex ), (6) The Tevatron Ring. Fig.3.1 shows the basic elements of the FermiLab Tevatron Collider Complex.

The beam begins as a small tank of Hydrogen gas. Electrons are added to the hydrogen atoms thereby producing hydrogen ions $H^-$. The $H^-$ ions are introduced into the Pre-Accelerator which, by means of static electric fields, accelerate the

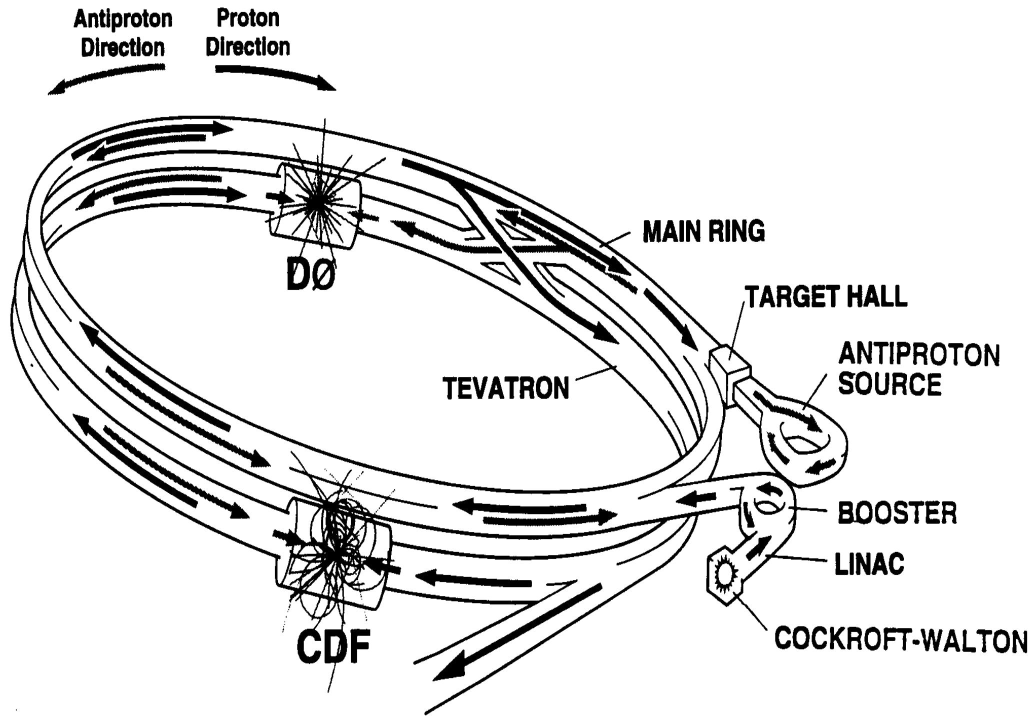


Figure 3.1: FermiLab's Tevatron Collider.

ions up to an energy of 750 keV. Upon exiting the Pre-Accelerator, transport lines direct the $H^-$ ions into the 150 m long Linac. Within the Linac a series of 9 RF 'tanks' accelerate the ions up to 200 MeV. Quadrupole magnets are used to help focus the beam. After leaving the Linac the ions are then made to pass through carbon foil. The latter acts to effectively remove all the electrons from the $H^-$ ions, thus leaving only the hydrogen nuclei or protons. At this point the protons are steered into the Booster Accelerator. The booster is a 151 m diameter synchrotron. Within the synchrotron the protons pass through a series of 18 RF cavities spaced around the ring. As the protons pass through the cavities they accelerate. Magnetic fields produced by focusing and bending magnets act to keep the protrons circulating in a stable orbit. As the RF frequencies are raised to produce higher momentum protons, the currents in the magnets must also be raised in a synchronous fashion in order to hold the protons within a stable orbit (since $p = qB\rho$ ; where $p$ = proton momentum, $q$ = proton charge, $B$ = magnetic field, and $\rho$ = radius of curvature). At the end of the acceleration cycle the protons exit the booster with an energy of 8 GeV. The beam is extracted and then transferred to the Main Ring.

The Main Ring is a synchrotron with a diameter of 2 kilometers. More than 1,000 copper/coiled bending and focusing magnets are used to provide confinement and stability. Dipole magnets are used to keep the proton beam steered into a circular orbit. Quadrupole magnets focus the beam into short bunches with a small cross-sectional size. The Main Ring accelerates the protons from 8 GeV to 150 GeV again using RF electromagnetic fields. The proton bunches are extracted from the Main Ring and directed against a nickel/copper target. This produces approximately 20 million anti-protons per bunch. The anti-protons are then injected into the Pbar storage rings.

The function of the Pbar storage rings is to squeeze the initially incoherent anti-proton beam into as compact a phase space as possible. The Pbar storage rings are comprised of the Debuncher and the anti-proton Accumulator. At first, the anti-protons exhibit large variations in momentum. Many oscillate in directions transverse to the desired beam orbit. Within the Debuncher a process known as stochastic cooling is used to achieve a nearly uniform momentum distribution of the anti-protons and to reduce as much as possible their oscillations transverse to the designed beam orbit. This cooling process is accomplished by sensors which are able to detect anti-protons whose orbits are not ideal. Correction signals are then sent to kicker electrodes that serve to restore the errant particles to their proper trajectories. After this initial cooling process approximately 20 billion anti-protons are sent into the anti-proton Accumulator. Further cooling takes place and the density of the anti-protons is significantly increased. After a period of 4 to 6 hours the continuous accumulation of anti-protons results in a 'store' of about 200 billion anti-protons. This is sufficient to set up a 'shot' into the Main Ring.

As with the protons, the anti-protons are accelerated in the Main Ring (travelling in a direction opposite to that of the protons) up to an energy of 150 GeV. From the Main Ring both protons and anti-protons are injected into the Tevatron (still travelling in opposite directions). The Tevatron is located within the same beam tunnel enclosure as the Main Ring, about 2 feet below it. Superconducting magnets are cooled to a temperature of 4.8 degrees Kelvin by means of a liquid Helium cooling system. In this way the magnets are able to create much stronger magnetic fields and therefore allow for the acceleration of particles to much higher energies. Six bunches of protons and six bunches of anti-protons (approximately $6 \times 10^{10}$ particles per bunch) are accelerated by RF from 150 GeV to 900 GeV. Once the desired final energy of 0.9 TeV is reached for both the proton and anti-proton bunches, the two beams are brought together at two beam-crossing stations designated as BØ (CDF) and DØ . A special group of quadrupole magnets (low-beta quadrupoles) are used to reduce the cross-sectional area of the beams at these points to about $1mm^2$. Beam crossings take place about once every 3.5 $\mu$s. Due to scattering with residual beam gasses and beam-beam interaction effects, the density of the beams slowly decreases with time. Beam lifetimes are on the order of 20 hours. However, during this time the anti-proton accumulator remains continually active so that a new 'stack' of anti-protons is available when the next 'shot' is needed. Stacking rates of $4.54 \times 10^{10}$ /hour have been achieved at the Tevatron. Typical luminosities are about $5 \times 10^{30} cm^{-2} s^{-1}$ which produce, on average, about 0.75 interactions per crossing.

## 3.2 Introduction to the DØ Detector

The DØ detector was constructed to study proton-antiproton collisions at $\sqrt{s} = 2$ TeV [38]. It is located at the beam-crossing station DØ on the FermiLab Tevatron collider ring - hence the Detector's name. The main purpose in constructing the detector was to be able to study high-mass states and high $p_T$ phenomena. Primary Physics interests center on the search for the top quark, W and Z production and decay, production of b-quark hadrons, the search for SUSY particles, and various tests of perturbative QCD.

To facilitate and enhance the study of these primary physics goals the DØ detector was designed with the following capabilities in mind:

- Good identification and measurement of electrons and muons.
- Highly segmented calorimetry with good energy resolution for the measurement of high $p_T$ parton jets.
- Good determination of missing $E_T$.

In order to achieve these measurement capabilities the following design criteria were implemented:

- Thick, magnetized iron absorbers for good momentum measurement of muons. The dense toroids also serve to minimize hadronic punchthrough.

- Nearly hermetic, finely segmented, liquid argon calorimetry.

- Compact, non-magnetic inner tracking volumes with good spatial resolution and suppresion of backgrounds to electron identification.

A cutaway view of the DØ detector is shown in Fig.3.2. As the figure makes evident, the detector has been constructed as a succession of nested shell-like components. The overall detector architecture is composed of three primary detector sub-systems. These sub-systems consist of an inner tracking system, surrounded by the calorimeter system, which in turn is surrounded by the muon system.

The inner tracking system consists of four different detector components. The central portion of this system is comprised of the vertex detector (VTX), the transition radiation detector (TRD), and the central drift chamber (CDC). These components form a nested series of concentric cyclinders which surround the beam pipe and cover the central pseudorapidity region $|\eta| < 1.2$. Pseudorapidity is here defined as $\eta = -\ln(\tan\frac{\theta}{2})$, where $\theta$ is the polar angle measured from the beam axis. The pseudorapidity range $1.4 < |\eta| < 3.1$ is covered by the forward and backward drift chambers (FDC). The tracking system does not have a central magnetic field associated with it.

The DØ calorimeter is of the sampling variety and is based upon the use of uranium/liquid argon (LAr) calorimetry. It consists of three major components. The central calorimeter (CC) covers the pseudorapidity range $|\eta| < 1.1$, and the end calorimeters (EC) cover the region $1.1 < |\eta| < 4.5$.

Outermost in this nested structure of hardware components is the DØ muon system. It encloses all the other detector subsystems. The muon system consists of three layers of chambers and five toroids. The innermost layer is called the

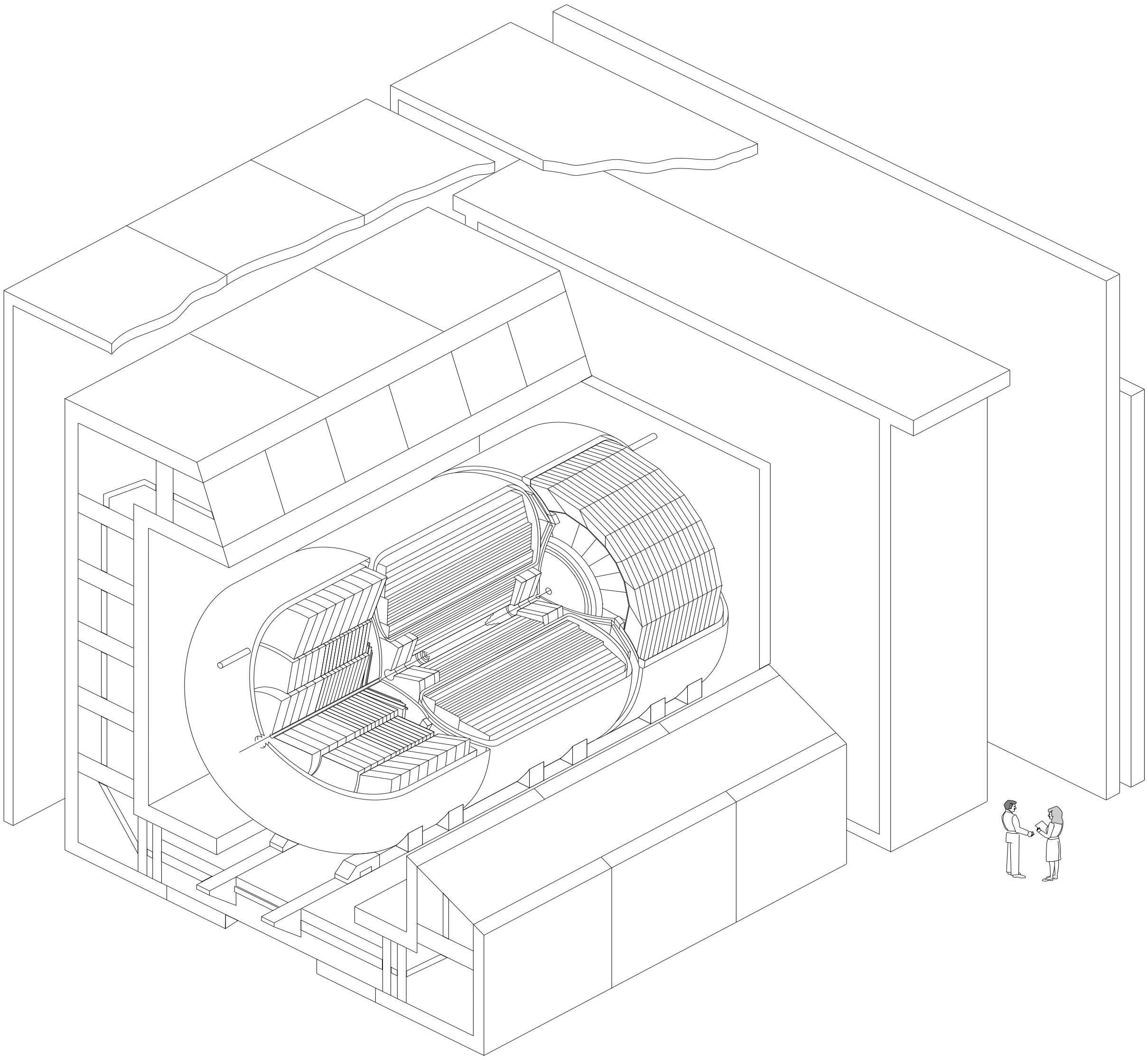

Figure 3.2: Cutaway view of the DØ detector

A-layer. Following the A-layer is the large central toroid (CF). Enclosing the A-layer and central toroid is the B-layer, and finally comes the outermost layer of chambers referred to as the C-layer. In the forward and backward directions are located the end cap toroids (EF), and concentric with the EF toroids are the two small angle (SAMUS) toroids. The muon system covers the pseudorapidity range $|\eta| < 3.4$.

The entire detector sits upon a support platform that can be rolled in and out of the DØ collision hall. Much of the front-end electronics for the detectors also rest upon the platform. Cables from the detector elements pass over an articulating bridge from which they are led into the moveable counting house (MCH). The cable bridge and MCH are located outside the concrete Tevatron shield wall. Digitized information produced in the MCH is collected, zero suppressed, and passed over high-speed data highways to one of many data acquisition processor nodes located in the control room area.

## 3.3 The DØ Tracking System

As mentioned previously, the DØ tracking system is composed of the following sub-detectors [39]:

- The Vertex Drift Chamber (VTX).
- The Transition Radiation Detector (TRD).
- The Central Drift Chamber (CDC).
- Two Forward Drift Chambers (FDC).

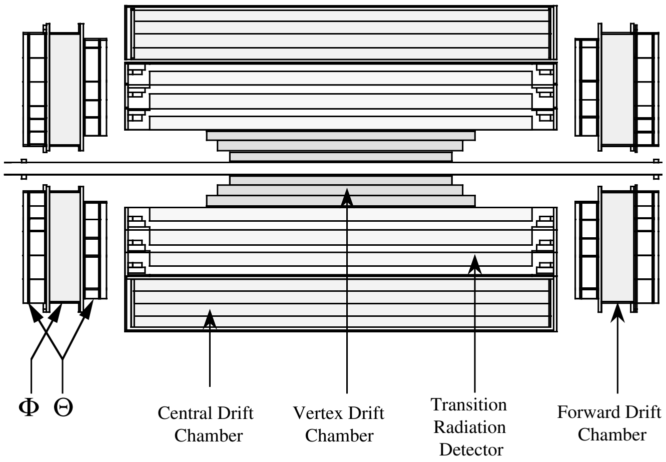

Figure 3.3: A cross section of the DØ central detectors

The VTX, TRD, and CDC cover the central pseudorapidity region and are arranged as concentric cylinders, each concentric with the beam pipe. The FDCs cover the small angle regions and are oriented perpendicular to the beam pipe. Fig.3.3 shows a cross sectional view of the DØ tracking system.

The tracking system fits within the inner cylindrical aperture of the calorimeters in a volume bounded by $r$ = 78cm and $z = \pm 135$ cm ( the z-axis runs along the beam pipe). Because there is no central magnetic field for measuring the momenta of charged particles, emphasis was placed upon the need for good two-track resolving power, high efficiency, and good ionization energy measurement so as to be able to distinguish single electrons from closely spaced conversion pairs. Inclusion of the TRD allows for an additional rejection factor of about 50 for isolated pions over and above that given by the calorimeter alone. The tracking system was designed to match the collider bunch-time interval of 3.5 $\mu$ s. This time allows relatively long drift cells. Good two-track resolving power is obtained by employing a flash analog-to-digital (FADC) conversion system for signal digitization in which the charge is sampled at about 10 ns intervals. The spatial resolution is on the order of 1 mm and is set by the need for primary z-vertex determination and by calorimeter shower matching.

### 3.3.1 Vertex Detector

The VTX chamber [40] is the innermost tracking detector in DØ . It has an inner radius of 3.7 cm (just outside the beryllium beam pipe) and an active outer radius of 16.2 cm. The VTX consists of three concentric layers of cells. The walls of these cells are made of a low density material (carbon fiber) to minimize the rate of photon conversions to $e^+e^-$ pairs. Eight sense wires in each cell are read out at both ends to measure z position using charge division. Adjacent sense wires are staggered by $\pm 100$ $\mu$m to resolve left-right ambiguities. The cells of the three layers are further offset in $\phi$ to aid in pattern recognition.

The gas chosen for operation of the VTX is $CO_2$ (95%) - ethane (5%) at one atmosphere with a small admixture of $H_2O$. The average drift velocity of ions under normal operating conditions is about 7.3 $\mu$m/ns. Gas gain at the sense wires is about $4 \times 10^4$. A spatial resolution of 60 $\mu$m for drift distances greater than 2 mm was measured for the VTX. The track pair resolution efficiency was measured to be better than 90% for separations greater than 0.63 mm. Table 3.1 shows further design parameters for the VTX.

### 3.3.2 Transition Radiation Detector (TRD)

Because much of the hadronic debris produced by jets may fake electrons, it is important to be able to distinguish the latter from hadronic background. Charged particles radiate photons (X-rays for highly relativistic charged particles, $\gamma > 10^3$) when crossing the boundary between two media with different dielectric constants.

| Drift Chamber | VTX | CDC |
|---|---|---|
| Maximum Length (cm) | 116.8 | 179.4 |
| Number of layers | 3 | 4 |
| Phi sectors/layer | 16,32,32 | 32 |
| Sense wires/sector | 8 | 7 |
| Total number of sense wires | 640 | 903 |
| Number of alternate readout channels | 832 | 256 |
| Sense wire stagger ($\mu$m) | 100 | 200 |
| Maximum drift distance (mm) | 13.7 | 70.8 |
| Gas mixture | $CO_2/C_2H_4$ | $Ar/CH_4/CO_2$ |
| Pressure of gas (atm) | 1 | 1 |
| Drift Velocity ($\mu$m/nsec) | 8 | 34 |
| Sense wire resolution ($\mu$m) | 60 | 200 |
| Charge division resolution (cm) | $\pm 1$[a] | - |
| Alternate readout resolution (mm) | - | 20 |
| Pair resolution (mm) | 7 | 10 |

Table 3.1: Characteristics of vertex and central drift chamber

[a] Design spec.

The energy of such photons is inversely proportional to the square root of the mass of the charged particle crossing the boundary. In this way transition radiation detectors can be used to help distinguish electrons from hadrons. The total energy deposited by, for example, 5 $GeV$ electrons exceeds that deposited by pions of the same energy because of the transition radiation X-rays produced and also because of the relativistic rise of the specific ionization. A figure of merit for such detectors is the $e/\pi$ rejection ratio. Test beam studies at CERN for the DØ TRD showed the device to have an $e/\pi$ rejection ratio of about 30 while retaining 90% of the electrons.

The TRD [41] occupies the space between the VTX and the CDC. It consists of three separate units, each containing a radiator and an X-ray detection chamber. 393 radiator foils in a volume filled with nitrogen gas produce an energy spectrum for the X-rays which is determined by the foil thickness and the gaps between the foils. A radial-drift proportional wire chamber (PWC) acts as the X-ray conversion medium and also collects the resulting charge which drifts radially outwards to sense cells. The magnitude and time of arrival of clusters of charge are used in distinguishing electrons from hadrons. Each TRD chamber has 256 anode readout channels. The thickness of the full TRD at $\theta = 90°$ is 8.1% of a radiation length and 3.6% of an interaction length.

### 3.3.3 The Central Drift Chamber (CDC)

The CDC [39][42] provides tracking coverage in the central region (approximately $|\eta| < 1.2$). It surrounds the TRD just prior to the central calorimeter. Cylindrical in shape, the CDC has a length of 184 cm and radii between 49.5 and 74.5 cm. The CDC consists of four concentric rings with 32 azimuthal cells per ring. Each cell contains 7 sense wires read out at one end. Additionally, a delay line is located just before the first sense wire and one just after the last sense wire. The delay lines are read out at both ends. Adjacent wires within each cell are staggered by $\pm 200$ $\mu$m to help remove left-right ambiguities within the cells. A further aid in pattern recognition is that alternate cells in radius are offset by one-half cell. Maximum drift ditances are on the order of 7 cm.

While the sense wires are used to determine the azimuthal ($\phi$) angle of a track, the delay lines pick up signals induced from the nearest anode wire. A measurement of the difference in arrival times at the two ends permits location of the track along the z-coordinate. The CDC uses a gas mixture of $Ar(92.5\%)CH_4(4\%)CO_2(3\%)$ with a small admixture of $H_2O(0.5\%)$. A drift field of 620 V/cm produces a drift velocity of about 34 $\mu$m/ns. Table 3.1 gives further parameters for the CDC.

Spatial resolutions measured at FermiLab's test beam facility showed 2 mm along the length of the detector (z) and 150 $\mu$m in the $r - \phi$ plane.

### 3.3.4 The Forward Drift Chambers (FDC)

The FDC [43] is two chambers, one of which is located at either end of the concentric barrels of the VTX, TRD, and CDC. They are positioned just before the entrance walls of the end cap calorimeters. Together both chambers extend the tracking coverage to within $\theta = 5$ degrees of the beam pipe. Each FDC consists of three separate modules. A $\Phi$ module, whose sense wires are radial and measure the $\phi$ coordinate, is sandwiched between a pair of $\Theta$ modules whose sense wires measure the $\theta$ coordinate. The $\Phi$ modules contain 36 sectors over the full azimuth. Each sector contains 16 anode wires oriented radially but spaced along the z direction. Each $\Theta$ module consists of four separate quadrants with each quadrant containing six rectangular cells at increasing radii. Each such cell in turn contains 8 anode wires in z, as well as one delay line which gives a local measurement of the orthogonal coordinate. All adjacent anode wires (in z) of both the $\Phi$ and $\Theta$ modules are staggered by $\pm 200$ $\mu$m to help resolve ambiguities. Additionally, the upstream and downstream $\Theta$ modules are rotated by 45 degrees in $\phi$ with respect to each other. Maximum drift distances are on the order of 5.3 cm. The FDC chambers use the same gas as the CDC, with similar values for drift field and gas gain. Tests at FermiLab's test beam facility showed the FDCs to have a spatial resolution of 200 $\mu$m in the coordinate perpendicular to the wire. Single delay line position resolution for the FDC was measured to be $\sigma_z \approx 4mm$.

## 3.4 The DØ Calorimeter System

Since the DØ detector does not have a central magnetic field, it is left to the calorimeter system to provide energy measurements for electrons, photons, and jets. The calorimeter also plays an important role in helping to identify electrons, photons, jets, and muons, as well as establishing the transverse energy balance in an event.

There are two basic types of calorimeters used in measuring the energy of a particle. One such type is called a total absorption calorimeter. Here the particle loses all of its energy within the absorbing material of the calorimeter. The other type of calorimeter is called a sampling calorimeter. In this version a particle loses only a portion of its energy, so that effectively a sampling is made of that portion of the energy lost by the particle while traversing the absorbing material of the calorimeter. A correction, called the sampling fraction, is then made to convert the fraction of the energy measured to the full energy lost by the particle. Sampling calorimeters are generally composed of a dense absorbing medium, and a less dense active medium which samples the ionization produced in electromagnetic or hadronic showers.The DØ calorimeters [44], shown in Fig.3.4, are sampling calorimeters. The absorbing materials are uranium, copper, and stainless steel. The active medium is liquid argon (LAr).

The calorimeter is built up out of a basic cell structure into a set of pseudo-projective readout towers with each tower further subdivided in depth. Typical transverse sizes of towers are $\Delta\eta = 0.1$ and $\Delta\phi = 0.1$. A typical calorimeter unit cell is shown in Fig.3.5.

From the figure it can be seen that the basic structure consists of two absorber

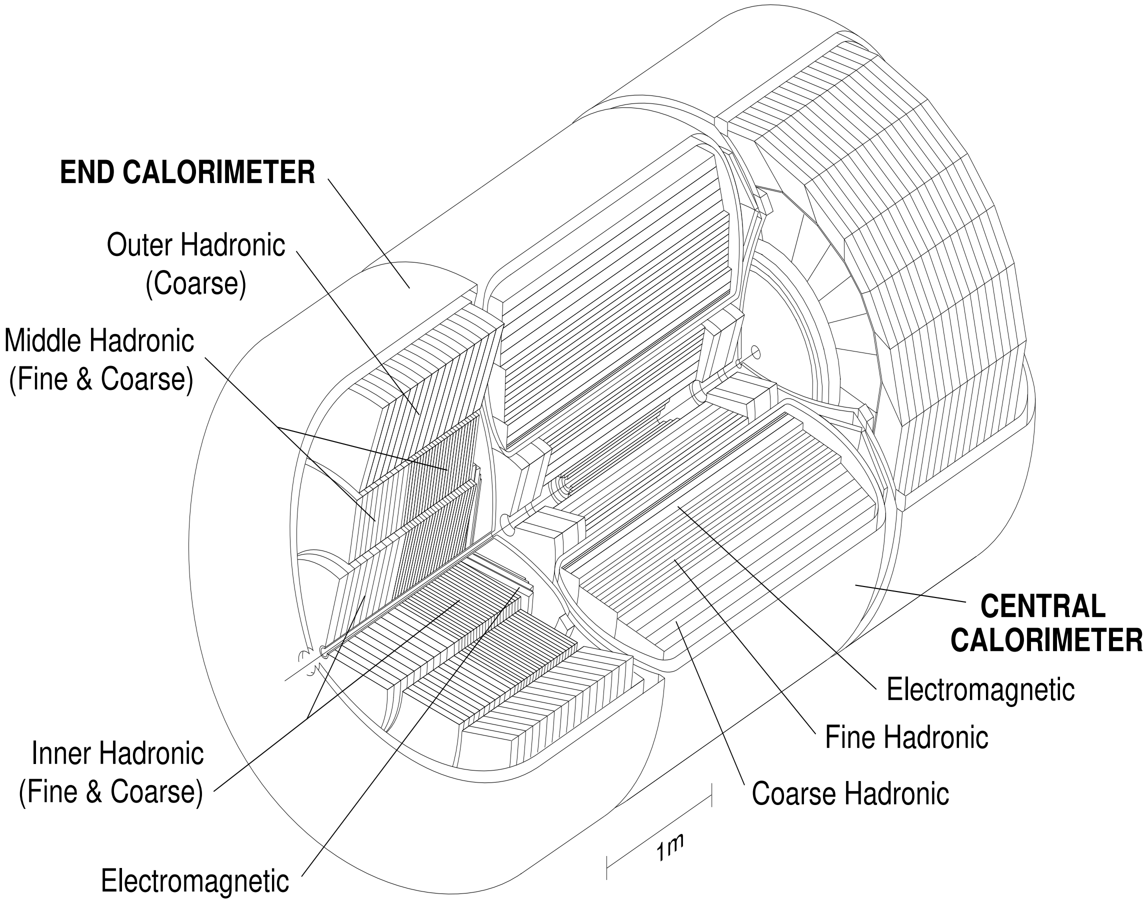


Figure 3.4: A cut away view of the DØ calorimeter system.

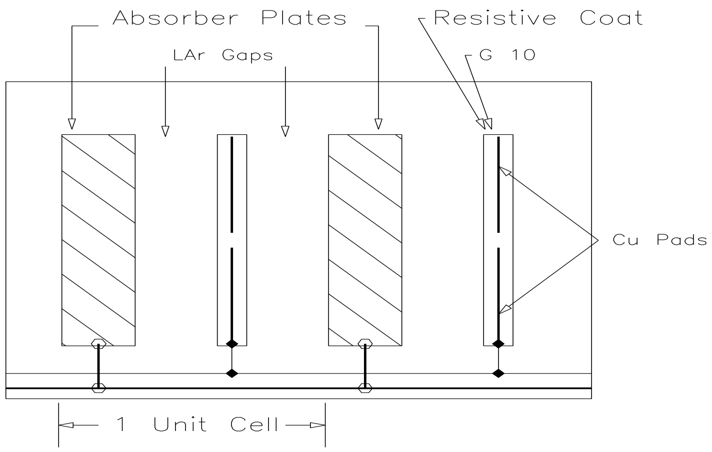


Figure 3.5: A unit cell structure of the DØ calorimeter.

plates that sandwich a G10 signal board situated between two LAr gaps. The signal board has copper pads inside and covered outside with a resistive coating. An eletric field of ≈8.7 kV/cm is applied between the absorber plates and resistive coat on the signal board. When a particle traverses the absorber plates a shower of secondary particles develops which ionizes the LAr. Ions liberated by the LAr drift across the gap between the absorber and signal board because of the applied electric field. The resulting current induces a charge on the inner copper pads of the G10 signal boards. This signal is preamplified and read out by the calorimeter electronics.

### 3.4.1 The Central Calorimeter (CC)

The CC covers the range $|\eta| < 1.2$. It consists of three concentric cylindrical shells. Innermost is the ring of 32 electromagnetic (CCEM) modules. Surrounding the

CCEM is the ring of 16 fine hadronic (CCFH) modules. Finally, the outermost shell is the ring of 16 course hadronic (CCCH) modules. End plates serve as support members for the modules in a given ring. The CC uses depleted uranium as the absorbing material.

The CCEM has four separate layers in depth. The first two layers are 2 radiation lengths ($X_0$) thick. These layers sample longitudinal shower development near the beginning of showers where photons and $\pi^0$s differ statistically. The third layer includes the region of maximum EM shower energy deposits and is 6.8 $X_0$ thick. The fourth layer is 9.8 $X_0$ thick and makes the total thickness for the CCEM approximately 20 $X_0$. The third layer of the CCEM is twice as finely segmented as usual in both $\eta$ and $\phi$ so as to allow more precise location of EM shower centroids. The total number of signals for the 32 modules of the CCEM is about 10,400. The modules span 24 $\Delta\eta = 0.1$ towers for a length of 260 cm. A full module comprises 20.5 $X_0$ and 0.76 $\lambda_A$ (nuclear absorption lengths) and weighs 0.6 metric tons.

The CCFH has three layers in depth with approximate thicknesses of 1.3, 1.0, and 0.9 $\lambda_A$ respectively. The CCCH is just one layer in depth with a thickness of 3.2 $\lambda_A$. The CCFH modules weigh 8.3 metric tons and provide about 3500 signals. Similarly, the CCCH modules weigh 7.2 metric tons and produce about 770 signals. The total weight of the CC modules and their support structures is about 305 metric tons, with an additional 26 metric tons due to the LAr.

The energy resolution of a sampling detector is typically expressed as follows:

$$(\frac{\sigma}{E})^2 = C^2 + \frac{S^2}{E} + \frac{N^2}{E^2} \tag{3.1}$$

Here E is the mean energy of the incident particle, C is a constant reflecting

| Central Calorimeter | EM | FH | CH |
|---|---|---|---|
| Number of modules | 32 | 16 | 16 |
| Absorber [a] | Uranium | Uranium | Copper |
| Absorber Thickness (cm) | 0.3 | 0.6 | 4.65 |
| Argon gap (cm) | 0.23 | 0.23 | 0.23 |
| Number of signal boards/module | 21 | 50 | 9 |
| Longitudinal depth | 20.5 $X_0$ | 3.2 $\Lambda$ | 3.2 $\Lambda$ |
| Number of readout layers | 4 | 3 | 1 |
| Number of signal boards/readout depth | 2,2,7,10 | 21,16,13 | 9 |
| Total $X_0$ [b] | 20.5 | 96.0 | 32.9 |
| Total $\Lambda$ [c] | 0.76 | 3.2 | 3.2 |
| Sampling fraction (%) | 11.79 | 6.79 | 1.45 |
| eadout segmentations ($\Delta\phi \times \Delta\eta$) [d] | $0.1 \times 0.1$ | $0.1 \times 0.1$ | $0.1 \times 0.1$ |
| Total number of readout cells | 10368 | 3000 | 1224 |
| Maximum pseudorapidity coverage | $\pm1.2$ | $\pm1.0$ | $\pm0.6$ |

Table 3.2: Central Calorimeter characteristics

[a] Uranium absorbers are depleted. FH absorbers are Uranium and 1.7% of Niobium alloy
[b] Total radiation length at $\eta = 0$
[c] Total interaction length at $\eta = 0$
[d] The third layer of the EM calorimeter is $0.05 \times 0.05$ in $\eta - \phi$ space.

calibration errors, S is a constant representing shower fluctuations in the LAr gaps, and N is a constant representing the contribution from noise - both electronic and that induced by the radioactivity of the uranium absorber. The measured values (from test beam electrons) [45][46] for the CCEM are $C = 0.003 \pm 0.004$, $S = (0.162 \pm 0.011)\sqrt{GeV}$, and $N = 0.140\ GeV$. Further characteristics for the CC are shown in Table 3.2 [47].

### 3.4.2 The End Calorimeters (EC)

The north and south ECs cover the pseudorapidity range $1.1 < |\eta| < 4.5$. The ECs are composed of four different module types. These are the electromagnetic modules (ECEM), the inner hadronic modules (ECIH), the middle hadronic modules (ECMH), and the outer hadronic modules (ECOH). There is just one ECEM module as well as only one ECIH module, however there are concentric rings of 16 middle and outer hadronic modules. The ECMH and ECOH modules are offset in azimuth to prevent the occurrence of cracks through which particles might pass.

The ECEM module has a total thickness of 24.1 cm and a diameter of 2 m. It is situated with its front face 1.7 m away from the nominal interaction point. The absorbing material is depleted uranium with an active medium of LAr. The pseudorapidity coverage is $1.4 < |\eta| < 4.0$. This provides hermetic coverage for the EM calorimeter down to the beam pipe.

The north and south ECIH modules are cylindrical. The inner radius is 3.92 cm while the outer radius is 86.4 cm. The absorbing material is uranium, except for the course hadronic section which is stainless steel. The pseudorapidity coverage is $1.6 < |\eta| < 4.5$.

Surrounding the ECIH is the ring of 16 modules that comprise the ECMH. The absorbing material is uranium-niobium (2%) alloy and stainless steel. The ECMH covers the range $1.1 < |\eta| < 2.0$. The energy resolution function for the ECMH has been measured from test beam results using both electrons and pions (25 to 150 GeV). The parameters found for electrons are: $C = 0.010 \pm 0.004$, $S = 0.233 \pm 0.010\sqrt{GeV}$, $N = 1.22\ GeV$. For pions the results are: $C = 0.047 \pm 0.005$, $S = 0.439 \pm 0.042\sqrt{GeV}$, and $N = 1.28\ GeV$.

The ECOH ring again consists of 16 modules concentric with the ECMH ring. The pseudorapidity coverage is $0.7 < |\eta| < 1.4$. The absorbing material is stainless steel. Further parameters that describe the EC calorimeter are shown in Table 3.3.

| End Calorimeter | EM | IFH | ICH | MFH | MCH | OH |
|---|---|---|---|---|---|---|
| Number of modules | 1 | 1 | 1 | 16 | 16 | 16 |
| Absorber [a] | U | U | SS [b] | U | SS | SS |
| Absorber Thickness (cm) | 0.4 | 0.6 | 0.6 | 0.6 | 4.65 | 4.65 |
| Liquid Argon gap (cm) | 0.23 | 0.21 | 0.21 | 0.22 | 0.22 | 0.22 |
| $N_{signal-boards}$/module | 18 | 64 | 12 | 60 | 14 | 24 |
| Longitudinal depth | $20.5X_0$ | $4.4\Lambda$ | $4.1\Lambda$ | $3.6\Lambda$ | $4.4\Lambda$ | $4.4\Lambda$ |
| Number of readout layers | 4 | 4 | 1 | 4 | 1 | 3 |
| $N_{signal-boards}$/readout depth | 2,2,6,8 | 16 | 14 | 15 | 12 | 8 |
| Total $X_0$ | 20.5 | 121.84 | 32.78 | 115.5 | 37.95 | 65.07 |
| Total $\Lambda$ | 0.949 | 4.91 | 3.57 | 4.05 | 4.08 | 7.01 |
| Sampling fraction (%) | 11.9 | 5.66 | 1.53 | 6.68 | 1.64 | 1.64 |
| Cell size in $\eta$ [c] | 0.1 [d] | 0.1 | 0.1 | 0.1 | 0.1 | 0.1 |
| Cell size in $\phi$ | 0.1 | 0.1 | 0.1 | 0.1 | 0.1 | 0.1 |
| Minimum rapidity covered | $\pm1.4$ | $\pm1.6$ | $\pm2.0$ | $\pm1.0$ | $\pm1.3$ | $\pm0.7$ |
| Maximum rapidity covered | $\pm4.0$ | $\pm4.45$ | $\pm4.45$ | $\pm1.7$ | $\pm1.9$ | $\pm1.4$ |
| Total number of channels | 7488 | 5900 [e] | | 1664 [f] | | 960 |

Table 3.3: End Calorimeter characteristics

[a] Uranium(U) absorbers are depleted. IFH and MFH absorbers are Uranium and 1.7% Niobium alloy

[b] SS is stainless steel

[c] $\Delta\phi \times \Delta\eta = 0.2 \times 0.2$ in the region of $\eta \geq 3.2$

[d] The third layer of EM calorimeter is segmented $0.05 \times 0.05$ in $\eta - \phi$ space

[e] The sum of the number of the IH readout channels

[f] The sum of the number of the MH readout channels

### 3.4.3 Massless Gaps and The ICD

Because of cryostat walls, stiffening rings, module endplates, and other support elements, the region $0.8 < |\eta| < 1.4$ contains a considerable amount of uninstrumented material. In order to correct for the energy loss in this region two different types of detector have been installed to supplement the DØ calorimeter system. One system is called the Intercryostat Detector (ICD). There are two ICDs, one mounted on the front surfaces of each of the ECs. Each ICD consists of an array of 384 scintillator tiles of size $\Delta\eta = \Delta\phi = 0.1$. These tiles are the same size as the calorimeter cells and form a pseudo-projective structure with the calorimeter cells. The ICD uses phototube readout.

The other supplementary system is a collection of modules referred to as the Massless Gap (MG). These are mounted on the surfaces of the CCFH, ECMH, and ECOH modules. The MG modules are single cell structures consisting of two signal boards surrounded by three LAr gaps. The size of these cells match those of the ICD and calorimeter.

Some mention should be made of the Cryogenic system for the DØ calorimeter. This consists of three separate double-walled stainless steel cryostsats that enclose and help support the calorimeter. An inventory of 20,000 gallons of LAr is maintained in the cryostats and storage dewars. Cooling to LAr temperatures (78K) occurs in approximately 10 days.

## 3.5 The DØ Muon System

The basic hardware components of the muon detection system [48] are the five solid iron toroidal magnets, and a set of chambers consisting of proportional drift tubes (PDTs) [49]. The purpose of this system is to identify muons produced in $p - \overline{p}$ collisions, and to determine their trajectories and momenta. A particularly strong feature of the DØ detector is the fact that most of the debris from electromagnetic and hadronic showers is absorbed in the calorimeters. Thus muons can be identified fairly easily in the middle of hadronic jets. This is in contrast to the case for electrons.

The purpose of the toroids is to produce a bend in the muon trajectory. A measurement of the bend angle provides sufficient information for the determination of the muon's momentum. It is necesarry to measure muon direction both before and after the bend. A set of measurements of the track is made before the toroid, and two series of measurements after the toroid. The incident trajectory is determined from a combination of the primary interaction vertex, the track as seen in the central tracking system, and the series of measurements made before the toroid. Comparison of incident and exiting track vectors yields the bend angle in the toroid, and hence the muon's momentum. Because of multiple Coulomb scattering in the iron toroids, the relative muon momentum resolution is $\geq 18\%$ up to the limit imposed by the bend coordinate resolution in the PDTs. Fig.3.6 shows an elevation view of the DØ detector with the five toroids and their associated PDT layers of muon chambers.

### 3.5.1 The Muon Toroids

The central toroid (CF) covers the central pseudorapidity region $|\eta| < 1$. Two end toroids (EF) cover the region $1 < |\eta| < 2.5$. Two small angle toroids (SAMUS) fit within central holes of the EF toroids and extend the muon coverage over the region $2.5 < |\eta| < 3.3$ Fig.3.7 shows the variation in muon system thickness expressed in interaction lengths ($\lambda$) as a function of psuedorapidity ($\eta$).

From the figure it can be seen that the combined calorimeter and muon system is quite thick, ranging from a minimum of 8 $\lambda$ near the CF-EF boundary to a maximum of nearly 20 $\lambda$ in the EF region. The minimum momentum required for a muon to escape the iron toroids ranges from 3.5 GeV/c at $\eta = 0$ to about 5 GeV/c at larger $\eta$.

The CF toroid is centered on the Tevatron beam line. It is a square annulus 109 cm thick and weighing 1973 metric tons. The distance from the beam to the inner surface of the CF is 317.5 cm, while the distance to the outside surface is 427 cm. The CF is built out of three different pieces. The bottom piece is fixed to the detector platform and helps provide support for the enclosed tracking and calorimeter systems. The remainder of the CF is composed of two C-shaped shells which may be split apart to allow access to the interior detectors. Internal fields of about 1.9 Tesla are excited by twenty coils of 10 turns each carrying 2500 A currents.

The two EF toroids are located at $447 < |z| < 600$ cm. A 183 $cm^2$ hole, centered on the beam line , is located in the middle of each EF. Further, each EF has a 25 cm diameter hole through which the main ring beam line passes. Fields of approximately 2 Tesla are excited in the EFs by means of eight coils with 8 turns each carrying 2500 A currents. Each EF toroid weighs 800 metric tons.

The square inner hole of each EF toroid holds a small angle (SAMUS) toroid. Each samus toroid weighs 32 metric tons and has outer surfaces 170 cm from the beam axis. As with the EF, each samus toroid has an inner hole (102 $cm^2$) through which the beam pipe can pass. Two coils of 25 turns each carry currents of 1000 A. Tungsten-Lead collimators fill the space between the samus toroids and the Tevatron beam pipe. They serve to intercept beam halo at small angles.

### 3.5.2 Wide Angle Muon Chambers

The wide angle muon system (WAMUS) consists of the CF/EF toroids and a collection of WAMUS chambers. The WAMUS chambers are arranged in three layers: The A-layer chambers being inside the toroids, and the B and C-layer chambers situated outside the toroids. In order to get a good measure of the muon track after it exits the toroids, the B and C-layers are separated by $\geq$ 1m.

Each A-layer chamber is comprised of four planes of PDT cells, whereas B and C-layer chambers are composed of three such planes. The cell structure for all WAMUS PDTs is the same. There are 164 WAMUS chambers differing only in number of PDT planes , overall width, and length. The WAMUS chambers cover the approximate pseudorapidity range $|\eta| < 2.4$. WAMUS PDTs are formed from aluminum extrusion unit cells which are cut to the appropriate lengths and then press-fit together. There is a transverse offset between planes of PDT cells to help in resolving left-right drift-time ambiguities. Fig.3.8 shows the basic interior construction of the WAMUS PDTs. Two cathode pad strips are inserted into the top and bottom of each cell. Gold-plated tungsten anode wires are held at 300 g tension near the center of each cell. The maximum drift distance is 5 cm. The aluminum extrusions are held at ground potential, while the cathode pads are held at +2.3 kV, and the anode wires are held at +4.56 kV.

In order to obtain position measurements along the muon track, both the drift or bend coordinate (perpendicular to the anode wire) and the wire or non-bend coordinate (along the anode wire) must be determined. To measure the bend coordinate one must know the relation between drift time and drift distance for the ions produced by the charged muon traversing the cell. The chambers are operated using a trinary gas mixture of $Ar(90\%)CF_4(5\%)CO_2(5\%)$. The drift velocity is approximately 6.5 cm/$\mu$s, but varies across the cell with changing $\vec{E}$. Tests with this gas indicate an approximately linear time-distance relation. Knowing both the drift velocity and drift time allows one to calculate the drift distance and the bend coordinate. Bend coordinates are measured with a resolution on the order of 500 $\mu$m.

The non-bend coordinate ($\zeta$) along the wire is measured [50] by a combination of cathode pad signals induced by the anode pulse, and timing information derived from the anode wires. The anode wires for adjacent cells are jumpered together at one end while the signals for the wire pair are read out at their other ends. To facilitate the determination of $\zeta$, the cathode pads, which consist of copper-clad Glasteel, have their copper cladding routed into a repeating diamond-shaped pattern with a repeat distance of 61 cm. By measuring the time difference ($\Delta t$) for a particular anode signal to arrive at the ends of the paired anode wires one can make a course determination of $\zeta$ with a precision varying between 10 and 20 cm. This is sufficient to establish in which diamond shape the hit occurred. Fine resolution in $\zeta$ is obtained by using the information from the cathode pad signals. The routing of the upper and lower cathode pads in each cell results in the cathodes being divided into two independent electrodes which form the inner and outer portions of the repeating diamond pattern discussed earlier. The two inner pads are summed and read out independently of the sum of the two outer pads. Fig.3.9 shows the cathode pad structure. The ratio of the sum and difference of inner and outer pad signals can be used to measure $\zeta$ with a resolution of approximately $\pm 3$ mm.

Signal shaping, time-to-voltage conversions, latching of struck cells, chamber monitoring and multiplexing of signals for efficient transport to the digitizers are performed locally. Each WAMUS chamber has a set of electronics boards housed in enclosures attached to the chamber body. ADCs and Trigger electronics reside in the Moveable Counting House (MCH).

### 3.5.3 Small Angle Muon Chambers

The small angle muon system (SAMUS) consists of two SAMUS toroids and a collection of SAMUS chambers. The SAMUS chambers cover the pseudorapidity region $2.5 < |\eta| < 3.5$. As with WAMUS, the SAMUS chambers are also arranged into three layers called stations. A-station precedes the SAMUS toroids, with B and C-stations placed after the SAMUS toroids. The SAMUS stations cover an area of 312×312 $cm^2$ perpendicular to the beam direction. Interior square holes permit the passage of the beam pipe. Each station consists of three planes of cylindrical proportional drift tubes. Each plane in turn is segmented into two half-planes or doublets. The tubes in a given plane are oriented along the x,y, and u directions (u being at 45 degrees with respect to x and y). Adjacent tubes are offset by one half a tube diameter. The SAMUS system contains a total of 5308 tubes. Anode wires are gold-plated tungsten and are tensioned to 208 g. The gas mixture is $CF_4(90\%)CH_4(10\%)$ with an average drift velocity of 9.7 cm/$\mu$s. The maximum drift time is 150 ns. As with WAMUS, the drift time to drift distance is nearly linear. The resolution of a single drift tube is approximately 350 $\mu$m. The signal processing and digitization is similar to that employed for WAMUS. Further details of the muon system are listed in Table 3.4.

| | |
|---|---|
| Magnetic field strength | 2 T |
| Magnetic kick (90°) | 0.61 GeV/c |
| System precision goal in bend plane | 500 $\mu$m (Diffusion limit, 200 $\mu$m) |
| System precision goal in non-bend plane | 2-3 mm (charge ratio, $\pm$1.0%) |
| $\delta p/p$ (multiple scattering limit)[a] | 18% |
| $3\sigma$ sign determination ($\theta, \phi$ 90°,0°) | $P_t \leq$350 GeV/c |
| Interaction lengths (90°) | 13.4 |
| Interaction lengths (5°) | 18.7 |
| Drift-coordinate resolution | $\pm$0.45 mm |

Table 3.4: Design parameters of the DØ muon system

[a] Absolute theoretical limit assuming 100% chamber efficiency.

## 3.6 Trigger and Data Acquisition

The DØ detector utilizes three different levels of triggers [51]. The Level 0 trigger is a hardware trigger based upon the use of scintillators to indicate the presence of an inelastic collision. The rate of Level 0 triggers is about 150 kHz at a luminosity of $5 \times 10^{30} cm^{-2} s^{-1}$. The Level 1 trigger is a collection of hardware trigger elements driven by a flexible software architecture. Most Level 1 triggers operate within the 3.5 $\mu$s time window between beam crossings and therefore suffer no dead time. Some triggers, however, require several beam crossings to complete. These are referred to as Level 1.5 triggers. The rate of Level 1 triggers is approximately 200 Hz ( about 100 Hz for Level 1.5). Events that satisfy the Level 1 (and Level 1.5) triggers are passed on to a farm of microprocessors which serve as event builders as well as the Level 2 software trigger system. The Level 2 triggers utilize sophisticated software algorithms to reduce the event rate down to about 2 Hz before passing them on to the Host computers for event monitoring and recording.

A block diagram of the trigger and data acquisition system is shown in Fig.3.10.

### 3.6.1 The Level 0 Trigger

The Level 0 trigger indicates the occurrence of an inelastic collision. It also serves as the luminosity monitor for the experiment. The hardware elements of this trigger consist of two scintillator hodoscopes, each being mounted on the front surfaces of the opposing EC cryostats and perpendicular to the beam direction. Each hodoscope has 20 short (7 cm $\times$ 7 cm) scintillation elements with single photomultiplier readout, and 8 long (7 cm $\times$ 65 cm) elements each readout by two photomultipliers. The time of flight resolution of the hodoscopes is typically 100-150 ps. Vertex z-coordinates are determined from the difference in arrival time for particles hitting the two Level 0 detectors. All Level 0 calculations are performed in hardware and are available for use in the Level 1 and Level 2 trigger decisions.

### 3.6.2 Level 1 Triggers

Among the various Level 1 trigger devices are the hardware Level 1 calorimeter trigger and the Level 1 muon trigger. A so-called Level 1 Framework gathers digital information from each of the specific Level 1 trigger devices and determines whether a particular event should be kept for further examination. The Level 1 framework coordinates various vetos which can inhibit triggers, provides prescales for triggers that have too high pass rates, correlates trigger and readout functions, and manages communication tasks with front-end electronics and the Trigger Control Computer (TCC).

The Framework employs a two-dimensional AND-OR network which is used to select triggers. The set of inputs to the network are 256 latched bits called AND-OR terms. Each of these bits represents some specific piece of detector information (for example, 2 calorimeter clusters over 5 GeV, 1 muon candidate with $|\eta| < 1$, and so on). Various logical combinations of these AND-OR terms results in the outputting of 32 specific Level 1 triggers. Satisfaction of any of these triggers results in a readout request by the data acquisition hardware. The Level 1 Framework then assembles a block of information that summarizes all the conditions that have lead to a positive Level 1 decision. This is then passed on to Level 2 for further analysis.

A simplified view of the Level 1 trigger system is shown in Fig.3.11. The basic input to the Level 1 muon trigger is a single latch bit for each of the approximately 16,700 PDT cells of the WAMUS and SAMUS muon system. The output consists of 16 Level 1 and 16 Level 1.5 physics bits. These are sent to the AND-OR network of the Level 1 Trigger Framework for full trigger information. These bits represent the number of course muon candidates found within specific pseudorapidity regions of the muon system. The input bits for the Muon Level 1 trigger system are received in the MCH by 200 Module Address Cards (MACs) contained in 24 VME digitizing crates. Each crate has a 68020 microprocessor used for downloading data and event building. The MAC cards and subsequent Level 1 and Level 1.5 trigger electronics are kept physically distinct for each of the 5 separate $\eta$ regions of the muon detector (CF, EF-North, EF-South, SAMUS-North, and SAMUS-South).

Each trigger region is divided azimuthally into quadrants, except for the CF which is divided into octants. In a given octant in the CF, for example, the chambers are further grouped in $\eta$ so that one has: 5 C-layer chambers, 5 B-layer chambers, 3 A-layer chambers. A typical 24 PDT cell wide chamber reports 48 half-cell wide locations (fine centroids). The fine centroid resolution is 5 cm. For each chamber in the octant its MAC ORs the 48 fine centroids by 3 to produce 16 course centroids with $3 \times 5 = 15\ cm$ resolution. A given octant then reports A(3,16), B(5,16), C(5,16) course centroids. These are sent to a Course Centroid Card (CCT) which ORs one more time for each layer by 4 to produce $(5\times16)/4 = 20$ course centroids in B and C layers, and $(3\times16)/4 = 12$ course centroids in A layer. The output of the octant is then given as A(12), B(20), C(20) with a course centroid resolution of $4\times15 = 60$ cm.

B and C combinations are programmed in PALs for a given A(i) i=1,2,...,12 as BC(i) = B(j)$\wedge$C(k) (summed for selected j and k). Finally the CCT matches the A(i) with its associated BC(i) to form bit pattern combinations of the form A(i)$\wedge$BC(i). These represent possible track candidates. The allowed B(j)$\wedge$C(k) combinations that contribute to a given non-zero A(i) determine the effective $p_T$ cut-off on the muon Level 1 trigger for the region under consideration. More allowed B(j)$\wedge$C(k) combinations imply a broader range of muon momenta to trigger on, since more bend is permitted in each muon track.

As stated earlier centroids are defined as the most likely half-cell (5 cm in WAMUS and 1.5 cm in SAMUS) traversed by a track, projected to the midplane of a chamber. The bit pattern produced by the MACs represents a logical OR of the centroids. In WAMUS this OR is made on a group of 3 centroids, whereas SAMUS uses groups of 4. The output of all CCTs for a given $\eta$ region is sent to a second CCT-like card which counts muon candidates in that region. Two bits of muon multiplicity information per region are then sent to a Trigger Monitor Card (TRGMON) which finally outputs the physics bits referred to earlier to the

AND-OR network of the Level 1 Trigger Framework. After a trigger framework decision on any Level 1 muon trigger, the MACs have their full centroid lists strobed into Octant Manager Cards (OTC) for use by Level 1.5 triggers. By employing look-up tables which correspond to possible tracks with $p_T$ thresholds above a certain value (typically 3 to 7 GeV/c), the OTCs are able to output two 24-bit trigger words and a status word. These are read by an OTC manager (OTCMGR) card which uses centroid information contained in the trigger words to output three bits to the TRGMON corresponding to transverse momentum, multiplicity, and geographic information. Upon receipt of good Level 1 or Level 1.5 triggers from the framework, all trigger words in the OTCMGR are read out by VME Buffer/Drivers (VBDs) in each OTC crate.

### 3.6.3 The Level 2 Trigger

The Level 2 trigger system consists basically of a farm of 50 micro-VAX 4000-M60s. This Level 2 system collects the digitized data from all relevant detector elements for events that have successfully passed the Level 1 (or Level 1.5) triggers. Processing of the event is built around a collection of algorithms referred to as filter tools. These filter tools serve to identify a particular kind of particle or event characteristic. Specific tools exist for muons, electrons, photons, jets, $\tau$'s, scalar $E_T$, and missing $E_T$. These various tools are combined together to form so-called filter scripts. A specific script is associated with each of the 32 Level 1 specific triggers. These scripts may then spawn several Level 2 filters from a given Level 1 trigger bit. There are 128 Level 2 filter bits available for use in studying specific physics interests. If an event passes a filter, the data is transferred to the host computer for subsequent logging of the event. The maximum input rate to the

Level 2 system is 200 Hz. The output from Level 2 is limited to approximately 2 Hz.

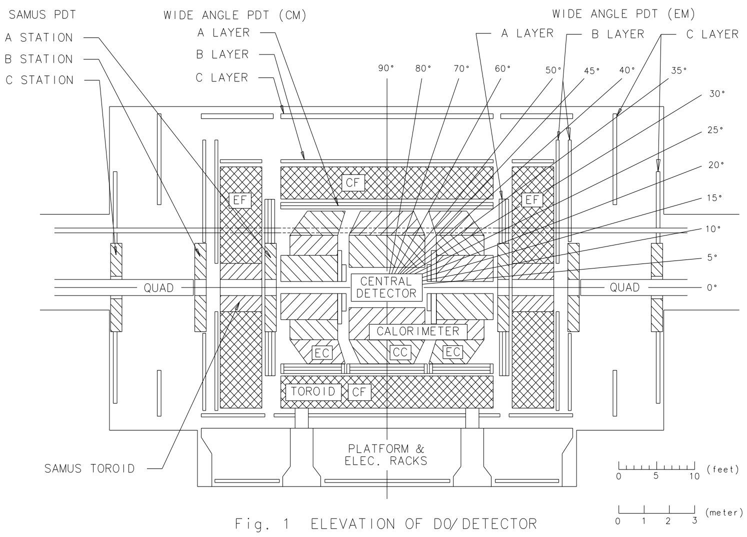


Figure 3.6: Elevation view of the DØ detector.

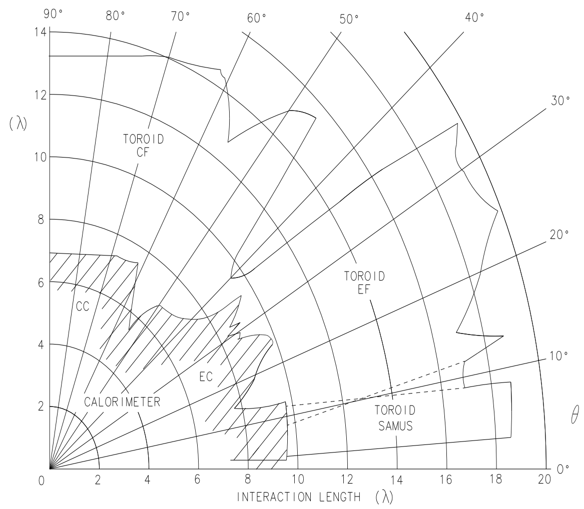


Figure 3.7: Total interaction lengths of calorimeter and muon system.

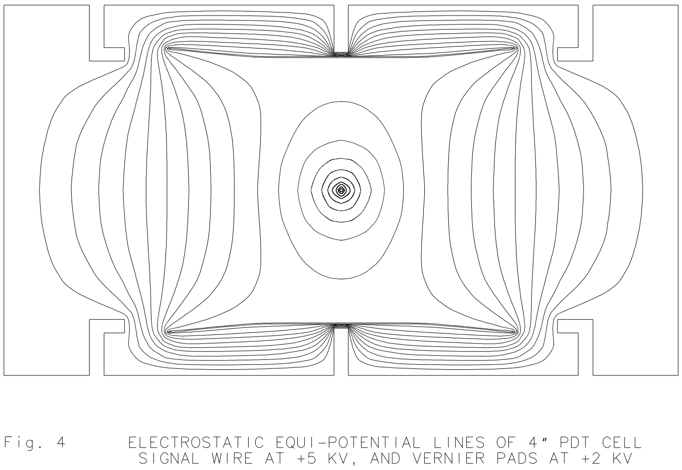


Figure 3.8: Muon System PDT Cell structure.

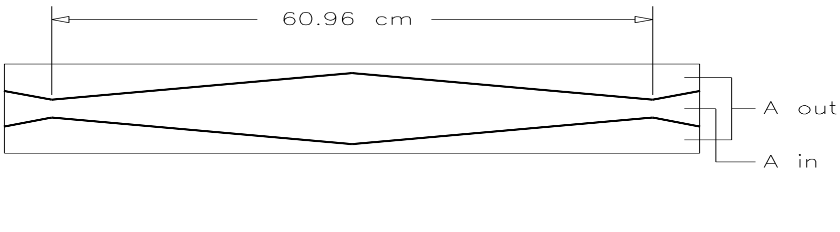


Figure 3.9: WAMUS PDT cathode pad structure.

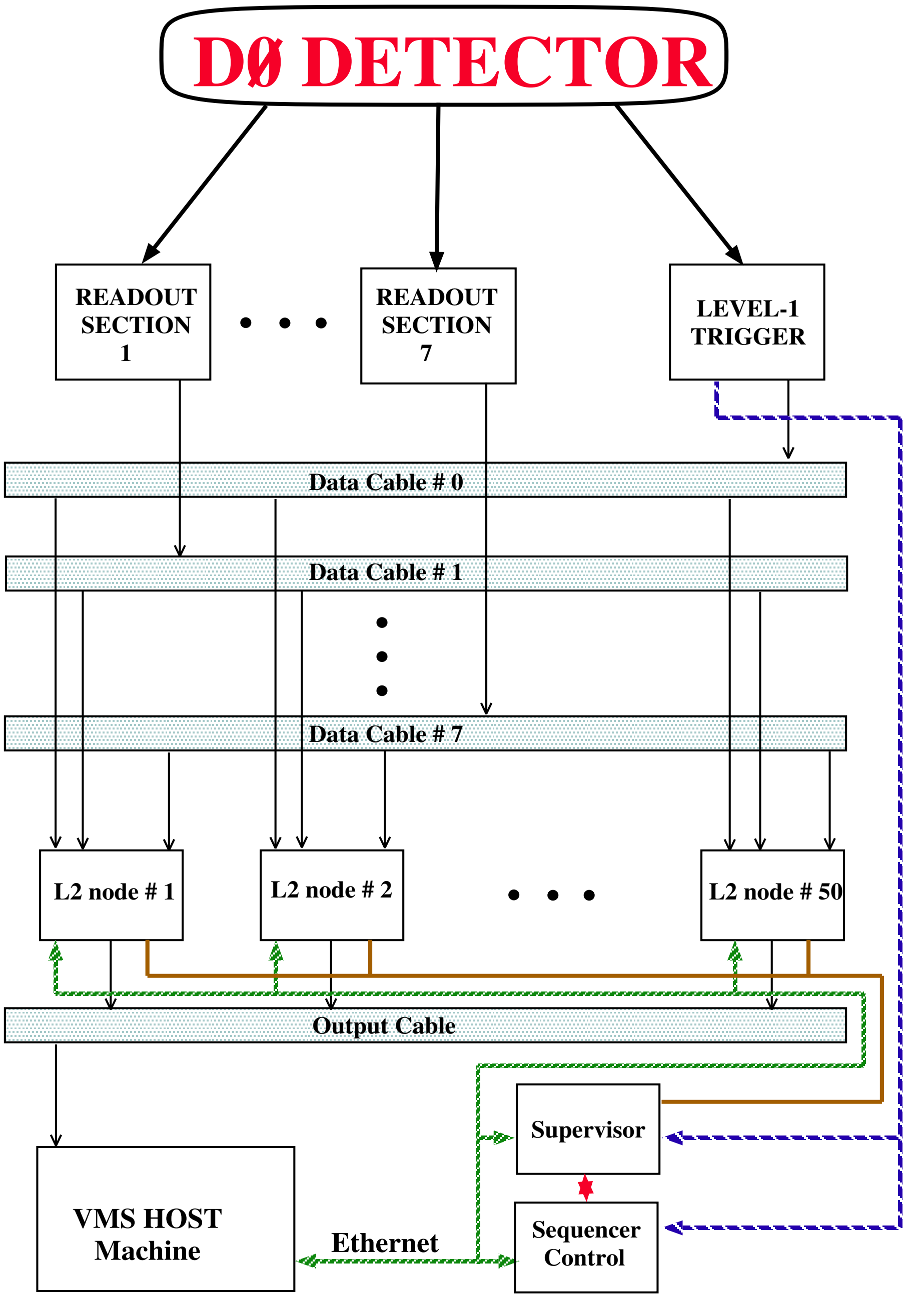


Figure 3.10: DØ trigger and Data Acqusition System.

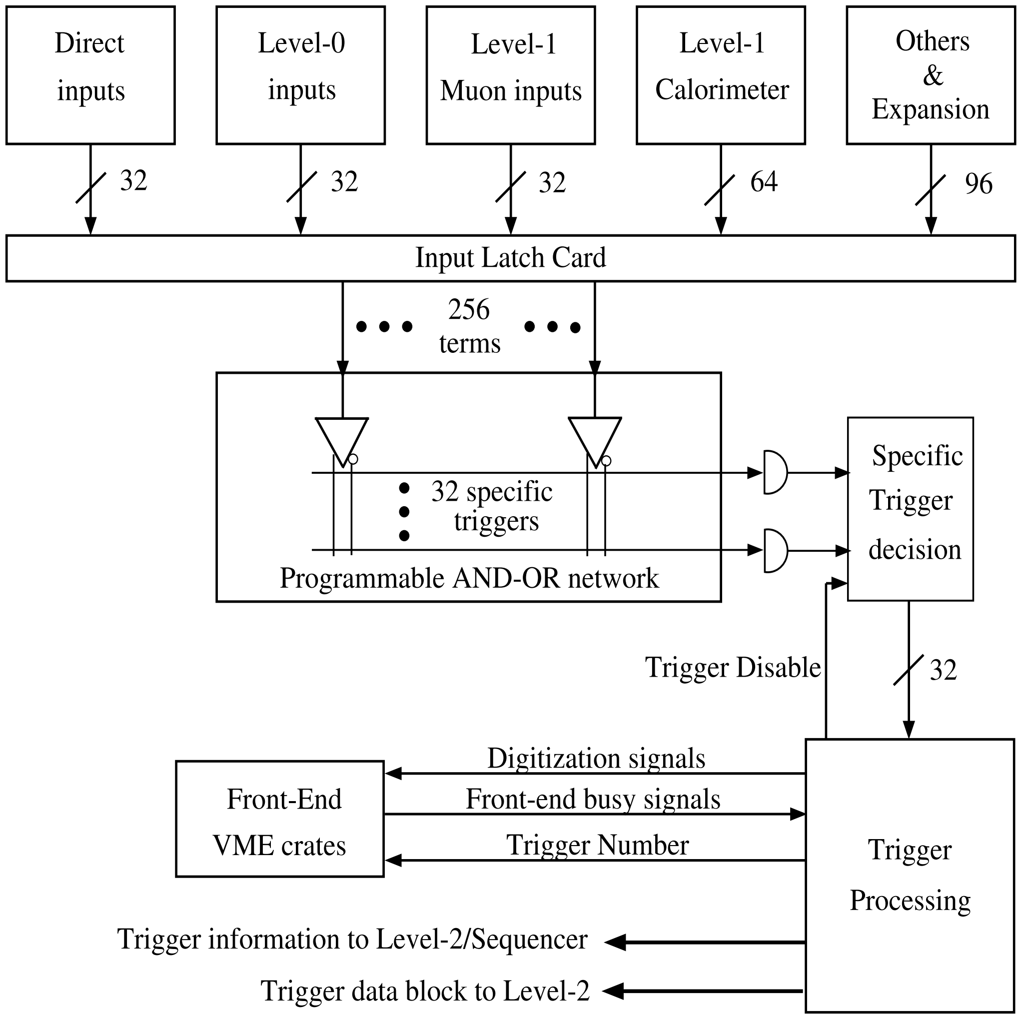


Figure 3.11: Level 1 Trigger processing stages

# Chapter 4

# Event Reconstruction and Simulation

The selection of a data sample for further analysis entails a host of prior complications. The very first steps involved in selecting and filtering the data require that specific trigger conditions be satisfied. These trigger requirements are designed to enhance physics signals of particular interest and to supress as much as possible the background to these signals. As mentioned previously, this initial trigger selection takes place in stages–proceeding through the hardware based Level 0 and Level 1 trigger, and thence to the tighter requirements imposed in the Level 2 software trigger and its associated filters. The idea here is to reduce the very high event rate to acceptably low levels, while still insuring that minimal loss occurs for signal events.

The initial trigger selection process yields raw data in the form of digitized signals specific to the various detector components. This raw data is then written to tape. The next step in the refinement of the data is the offline reconstruction process which is charged with the herculean task of re-interpreting these digitized signals in terms of generically recognizeable physics objects, namely charged particle tracks and various local clusters of energy distributions representing showers

| Trigger Component | Physics Object | Selection Criteria |
|---|---|---|
| Level 1 | $\geq$ 2 muons | $\lvert\eta_\mu\rvert \leq 1.7$ |
| Level 2 | $\geq$ 2 muons | $\lvert\eta_\mu\rvert \leq 1.7$ |
| | | $p_T^\mu \geq 3\ GeV/c$ |

Table 4.1: The MU-2-HIGH Trigger

in the calorimeter. Detailed reconstruction algorithms then proceed to make tentative identification of more specific physics objects, such as muons, jets, and electron candidates.

Generally, the final step in the data selection process revolves around offline analyses which further seek to validate particle identification and to select event topologies that are characteristic of the specific signals sought.

In the remaining sections we discuss each of these aspects in turn, particularly as they bear upon the problem of obtaining the final dimuon data sample which contains the $J/\psi$ signal.

## 4.1 The Trigger Selection

The trigger used in this analysis is a dimuon trigger called "MU-2-HIGH". As with most of the DØ triggers, it is comprised of a hardware-based Level 1 component, and a software-based Level 2 component. The essentials of this particular trigger are summarized in Table 4.1.

### 4.1.1 Level 1

The dimuon trigger used in this analysis was trigger bit 6 in the DØ global list of triggers. As mentioned previously, it is called MU-2-HIGH and denoted by the shorthand mu(2,y2). The y2 denotes the muon eta coverage involved ( y2 implies $|\eta_\mu| \le 1.7$), whereas the 2 obviously indicates the requirement for 2 muons. The rate of events passing mu-2-high at Level 1 was $\sim$ 3.2 $Hz$ at a luminosity of $1.0 \times 10^{30}\ cm^{-2}s^{-1}$. At luminosities above $6.0 \times 10^{30}\ cm^{-2}s^{-1}$ the pre-scale factor was set to two (this happened only infrequently during Run 1A). The muon eta coverage of this particular trigger was sufficient to encompass the CF and EF regions (all of WAMUS) of the muon system.

Several further requirements at Level 1 were implemented in the form of veto conditions. One such veto was a disenabling of the trigger for a period of $\sim \pm 0.2\ \mu s$ centered on the time of $p\bar{p}$ beam crossing. At this time proton bunches from the operation of the Main Ring are passing the DØ collision point. In fact most of the time the Main Ring was in simultaneous operation along with the Tevatron Collider itself. Since the Main Ring passes through the top of the DØ detector, activity in the Main Ring tended to cause some severe complications for the muon system (chamber inefficiencies in the neighborhood of the Main Ring, that is at $\phi \sim 100°$). This particular veto (mrbs-loss) incurred a dead time of $\sim$ 8%. A second veto of duration $\sim 0.6\ \mu s$ was implemented during the time of Main Ring injection when the proton losses were largest. This second veto (micro-blank) resulted in a dead time of $\sim$ 17%.

A somewhat better appreciation of this dimuon trigger can be gained by considering the single-muon Level 1 trigger. The trigger turns on at essentially $p_T^\mu = 3\ GeV/c$. This turn-on point is determined by the thickness of the muon system and the the PAL trigger logic design (Chapter 3). The 50% point is reached in the neighborhood of $p_T^\mu = 4 - 5\ GeV/c$, while the plateau value of $\sim$ 55% is attained at $p_T^\mu = 7.5 - 8.0\ GeV/c$ [52]. The decay muons for the $J/\psi$ have relatively small opening angles between them. This implies that the $p_T$ of the dimuon system is very nearly the sum of the $p_T$'s of the individual muons. The implication for the dimuon Level 1 trigger efficiency is a turn-on near $p_T^{\mu\mu} = 6\ GeV/c$ with a rise to a plateau value of approximately $0.55^2$ at $p_T^{\mu\mu} = 15 - 16\ GeV/c$. In Chapter 5 we will discuss the trigger efficiency for the $J/\psi$ in more detail.

### 4.1.2 Level 2

The Level 2 mu-2-high trigger is software-based and is constructed from a set of detailed algorithms that consitute a filter script (as discussed in Chapter 3) for the trigger. The essential part of this filter script is called "muon-l2". The muon-l2 filter consists of three shell fortran routines called MUON-L2-INIT, MUON-L2-PARAMETERS, and MUON-L2. MUON-L2-INIT has software which basically communicates the muon system geometry file and muon level 2 run control parameters (RCP file) to the muon level 2 filter. MUON-L2-PARAMETERS reads the file produced by MUON-L2-INIT (called a muon STP file) for parameters specifying such things as the following:

- the minimum number of muon track candidates required by the trigger
- the minimum $p_T^{\mu}$ required for a muon candidate
- the maximum allowed eta value that a muon may have in order to pass the trigger
- the quality of a muon candidate-that is, loose, tight, etc.

MUON-L2 is the fortran routine that is run for each event and which decides whether to pass the event based upon a comparison of data and the parameters read by MUON-L2-PARAMETERS. In the course of making its trigger decision MUON-L2 runs a program similar to that run for offline muon reconstruction (but somewhat simplified).

The rate of events passing mu-2-high at Level 2 was $\sim$ 0.02 $Hz$ at a luminosity of $1.0 \times 10^{30}$ $cm^{-2}s^{-1}$.The measured cross section for events passing mu-2-high was approximately 2.3 $\mu b$ out of a total min-bias cross section of about 42 $mb$.

## 4.2 Event Reconstruction and Particle ID

In order to proceed from the various digital and analogue signals that constitute the raw data obtained from each of the detector components, a program must be implemented which is capable of processing the abstract electronic data and interpreting it in terms of reconstructed physics objects. At DØ the software package which accomplishes this task is called "DORECO". Within DORECO initial particle assignments are made in conjuction with the calculation of assco-ciated kinematic quantities. The criteria imposed for partcle id's are sufficiently loose at this stage that widely differing analyses are able to be undertaken without fear of losing key information that might have been compromised otherwise.

### 4.2.1 Central Tracking Reconstruction

Track reconstruction in the CD begins with raw FADC (Fast Analog to Digital Coverter) data stored in Zebra bank data structures called CDDn (n=1 VTX, n=2 CDC, n=3 FDC, n=4 TRD). Pattern recognition and track reconstruction procedures are broadly similar for each of the 4 CD subdetectors, therefore for brevity we shall only discuss the reconstruction method used in the CDC.

CDC data processing at DØ is implemented by a collection of software routines which progressively transform FADC data in the CDD2 bank into tracks which are stored in the CDC Zebra track bank structure called DTRK. The main event processing routine proceeds through 3 phases:

- **Pulse and Hit Finding.**
- **Segment Finding.** Here a segment is defined to be a portion of the track which is in a given layer of the CDC. The CDC has 4 layers.
- **Segment Matching.** This proceeds by linking together the segments in the different layers to build the complete track candidate.

In order to perform these tasks, job initialization routines are called when starting a new run. The function of these routines is to read in and store various run control parameters as well as the necessary geometrical information relevant to the CDC detector. Once the required initialization is completed the raw FADC data is unpacked in a form which is convenient for later processing. This unpacked form labels the FADC data in terms of addresses which refer to the exact layer,sector (azimuthal portion of the CDC), and wire that correspond to the FADC digital information. Within a given layer and sector, pulse finding is performed by searching the FADC data for leading edges which are located by requiring derivatives of the signal to be above a certain threshold value. The first negative derivative is used to give the trailing edge. Pulse integrals are performed and the information is stored in another Zebra bank structure called the DCDA bank. This bank stores the drift times, pulse area, pulse width, and peak height for each of the 7 seven sense wires and 2 delay lines that comprise a cell which occupies the given layer and sector under examination. Hit finding proceeds by converting the pulse drift time information into position information after performing the proper gain corrections. Z positions are derived from the delay line read outs, while the sense wires provide the $r - \phi$ location of the hits. This process is carried out for all layers and sectors and the information is stored Zebra structures called the DSEC banks.

Once all the required hit information is collected, the process of segment finding begins. The segment finding algorithms are based upon the use of a "road" method. A road is defined by a hit in the "first" and "last" wire. This is usually wire 0 and wire 6 respectively, but this need not always be the case due to inefficiencies in the hit finding for the planes defined by these two wires. One layer is worked at a time, but all azimuthal sectors in that layer are considered simultaneously. Before considering the road however, a list of hits, ordered in $\phi$, is made for each of the seven wires 0-6. Each hit is used twice in the list due to right-left drift direction ambiguities. A loop over the hits on the first wire and a loop over the hits on the last wire is then performed in an attempt to search for segments by examining the $\phi$ difference of hits in the planes defined by the intermediate wires that are a part of the road. Straight lines in the $r - \phi$ plane are determined by the pair of hits under consideration and all intermediate wires are scanned for the hit closest to the predicted straight line. Tolerance cuts in $\phi$ are enforced in order to find the best matching intermediate hits. When sufficient matching hits are found for the candidate segment an overall X-Y fit is performed. When this process is completed for "first" equal to 0 and "last" equal to 6, the first-last wires are changed and the search is repeated again. Matching hits are tagged, and the process continues until all possible first-last wire combinations have been considered.

After constructing candidate track segments all layers are searched for segments that match in $\phi$ and whose distance computed in the median plane between the two segments is smaller than some predetermined value. One missing layer is allowed. Each time a full track candidate is found a full space track fit, including the Z coordinate is computed. Chisquare cuts are applied to the track in order to reject very low momentum track candidates. Information on the resulting track is stored in a linear structure of Zebra banks called the DTRK banks.

We must note that Vertex Reconstruction is also performed by using the CDC and VTX detectors. However we will discuss vertex reconstruction in a later chapter when we consider the calculation of muon impact parameters.

### 4.2.2 Electron and Photon Reconstruction

At DØ electrons and photons are reconstructed in exactly the same way - up to a point; the electrons have the further added requirement that there should exist a matching CD track. In reconstructing electron and photon candidates DORECO employs nearest neighbor clustering algorithms. These algorithms proceed from a list of EM towers that are ordered in terms of decreasing $E_T$. EM tower here refers to the four layers of the EM calorimeter plus the first layer of the fine hadronic calorimeter. Beginning with the highest $E_T$ tower, further nearby towers are added to the cluster until 90% of the total cluster energy is deposited in the EM section of the calorimeter, and the fraction of the energy outside the central tower of the cluster is less than 60%. The total energy of the cluster is defined as the sum of all calorimeter cells (electromagnetic and hadronic) within the cluster. The summing continues until there are no towers left with an $E_T$ above a predesignated $E_T$ threshold of 50 $MeV$. Further, the total $E_T$ of the cluster is required to be greater than 1.5 $GeV$. Once the cluster formation is completed, the centroids of these clusters are calculated from a $\log(E)$ weighted mean of the positions of those cells within the cluster that lie within the third layer of the EM calorimeter (this layer is the most finely segmented in $\eta - \phi$ space). At this point photons and electrons remain undifferentiated. In order to force the distinction DORECO requires that electron candidates must have at least one matching CDC or FDC track pointing to the cluster within a road of 0.1 ($2\pi/64$ radians) in $\phi$ and 0.1 radian in $\theta$.

In order to obtain good discrimination against hadrons, both electron and photon candidates have associated with them a covariance matrix which can be defined as follows: given a sample of N electrons or N photons let

$$M_{ij} = \frac{1}{N}\sum_{n=1}^{N}(x_i^n - < x_i >)(x_j^n - < x_j >)$$

where $x_i^n$ is the value of observable $i$ for electron (or photon) $n$ and $< x_i >$ is the mean value of observable $i$ for the sample. Observables may include such things as total energy fractions in given calorimeter layers, the $z$ position of the vertex, etc. Now define the so-called $H$ matrix by $H \equiv M^{-1}$. One may then calculate the covariance parameter

$$\chi^2 = \sum_{i.j}(x_i^k - < x_i >)H_{ij}(x_j^k - < x_j >)$$

which can be used to determine whether or not shower $k$ is electromagnetic in origin. By imposing appropriate cuts on $\chi^2$ one is able to effectively separate EM and hadronic showers. Fig.4.1 shows the distributions of $\chi^2$ for showers from test beam electrons and pions with an energy of 25 $GeV$. As the the figure shows, a good separation between electrons and pions can be made.

Because DØ has no central magnetic field, the $e^+e^-$ pairs formed from photon conversions overlap in space. However $dE/dx$ (ionization per unit length) mea-

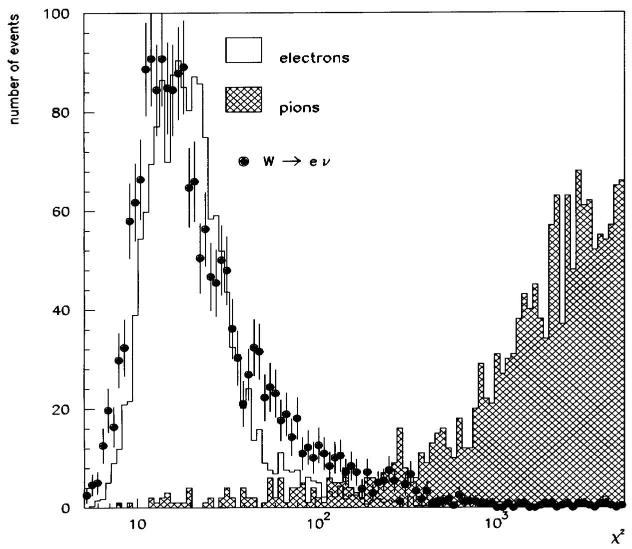


Figure 4.1: $\chi^2$ distribution for test beam electrons (unshaded), test beam pions (shaded), and electrons from $W$'s (dots)

surements in the CD detectors may be used to distinguish such multiple tracks from single tracks.

DORECO computes many quality indicators associated with electron and photon candidates. Quantities such as cluster EM fractions, cluster isolation variables, track matching significance between CD tracks and associated calorimeter clusters, and various longitudinal and transverse shower shape cuts (using $H$ matrix techniques) have all been used by various analyses in order to ensure good electron and photon id. More detailed descriptions of $H$ matrix techniques may be found in ref [59].

### 4.2.3 Jets and Missing $E_T$

Jets are clusters or groups of fairly well collimated particles which are produced from the hadronization of final state partons that have been generated in hard parton interactions. There are two types of algorithms used to define jets at DØ : the cone algorithm, and the nearest neighbor algorithm. We will discuss only the cone algorithm, since that is the one actually used in this analysis. The energy deposited by the parton fragmentation products that constitute the jet is distributed over a region of calorimeter cells. The pattern of this distribution can be empirically desribed in terms of cones in $\eta - \phi$ space. The parameters that define the jet cone are its radius and the direction of its axis. The radius of the cone is given by $\Delta R = \sqrt{\Delta\eta^2 + \Delta\phi^2}$. Cones of differing radii may be used, however the one used in this analysis is the cone of radius $\Delta R = 0.7$.

The jet finding algorithms employed by DORECO begin the reconstruction process with a list of calorimeter towers (typically $0.1 \times 0.1$ in $\eta \times \phi$) that are ordered in decreasing values of $E_T$ (here $E_T = \sum_i E_i \sin(\theta)$ where $i$ ranges over the calorimeter cells that comprise the tower and whose observed energy deposition is given by $E_i$ and where $\theta$ represents the polar coordinate of the tower center). Preclusters are formed from all nearby towers that lie within a radius of $\Delta R = 0.3$ about the direction of the highest $E_T$ tower (provided the $E_T$ of these nearby towers exceeds the threshold value of 1 $GeV$). The center in $\eta - \phi$ space of the precluster serves as the initial direction of the jet while the summed $E_T$ of all towers within the precluster gives the initial value of the jet $E_T$. Next all towers within the defining $\Delta R$ cone size of this preliminary jet are examined and their $E_T$'s are added to the initial jet $E_T$ to form a new jet $E_T$. At the same time a new $E_T$ weighted center is recalculated for the jet by using the added towers. These steps are repeated until the jet so formed appears to remain stable. Jets constructed in this manner are merged if they share more than 50% of their energy and split otherwise. Finally an $E_T$ threshold of 8 $GeV$ is imposed on all reconstructed jets.

The jet energy resolution has been measured from the collider data by examining the transverse momentum balance between two jets. The jet $E_T$ resolution may be parametrized as follows:

$$(\frac{\sigma}{E_T})^2 = C^2 + \frac{S^2}{E_T} + \frac{N^2}{E_T^2} \tag{4.1}$$

where $C$ is an error term from the calibration, $S$ represents the shower fluctuations in the sampling gap, and $N$ denotes the contribution due to noise and the underlying event. For example, in the CC we have that: $C = 0, S = 0.74\sqrt{GeV}, N = 2.16\ GeV$.

Jet energy scale corrections [56] are calculated using a technique developed by the CDF collaboration [57]. These corrections have been estimated by studying the $E_T$ balance in samples of direct photon events where a photon is back-to-back in $\eta - \phi$ with a jet. Here it is assumed that $\not{E}_T \sim 0$, and that the electromagnetic energy response is correctly calibrated. One further assumes that the measured $\not{E}_T$ is then due to the incorrect response of the calorimeter to the jet as compared with its response to the photon. On the basis of these assumptions the difference between the true jet $E_T$ and the measured jet $E_T$ is ascribed to the component of $\not{E}_T$ along the direction of the jet ($\hat{n}_T^{jet}$). That is,

$$E_T^{true} - E_T^{jet} = \vec{\not{E}}_T \cdot \hat{n}_T^{jet} \tag{4.2}$$

One can then define a correction factor which may be used to convert from measured jet energy to the true jet energy by

$$E_T^{true} = (1 + \frac{\vec{\not{E}}_T \cdot \hat{n}_T^{jet}}{E_T^{jet}}) \cdot E_T^{jet}$$

The ratio

$$\frac{\vec{\not\!\!E}_T \cdot \hat{n}_T^{jet}}{E_T^{jet}} \equiv MPF$$

is called the missing $E_T$ projection fraction.

Because neutrinos carry no charge and are extremely weakly interacting, the DØ detector has no way of detecting them directly. One must therefore examine the momentum imbalance in an event in order to infer the presence of neutrinos. However the measurement of longitudinal momenta is inaccurate because of particles being lost down the beam pipe and because of our ignorance concerning the longitudinal momenta of initial state partons. Therefore momentum conservation can be usefully applied only in the plane transverse to the beam, that is one must look at transverse energies and carefully examine any observed imbalances in order to establish the presence of neutrinos in the event. Thus the DORECO reconstruction algorithms for neutrinos proceeds in an indirect fashion and relies upon measurements of Missing $E_T$ (denoted by $\not\!\!E_T$).

The momentum of the neutrino is calculated by summing vectorially all the transverse energy in the calorimeter cells. A preliminary transverse momentum of the neutrino is then calculated as the negation of these sums, that is we have

$$\not\!\!E_x^{cal} = -\sum_i E_i \ \sin(\theta_i) \ \cos(\phi_i)$$

$$\not\!\!E_y^{cal} = -\sum_i E_i \ \sin(\theta_i) \ \sin(\phi_i)$$

with

$$\not\!\!E_T = \sqrt{(\not\!\!E_x^{temp})^2 + (\not\!\!E_y^{temp})^2}$$

and where $i$ runs over all cells in the calorimeter, with $E_i$,$\theta_i$, and $\phi_i$ denoting the energy deposit, and the polar and azimuthal coordinates respectively of cell $i$.

This temporary estimate of the neutrinos transverse momentum is then corrected by including the vector components of all muons in the above sum while subtracting out their expected energy depositions (since the above calorimeter sums include the energy deposited by the muons). Thus the muon-corrected estimate of the missing $E_T$ is given by

$$\not{E}_x = \not{E}_x^{cal} - \sum_{\mu}(p^{\mu} - E^{dep})\ \sin(\theta_{\mu})\ \cos(\phi_{\mu})$$

$$\not{E}_y = \not{E}_y^{cal} - \sum_{\mu}(p^{\mu} - E^{dep})\ \sin(\theta_{\mu})\ \sin(\phi_{\mu})$$

$$\not{E}_T = \sqrt{(\not{E}_x)^2 + (\not{E}_y)^2}$$

where $p^{\mu}, E^{dep}, \theta_{\mu}$, and $\phi_{\mu}$ denote respectively the muon momentum, energy deposition, and polar and azimuthal angles.

The $\not{E}_T$resolution of the DØ calorimeter may be parametrized as

$$\sigma_{\not{E}_T} = a + b \cdot S_T + c \cdot S_T^2$$

where $a = 1.89 \pm 0.05\ GeV, b = (6.7 \pm 0.7) \times 10^{-3}, c = (9.9 \pm 2.1) \times 10^{-6} GeV^{-1}$, and where $S_T$ is the scalar sum of the transverse energy in the calorimeter [58].

### 4.2.4 Muon Reconstruction

The raw data collected by the muon system consists of a digital pad-latch indicating a possible hit, and a series of analogue signals that represent the drift time, delta time, and cathode pad charges associated with the recorded pad-latch signal. This information is stored in a zebra bank structure called MUD1. In order to reconstruct muon candidates, the muon reconstruction algorithms must: (1) first convert this information into hits located in space relative to the global

DØ coordinate frame; (2) perform pattern recognition searches on the reconstructed hits in order to arrive at possible muon track candidates; (3) assign hits to the best possible track and link this track with information gathered from the Central Detector and the Calorimeter.

1) Initially a loop is made over the raw data in MUD1 to determine if any of the data appears to be corrupted. Determinations are made as to which WAMUS or SAMUS chambers have been hit. Hit chambers are then looped over and corrections are made for the time and delta time constants. Pad latch bits and time information is used to assign a hit to either the even or the odd cell (or both) of the ganged cell pair. Good hits are required to have at least one pad latch set and a physical drift time. Corrections are then made to the pad values for pedestals and gains. Drift times are corrected for time-of-flight and then converted to drift distances. At this point there still exists a left-right ambiguity in the drift distances, and a similar two-fold ambiguity exists in the vernier pad solutions derived from the corrected cathode pad values and their associated charge ratio (as described in Chapter 3). At this stage the two solutions for the drift time are considered as separate hits.

2) Tracks are found separately in both the bend and the non-bend views. In the non-bend view a straight line fit through the magnet is assumed. Delta times are used to seed a possible list of vernier pad solutions. Those pad solutions that minimize the quality of the fit are assumed to be the correct pad solutions. The bend view assumes two straight line fits with the two lines constrained to meet in the magnet center. Here the drift distances are used in conjunction with the fit to remove left-right ambiguities. A road algorithm is used and the hits are required to be on the tracks in both views. All segments are required to point

to the interaction vertex (within 3-5 m). In the bend view, BC layer segments are searched for first and are required to have a minimum of 4 planes (out of 6 possible) allowing for only one hit per plane. Matching A layer segments are then searched for next, where the A layer segment is required to have at least 2 planes (out of a possible 4). If no A segment is found, then the BC segment projected to the magnet center together with the vertex point is used to define the segment inside the magnet. If no BC segment is found, then the search starts for an A layer segment which is then extended into the B or C layer. Tracking is done by quadrants allowing for up to 6 tracks per quadrant.

3) At this point the muon track is extrapolated back into the calorimeter and the energy along the traversed cells and their nearest neighbors is summed to account for the muon energy loss. The bend angle from the track in the bend view is used in conjunction with the known magnetic field to determine the muon momentum. This initial determination is then corrected for the muon energy loss by employing look up tables. A series of track quality flags is set which indicate the quality of the fit (in both views) and the quality of the track projection to the vertex. Further muon quality words such as the integral $\int \vec{B} \cdot d\vec{l}$ (which can act as an indicator of the goodness of the muon momentum determination) are recorded in zebra bank structures associated with each muon track candidate.

The above calculations concerning muon track reconstruction refer only to the muon system itself, that is the track reconstruction is local to the muon system. The final muon track and momentum calculations are done by a global fit[53]. This global fit makes use of the following measurements:

- 2 VTX measurements of the vertex point $(VY, VZ)$.

- 4 CD measurements which give the slope and intercept of the best matching CD track in $XY$ and $RZ$ views.

- 2 Angle "measurements" (the means are set to zero) describing the Multiple Coulomb Scattering that occurs in the Calorimeter.

- 4 tracking measurements giving slope and intercept in both views for Muon System A-layer tracks.

- 4 tracking measurements giving slope and intercept in both views for Muon System BC-layer tracks.

In total then, there are 16 measurements:VTX(2),CD(4),MCS(2),A-Layer(4), BC-Layer(4). The offline global fitting algorithms then attempt a standard least-squares fit of the global muon track in terms of 7 fit parameters:

- 4 parameters for the muon track in the CD.

- 2 parameters describing the deflection of the muon in the Calorimeter due to Multiple Coulomb Scattering.

- 1 parameter - $1/p$ the inverse of the muon momentum.

Approximately 70% of the locally determined muon track candidates can be successfully globaly fitted in the manner described above. If a muon can be globaly fitted then the results of the global fit are used to overwrite the zebra bank contents that are used to summarize the important parameters that desribe each local muon candidate.

The muon momentum resolution is primarily determined by two components: the multiple Coulomb scattering that occurs in the iron toroids, and the resolution of the measured space points. Secondary effects due to chamber inefficiencies and geometrical misalignment also tend to degrade the momentum resolution. The resolution of the muon momentum may be parametrized as follows:

$$(\frac{\delta p}{p})^2 = (\frac{0.18(p-2)}{p})^2 + (0.008p)^2 \tag{4.3}$$

The first term desribes the limit on the resolution due to the effects of multiple Coulomb scattering. Space point drift resolution on the order of $\sim\ 2\ mm$, and chamber alignment errors on the order of $\sim\ 3\ mm$ are reflected in the second term above. This parametrization was determined by comparing $Z^0$ dimuon data with Monte Carlo simulated events which were tuned until the width and tails of the $Z^0$ data could be satisfactorily reproduced[54][55]. Thus the resolution for low momentum muons is dominated by multiple Coulomb scattering, whereas high momentum muons have their resolution primarily limited by the effects of space point drift resolution and small bending angles which become more difficult to measure.

## 4.3 Monte Carlo Event Simulation

Monte Carlo event generators constitute an extremely important and commonly used class of tools utilized by high energy particle physicists. The term "Monte Carlo" refers to numerical simulations of processes that may be characterized by sets of random variables. These variables assume values in accordance with prescribed probability distributions. The distributions themselves are based upon the process of random number generation. These techniques may be used to simulate the collision of interacting hadrons and to model the observation of the scattered collision products within an appropriately designed detector. For hadron-hadron collisions, the most commonly used Monte Carlo event generators are ISAJET, PYTHIA, and HERWIG [60]. Each of these generators follow the same basic approach in modeling high energy hadron-hadron collisions. Furthermore, since all Monte Carlo event generation used in this thesis is based upon ISAJET, only the latter event generator will be described in any detail.

### 4.3.1 ISAJET Monte Carlo

The main function of ISAJET is to simulate $p-p$ and $p-\bar{p}$ collisions and to model the attendant hard parton-parton scattering processes that follow. It is based upon perturbative QCD cross sections, leading order QCD radiative corrections for initial and final state partons, and phenomenological models for jet and beam jet fragmentation. ISAJET simulates events in four distinct steps which will now be desribed in turn.

#### Hard Scattering

The hard scattering that occurs between the parton constituents of the colliding hadrons is described in terms of amplitudes and cross sections that have been derived from lowest order scattering matrix elements computed in perturbative QCD. These cross sections, $\hat{\sigma}$, are then convoluted in the usual manner with the parton density distributions, $f_i(x, Q^2)$, that is

$$\sigma = \int dx_1 dx_2 \hat{\sigma}_{ij} f_i(x_1, Q^2) f_j(x_2, Q^2)$$

As usual $x_1$ and $x_2$ denote the parton momentum fractions and $Q^2$ denotes the momentum transfer squared. The default structure functions $f_i$ are those of Eichten, Hinchliffe, Lane, and Quigg (EHLQ) [61].

### QCD Evolution

The evolution process in ISAJET is used to simulate both initial and final state radiative corrections to the basic hard scattering process. The evolution is based upon a branching algorithm introduced by Fox and Wolfram [62]. Both initial and final state partons are allowed to undergo repeated parton branchings. The probability that a branching $a \to bc$ occurs during a small change in the evolution parameter $dt(t = p^2)$ is given by the Altarelli-Parisi equations

$$\frac{dP}{dt} = \int dz \frac{\alpha_s(p^2)}{2\pi} P_{a\to bc}(z)$$

where $P_{a\to bc}(z)$ represents the splitting function, and $z$ denotes the momentum fraction of the initial parton $a$ carried off by $b$ say. The evolution process starts with the maximum allowed value for $t(t = t_0 = p_a^2)$ and then solves for that value of $t(t = t_1)$ at which the branching occurs. The value of $t_1$ is determined from the probability $\Pi(t_0, t_1)$ for evolving from an initial mass $t_0$ to a final mass $t_1$ while emitting no parton radiation. That is, if

$$\Pi(t_0, t_1) = \frac{\alpha_s(t_0)}{\alpha_s(t_1)}^{2\gamma(z_c)/b_0}$$

where

$$\gamma(z_c) = \int_{z_c}^{1-z_c} dz P(z)$$

with $z_c$ expressed in terms of $t_c$(a suitable cutoff value for $t$), then $t_1$ may be derived from the derivative $\Xi(t_1) = \partial\Pi(t_0, t_1)/\partial t_1$, since this gives the distribution for the mass $t_1$ at which the first resolvable radiation occurs. After $t_1$ for the first branching is chosen, a new $z$ for the next branching is selected according to $P(z)$, and the masses of the two new partons $b$ and $c$ are evolved starting from $zt_1$ and $(1-z)t_1$ respectively. The products $b$ and $c$ are then allowed to branch and so on.

The branching process is stopped when a parton mass is evolved below the cutoff $t_c = 6\ GeV^2$.

**Hadronization**

As discussed earlier, the quarks form the fundamental representation of $SU(3)_c$, while the gluons constitute the adjoint representation of $SU(3)_c$. They are therefore not color-singlet states. Color confinement in QCD postulates that only color-singlet hadronic states are observable. Thus ISAJET must combine the partons formed during the QCD evolution process into the colorless mesons and baryons that are actually found to exist in nature. The process of forming color-singlet hadrons from the colored partons is called hadronization or fragmentation. Fragmentation is an intrinsically non-perturbative process and various phenomenological models are used. The approach adopted by ISAJET is based upon the Feynman-Field independent fragmentation model [63]. Given a quark $q$ with momentum $p$, a $q'\bar{q}'$ pair is generated. The $q$ and $\bar{q}'$ are combined to form a meson with energy fraction $z$. The leftover quark $q'$ (with energy fraction $1 - z$) is then fragmented in the same way. The process continues until the energy left falls below some cutoff value. Light quarks are generated according to the ratio $u : d : s = 0.4 : 0.4 : 0.2$, with the energy fraction $z$ being distributed according to

$$D(z) = 1 - a + a(b+1)(1-z)^b, a = 0.96, b = 3$$

Heavy quarks $Q$ (b,c, and t) are fragmented with $z$ being generated according to the Peterson form

$$D_Q(z) = \frac{1}{z[1 - 1/z - \epsilon/(1-z)]^2}$$

where $\epsilon = 0.5\ GeV^2/m_Q^2$. Baryons are formed by generating diquark pairs with a total probability of 0.08.

### Beam Fragmentation

Beam jet fragmentation refers to the process of hadronizing those leftover partons within the colliding hadrons that did not participate in the initial hard scattering process. After hadronization these spectator partons will form the bulk of what is referred to as the "underlying event". They must be evolved and hadronized according to some prescription which attempts to match the observed phenomenology of such underlying events. There is no concensus as to how this should be done since again the whole process is essentially non-perturbative in character. Many of the major differences between the various Monte Carlo event generators center about this problem of beam jet fragmentation. The approach taken by ISAJET is to simply superimpose a minimum bias event upon the hard scattering event.

## 4.3.2 Simulation of the Detector and Triggers

A full simulation of the DØ detector and its associated triggers is necessary for several reasons: (1) geometrical acceptances for a given physics process may be accurately determined provided the detector's geometrical setup can be adequately modeled in sufficient detail; (2) the systematic effects of detector smearing may be studied thus allowing for an assesment of the resolutions to be expected in various signals of interest; (3) studies of signals versus backgrounds may be carried out and the effects of various cuts designed to enhance signal to background ratios may be estimated.

### Detector Simulation

The simulation of the DØ detector is done with a program called DOGEANT which is a customized version of the CERN Program Library package known as

GEANT [64]. The GEANT program is able to accurately simulate the tracking of particles through complicated user-specified detector setups. The interactions of particles are modeled in terms of various physics processes that include $\delta$-ray production, multiple Coulomb scattering, full electromagnetic and hadronic showering, electron and muon bremsstrahlung, and decays. GEANT is able to simulate the response of various detector components to the above mentioned processes in terms of digitized signals and this is all done in a manner which closely parallels the actual raw data acquisition process.

In order to make it more flexible and to allow for easier modification, DOGEANT does not hard code the geometrical setup of the detector, but rather places all the required information in sets of ASCII files known as Run Control Parameter (RCP) files. The geometry of the DØ muon detector is simulated in great detail down to level of sense wires, cathode material, support structures, etc. Naturally, however, a compromise must be made between the amount of CPU time required to track particles through many complicated geometrical volumes, and the level of detail required in order to insure an accurate modeling of the physics and the detector response. For example, a full simulation of showering in the calorimeter would require that DOGEANT track hundreds of secondaries through large numbers of uranium plates and argon gaps. Hence an approximation of the calorimeter is used instead. The full structure of the supports and individual modules is preserved, but the contents of the modules are modeled as homogeneous blocks of uranium-G10-argon mixture (with the correct average atomic weight). This greatly reduces the number of volumes and therefore speeds up the tracking. Within the calorimeter sampling fluctuations are added after showering for each track, and appropriate hadron to electron response (as determined from test beam results) is introduced. Electromagnetic showers are allowed to evolve until the individual secondaries fall below 200 $MeV$ at which point the energies are determined from simple parametrizations.

#### Trigger Simulation

The simulation of the DØ Level 1 and Level 2 trigger system is done by utilizing two packages called L1SIM and L2SIM respectively. The packages possess the flexibilty to operate on either actual or Monte Carlo raw data. L1SIM uses simulated Level 1 trigger elements and a simulated AND-OR network. L2SIM simulates the Level 2 software trigger system, in fact the code used in L2SIM is essentially that used by the actual Level 2 trigger except that it is written in standard VMS rather than the compact Level 2 language of VAXELN. The input trigger configuration files used by L2SIM are identical to those actually used by the Level 2 trigger [65].

### 4.3.3 Corrections to the Monte Carlo Simulations

The simulated Monte Carlo events that are produced by DOGEANT suffer from several deficiencies that prevent them from being a truly accurate representation of the real data. It has been found that several refinements to the calorimeter and muon simulations are required in order to simulate the data in a more realistic fashion. These refinements center mainly on the problems due to various sources of noise and periodically varying calibration and survey constants. In the folllowing we will therefore discuss the remedies that DØ currenly employs.

### The Noisy Package

DOGEANT output does not include the effects due to calorimeter noise and multiple interactions. A set of packages called NOISY have been designed with the intention of adding noise from several sources to the calorimeter output of DOGEANT. These sources of noise include those produced by the uranium construction of the calorimeter and also the effects due to electronics noise. Further degradations of calorimeter signals can be made in order to simulate the effects due to multiple interactions in the bucket in which an event has ocurred as well as the pileup from events in other buckets. Noise is added cell by cell to the GEANT output and a new set of calorimeter raw data banks (CAD banks) is made.

The uranium and electronics noise contributions can be modeled in terms of a gaussian smearing done in each calorimeter cell, or else in terms of a model based upon pedestal distributions derived from cosmic ray data. Multiple interactions and event pileup is simulated by using a second event input stream. By using the average number of interactions per bucket a Poisson probabilty $P(N)$ may be calculated for getting $N$ interactions per bucket so that for each signal event an appropriate number of additional events may be read in from the pileup stream and added cell by cell to the current signal event using properly adjusted weights.

### The MU-SMEAR Package

The MU-SMEAR package has the purpose of doing further smearing to DOGEANT Monte Carlo data in order to mimic the real detector resolution. It attempts to account for those sorts of inefficiencies which cannot and should not be applied in the Monte Carlo generation (for example, blown AC fuses on low-voltage power supplies, or chamber gas leaks and so on).

DOGEANT assumes the design resolution of the muon system to be

$$(\frac{\delta P}{P})^2 = (0.18)^2 + (0.001P)^2$$

However the actual muon system momentum resolution is not this good. For example, for muon momenta in the range $40 - 50$ $GeV$ the resolution is close to 50% whereas DOGEANT would produce a resolution of only about 19%. These differences are due primarily to factors such as alignment uncertainties, drift time resolutions, pad latch inefficiencies, and the myriad of smaller cumulative effects mentioned earlier.

To account for all these sources of inefficiency the MU-SMEAR package was designed to do three things. First, it smears the raw muon data bank (MUD1) in order to worsen the time and delta time electronics resolutions. GEANT Monte Carlo has a drift time position resolution of 20 $\mu m$ and a time division resolution of 12 $cm$. However, Run 1A data showed typical values of 70 $\mu m$ and 20 $cm$ respectively for the drift time and time division position resolutions. Second, the package drops hits from MUD1 in order to simulate chamber inefficiencies. Again, Run 1A data indicated that most chambers were about 90% efficient with the exception of the EF B layer and C layer chambers which appeared to be only $\sim 50\%$ efficient. GEANT assumes essentially 100% efficiency for all chambers. Third, the package modifies muon geometry files so as to effect a deliberate misalignment of chamber positions. A typical value of 3 $mm$ misalignment (in the drift direction only) was needed in order have GEANT Monte Carlo for $W \rightarrow \mu + \nu$ and $Z \rightarrow \mu + \mu$ muon distributions match DORECO (version 11) data.

# Chapter 5

# Generated Monte Carlo Samples

Certainly the $J/\psi$ has been known for a long time, but it has never been studied at the energies provided by the Tevatron. Might it be possible that unexpected production mechanisms will begin to manifest themselves? Will the models that have served well in the past continue to be sufficient to explain all that is observed about the $J/\psi$ ? In order to answer these questions and to gain our bearings in this new landscape we need an initial foothold. We must proceed from what we believe we already know and attempt to put forward our best guesses at to what to expect concerning the $J/\psi$ and our detectors response to it. In this chapter we address the problem of simulating $J/\psi$ production at the Tevatron and modeling its subsequent observation in the DØ detector.

In order to study the $J/\psi$ a number of different Monte Carlo samples were generated. These include samples that serve to characterize not only the $J/\psi$ signal itself, but also the attendant physics processes that accompany the $J/\psi$ and act as a source of important background. In this chapter we discuss the six different Monte Carlo samples that were generated using ISAJET (version 6.49). The processes simulated were the following:

- B-produced $J/\psi$.

- $\chi_c$-produced $J/\psi$.

- Heavy Quark $Q\bar{Q}$-produced dimuons.

- Drell Yan dimuons.

- Low Mass Mesons $(\rho, \phi, \omega, \eta, \eta^{'})$.

- Dimuons arising from $\pi - K$ decays.

For each process we parametrize the distributions of certain selected physics variables of interest. These parametrizations are then used in later chapters in conjunction with the method of Maximum Likelihood in order to determine the relative contribution of each process to the distributions observed in the dimuon data. The distributions are:

- **$M_{\mu\mu}$, the invariant mass of unlike sign dimuons.**

- **$p^T_{\mu\mu}$, the transverse momentum of the dimuon system.** We note here for future reference that this distribution will **not** be used in the Maximum Likelihood Fits, rather we intend to **predict** dimuon $p_T$ distributions obtained on the basis of the likelihood fits to the other 3 distributions described here.

- **$p^T_{\mu\mu\ Rel}$, the momentum of the dimuon transverse to the direction of its associated jet.** A dimuon is said to have an associated jet if there is a reconstructed jet within an $\eta - \varphi$ cone of radius $R = \sqrt{\Delta\eta^2 + \Delta\varphi^2} = 0.7$ about the direction of the dimuon. If the dimuon has no asscociated jet, then an entry is made in the first bin of this distribution.

- $I_{\mu\mu}^{2NN}$, **the 2 nearest neighbor calorimeter isolation variable.** This quantity is calculated as follows: for each muon of the dimuon pair we calculate the difference between the 2 nearest neighbor energy deposition observed in the calorimeter and the energy loss expected for a minimum ionizing particle of that energy and momentum. If the other muon of the pair lies within an $\eta - \varphi$ cone of radius $R = 0.6$ about the direction of the muon of current interest, then the energy loss expected for that muon is subtracted as well. That is, for the muons constituting the dimuon pair we form the quantities

$$I_{\mu 1\ Cal}^{2NN} = E_{\mu 1\ Cal}^{2NN} - E_{\mu 1\ expected} - E_{\mu 2\ expected} \tag{5.1}$$

$$I_{\mu 2\ Cal}^{2NN} = E_{\mu 2\ Cal}^{2NN} - E_{\mu 2\ expected} - E_{\mu 1\ expected} \tag{5.2}$$

  where the last term in each expression is present provided the other muon is within a cone of radius $R = 0.6$ about the direction of the first. Finally $I_{\mu\mu}^{2NN}$ is defined to be equal to the value of $I_{\mu\ Cal}^{2NN}$ for that muon which is closest in direction to the direction of the dimuon.

A set of muon id and dimuon selection cuts has been imposed on each of the Monte Carlo samples to be discussed below. These cuts are described in detail in the next chapter. Each sample has been run through DOGEANT (version 3.14), then run through DORECO (version 11.19), and finally run through L12SIM (global trigger configuration file V7.2). Additionally each sample has been corrected by running it through the NOISY and MU-SMEAR packages. They should therefore represent a complete simulation of the entire DØ detector and trigger system.

## 5.1 Simulation of the Production of $J/\psi$ Mesons

The present understanding of $J/\psi$ production at Tevatron energies supposes that there are at least three different mechanisms involved: (1) The BPM mechanism; (2) The CPM mechanism; and (3) The Fragmentation mechanism. ISAJET Monte Carlo has been used to simulate the first two listed production mechanisms, however no Monte Carlo package is presently available that will allow for the simulation of $J/\psi$ production via the Fragmentation mechanism. Therefore we will briefly discuss those Monte Carlo samples that have been used to help model the production of the $J/\psi$ through the CPM and BPM mechanisms.

### 5.1.1 Simulation of BPM $J/\psi$ Production

The standard ISAJET (version 6.49) Monte Carlo package was used. The hard scattering process was taken to be "Two Jet" with the Jet $p_T$ range given by $7\ GeV/c < p_T^{jet} < 80\ GeV/c$. Events were evolved up to 10 times requesting that there be a heavy $b$ and/or $c$ quark present in the event. Various attempts at hadronization were made until a $J/\psi$ was determined to be present in the event. The $J/\psi$ was forced to decay to a pair of opposite sign muons, that is the process selected was

$$p\bar{p} \rightarrow b + X \rightarrow J/\psi + X \rightarrow \mu^+\mu^- + X$$

The relevant branching ratios used by ISAJET are

$$Br(b \rightarrow J/\psi + X) = 1.12\%, \quad Br(J/\psi \rightarrow \mu^+\mu^-) = 7.04\%$$

The number of events generated in the ISAJET sample used for the acceptance and efficiency calculations in this thesis was 38000.

In Fig.5.1 we show the distributions of the 4 different physiscs variables of interest for later data anlysis. We note that the $J/\psi$ mass is well fitted by a Gaussian of width $\sigma = 0.38\ GeV/c^2$, with a mean value of $M_{J/\psi} = 3.053 \pm 0.005\ GeV/c^2$. This corresponds to a mass resolution of approximately 12%.

### 5.1.2 Simulation of CPM $J/\psi$ Production

In order to simulate the production of $J/\psi$'s via the CPM mechanism, a modified version of the standard ISAJET Monte Carlo was used. This Monte Carlo version is called the ISACHI package. It is essentially ISAJET but with the standard Combridge hard scattering matrix elements replaced by those of Humpert. These latter matrix elements simulate the cascade production of $J/\psi$'s via the following processes

$$p\bar{p} \to \chi_{c_0} + X \to J/\psi + \gamma + X, \quad Br(\chi_{c_0} \to J/\psi + \gamma) = 0.66\%$$

$$p\bar{p} \to \chi_{c_1} + X \to J/\psi + \gamma + X, \quad Br(\chi_{c_1} \to J/\psi + \gamma) = 27.3\%$$

$$p\bar{p} \to \chi_{c_2} + X \to J/\psi + \gamma + X, \quad Br(\chi_{c_2} \to J/\psi + \gamma) = 13.5\%$$

Again the $J/\psi$ was forced to decay to $\mu^+\mu^-$ pairs. The $p_T$ range chosen for the $\chi_c$ states was $4\ GeV/c < p_T^{\chi} < 40\ GeV/c$. The number of events generated in the ISACHI sample used for the acceptance and efficiency calculations in this thesis was 20000. Fig.5.2 shows the distributions of the 4 different physics variables of interest for later data analysis.

Table 5.1 summarizes the $J/\psi$ Monte Carlo samples that were generated.

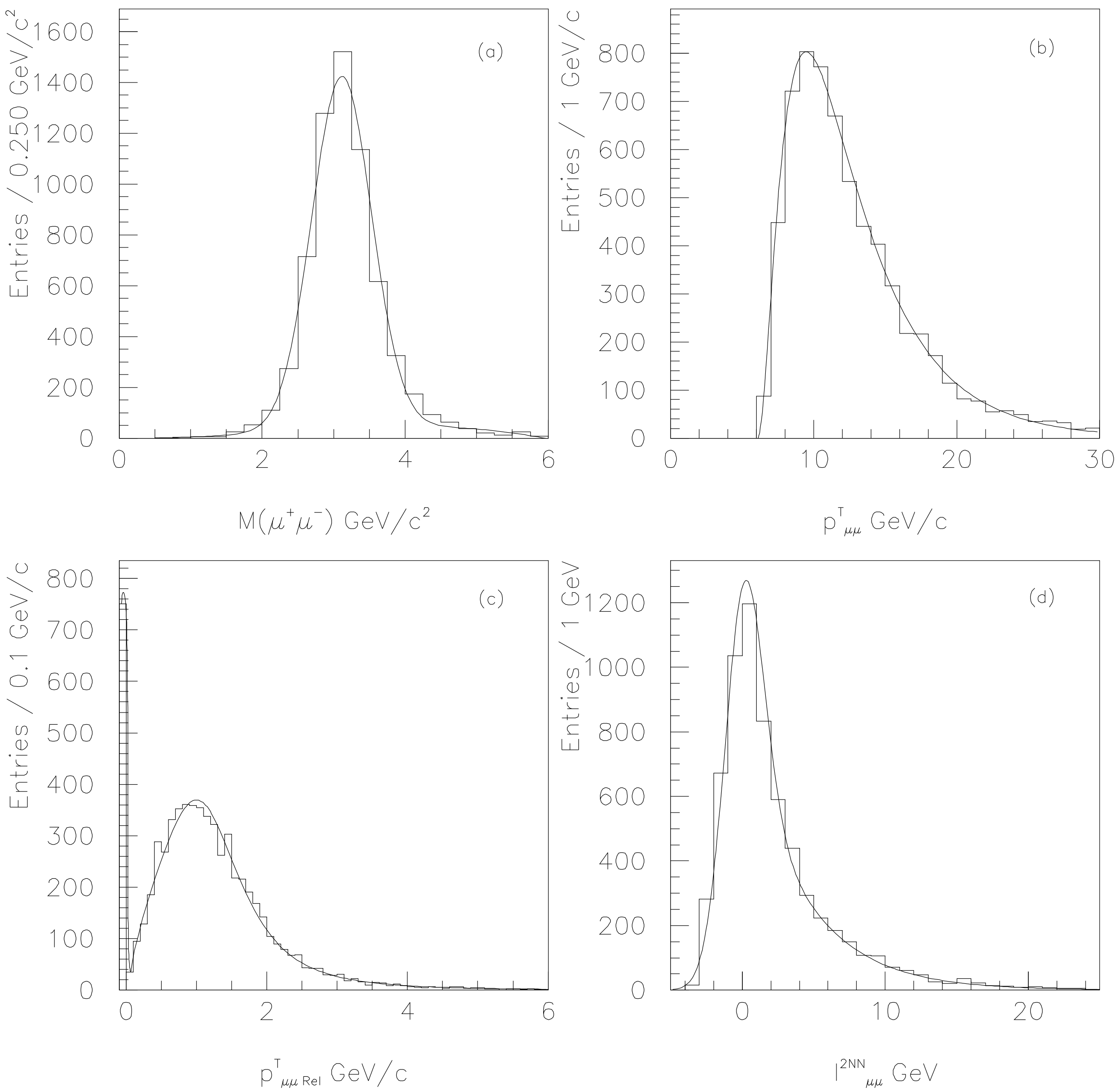


Figure 5.1: Distributions from B-produced $J/\psi$ Monte Carlo. (a) Invariant Mass (b) Dimuon $p_T$ (c) Dimuon $p_{TRel}$ and (d) Dimuon Isolation. Superimposed on the plots are parametrized fits.

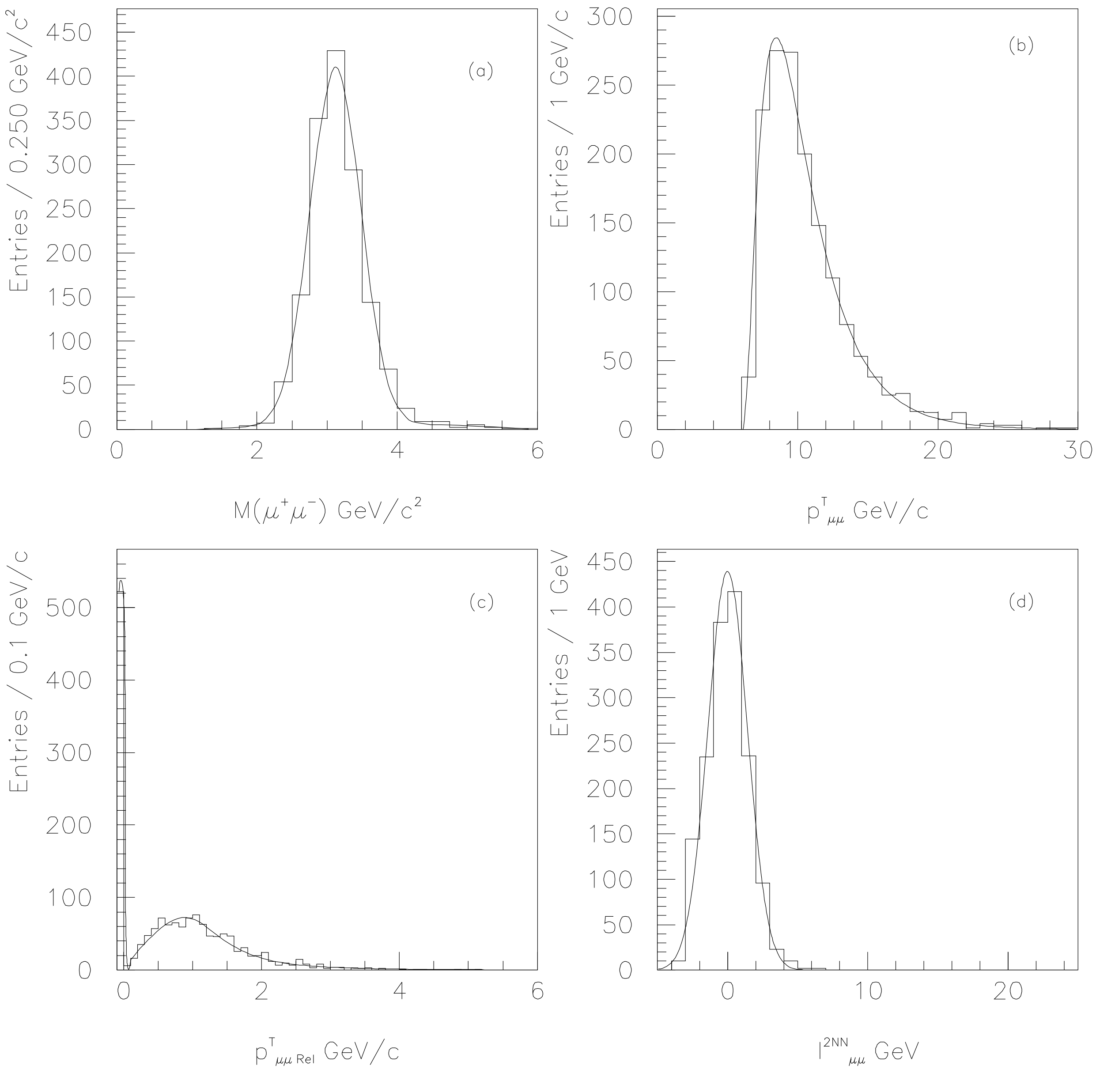


Figure 5.2: Distributions from $\chi_c$-produced $J/\psi$ Monte Carlo. (a) Invariant Mass (b) Dimuon $p_T$ (c) Dimuon $p_{TRel}$ and (d) Dimuon Isolation. Superimposed on the plots are parametrized fits.

| $J/\psi$ Production Process | $p_T$ Range | Events Generated |
|---|---|---|
| $b \to J/\psi + X$ | $7\ GeV/c\ < p_T^{jet} < 80\ GeV/c$ | 38000 |
| $\chi_c \to J/\psi + \gamma$ | $4\ GeV/c\ < p_T^{\chi} < 40\ GeV/c$ | 20000 |

Table 5.1: ISAJET Monte Carlo samples used to study $J/\psi$ production

## 5.2 Heavy Quark $Q\bar{Q}$-Produced Dimuons

Heavy Quark ($b$ and $c$) production is expected to be a significant source of background to the $J/\psi$ signal at the Tevatron Collider. The cross sections for $b$ and $c$ production are of comparable value, on the order of $30 - 40\ \mu b$. However due to the harder fragmentation function for $b$-quark hadronization, the yield of muons tends to be higher in processes involving $b$-quark production.

The dimuons associated with $b$ quark production arise from two principle topologies involving semileptonic $B$-hadron decays. These two distinct topological forms may be referred to as: (1) Parallel B semileptonic decays, and (2) Sequential B semileptonic decays.

In parallel decays we have each of the two jets ($b$ and $\bar{b}$) contributing a muon through the underlying process

$$b \rightarrow c + W^- \rightarrow c + \mu^- + \bar{\nu}_\mu \tag{5.3}$$

$$\bar{b} \rightarrow \bar{c} + W^+ \rightarrow \bar{c} + \mu^+ + \nu_\mu \tag{5.4}$$

For sequential decays only one of the $b$ jets contributes according to the process

$$\begin{aligned} b &\rightarrow c + \mu^- + \bar{\nu}_\mu \\ &\rightarrow s + \mu^+ + \nu_\mu + \mu^- + \bar{\nu}_\mu \end{aligned} \tag{5.5}$$

In either case an opposite sign dimuon pair is produced. Parallel decays produce dimuons with relatively small $p_T$ and large opening angles between the muons. Sequential decays on the other hand, produce dimuons with larger values of $p_T$ and small opening angles between the muons. Of the two topologies, the sequential decays tend to produce the dominant background in the region of the $J/\psi$. The mass spectrum for sequential decays peaks near 2 $GeV/c^2$ and falls sharply from that value slicing through the nominal $J/\psi$ mass region of $2 - 4.4$ $GeV/c^2$, whereas parallel decays exhibit a much broader mass distribution that tends to peak near 9 $GeV/c^2$.

Again standard ISAJET (version 6.49) was used for the $Q\bar{Q}$ Monte Carlo. The hard scattering process was taken to be "Two Jet" with the Jet $p_T$ range given by 4 $GeV/c$ $< p_T^{jet} <$ 80 $GeV/c$. Events were evolved up to 10 times requesting that there be a $b$ and/or $c$ quark present in the event. Various attempts at hadronization were made until a dimuon was determined to be present in the event. The number of events generated in the ISAJET sample used in this thesis was 48000. Fig.5.3 shows distributions for the heavy quark $Q\bar{Q}$ Monte Carlo.

## 5.3 Drell-Yan Dimuon Production

The Isajet events for the Drell-Yan simulation restricted the "mass" of the virtual photon to range $0.28 - 20$ $GeV/c^2$. The transverse momentum of the virtual photon was taken in the range $0 - 80$ $GeV/c$. This range of transverse momentum values allowed for the simulation of both Leading Order (LO) and Next-to-Leading-Order (NLO) event topologies.

The LO dimuon event topology produces dimuons with small $p_T$ and large opening angles. As with the $b$-quark parallel decays, the LO events produce a

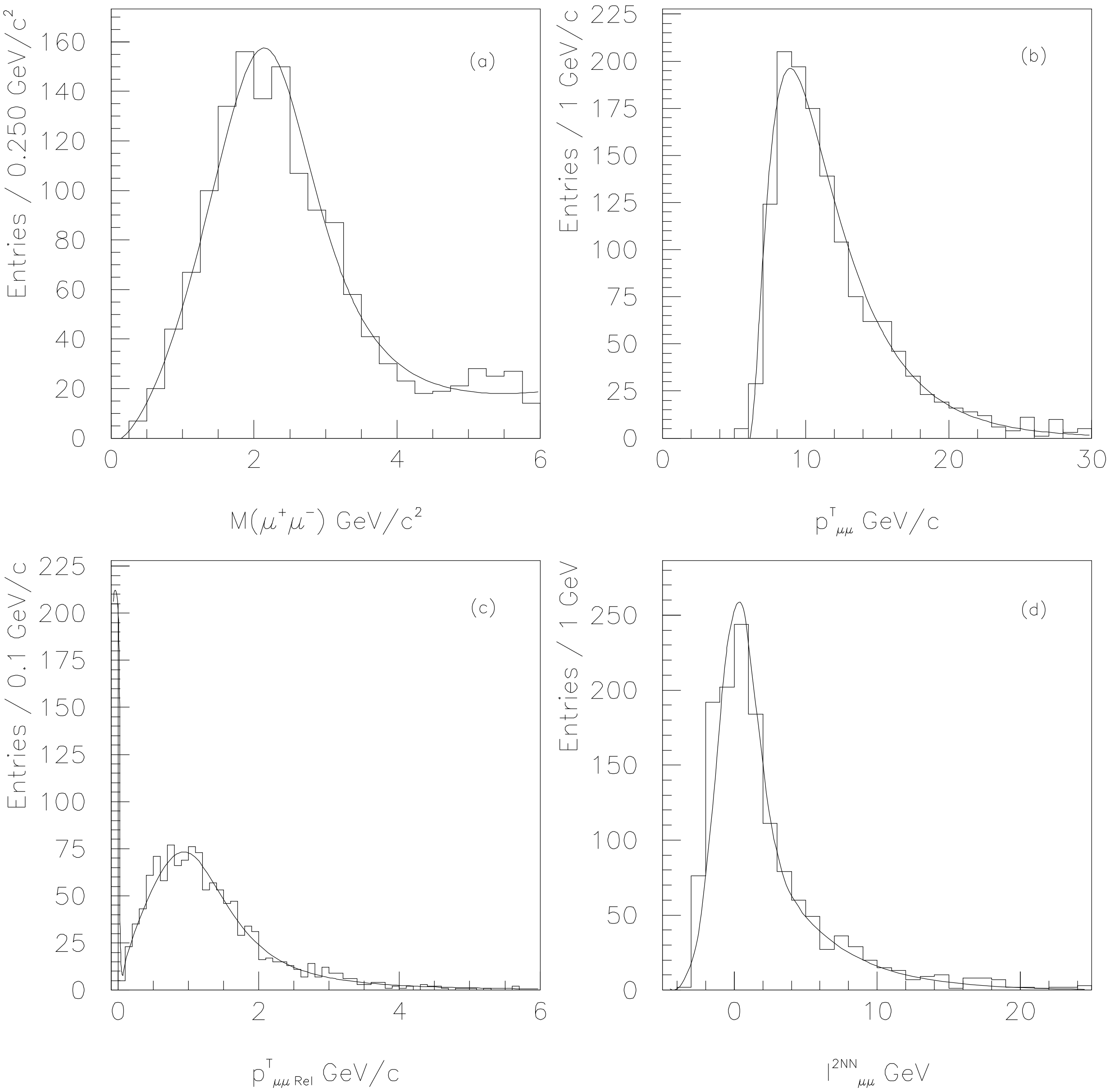


Figure 5.3: Distributions from $Q\bar{Q}$ Monte Carlo. (a) Invariant Mass (b) Dimuon $p_T$ (c) Dimuon $p_{TRel}$ and (d) Dimuon Isolation. Superimposed on the plots are parametrized fits.

broad mass distribution peaked near 9 $GeV/c^2$. NLO dimuon topology is somewhat analogous in characteristics to b-quark sequential decays. The dimuon $p_T$ has relatively larger values than the LO case, while the opening angles between the muons peaks near 20 degrees. The mass distribution for the NLO case exhibits a nearly exponential behaviour but with a turn on that peaks the distribution at a value somewhat less than 1 $GeV/c^2$.

In total we generated 20000 events in the Drell-Yan sample. Fig.5.4 shows distributions for the Drell-Yan Monte Carlo.

## 5.4 Low Mass Meson Resonances

Another source of dimuon production at hadron colliders stems from the production of numerous low mass meson resonances such as the $\rho, \omega, \phi, \eta$, and $\eta'$. Although the branching ratios to $\mu^+\mu^-$ final states are rather small (typically on the order $10^{-4}$), this is compensated by the fact that such mesons are produced in abundance as constituents of jets resulting from hadronization processes. Table 5.2 lists the various low mass resonant states simulated. Some of these are two body decays directly into $\mu^+\mu^-$ final states, whereas others are three body decays which also include $\mu^+\mu^-$ in the final state.

The package used to simulate these decays is based upon ISAJET but was modified [66] to include the muonic decays of these well known resonances. What is done is to replace the ISAJET primary charged hadron (pion,kaon,proton) with one of $\rho, \omega, \phi, \eta$, or $\eta'$. For the 3-body decays the dimuons that are generated come from the decay of a virtual photon. In all we have generated 10000 such events. Fig.5.5 shows distributions for the Low Mass Monte Carlo.

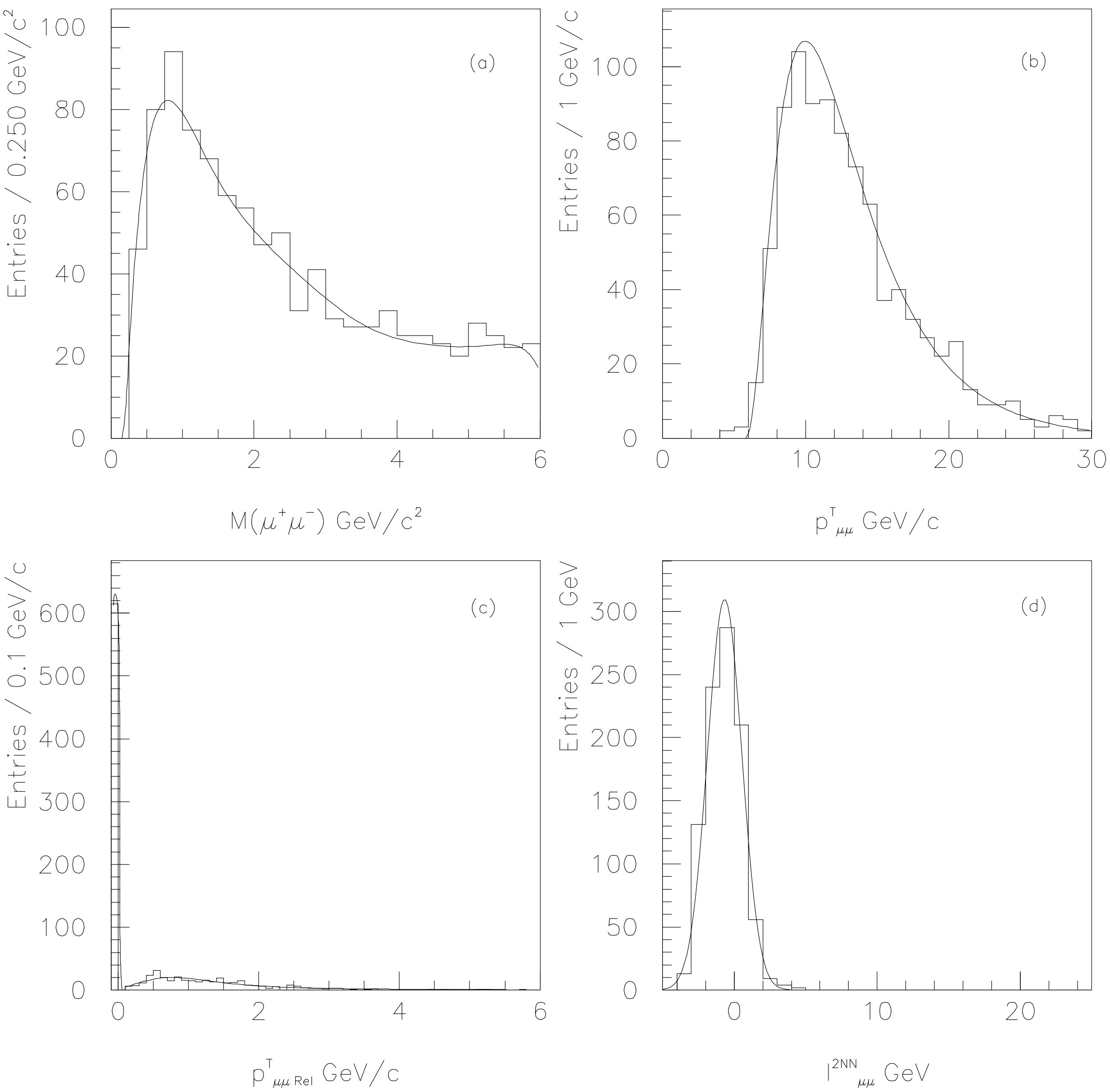


Figure 5.4: Distributions from Drell-Yan Monte Carlo. (a) Invariant Mass (b) Dimuon $p_T$ (c) Dimuon $p_{TRel}$ and (d) Dimuon Isolation. Superimposed on the plots are parametrized fits.

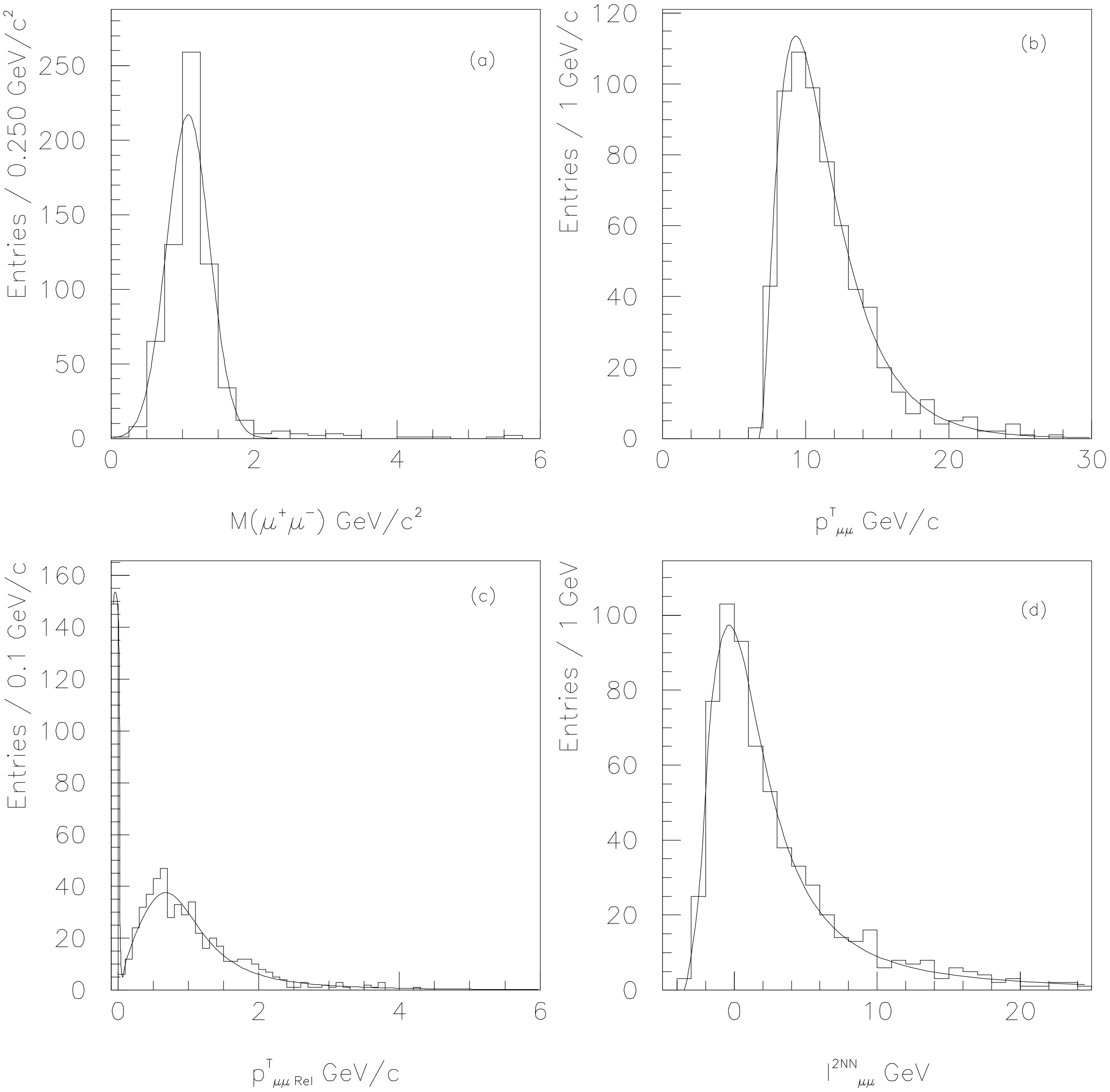


Figure 5.5: Distributions from Low Mass Resonances Monte Carlo. (a) Invariant Mass (b) Dimuon $p_T$ (c) Dimuon $p_{TRel}$ and (d) Dimuon Isolation. Superimposed on the plots are parametrized fits.

| Resonance | Mass(MeV) | Decay | Branching Ratio |
|---|---|---|---|
| $\rho$ | 769.9 | $\mu^+\mu^-$ | $4.6 \times 10^{-5}$ |
| $\omega$ | 781.94 | $\mu^+\mu^-$ | $1.8 \times 10^{-4}$ |
| $\phi$ | 1019.4 | $\mu^+\mu^-$ | $2.48 \times 10^{-4}$ |
| $\eta$ | 547.45 | $\mu^+\mu^-\gamma$ | $3.1 \times 10^{-4}$ |
| $\eta^{'}$ | 957.77 | $\mu^+\mu^-\gamma$ | $1.04 \times 10^{-4}$ |
| $\omega$ | 781.94 | $\mu^+\mu^-\pi^0$ | $1.2 \times 10^{-4}$ |

Table 5.2: Low mass resonances and their muonic decays simulated in ISAJET

## 5.5 Dimuons arising from $\pi - K$ decays.

A dimuon background may also be generated by the leptonic decays of $\pi$ and $K$ mesons, that is $\pi \to \mu + \nu_\mu$ ($Br = 99.99\%$), and $K \to \mu + \nu_\mu$ ($Br = 63.51\%$). The probability that the dimuon is constituted entirely of such decay muons is negligible when compared with the much greater chance of a prompt muon (say from heavy quark decay) combining with a $\pi$ or $K$ decay muon to form a dimuon. This so-called "prompt plus decay" mechanism provides a significant source of background in the study of dimuon physics processes.

This mechanism has been simulated in ISAJET by utilizing the heavy quark $Q\bar{Q}$ dimuon Monte Carlo discussed earlier. Essentially one of the muons is replaced by a $\pi$ or $K$ meson which is then allowed to undergo leptonic decay. We have generated 20000 such events. Fig.5.6 shows distributions for the $\pi - K$ Monte Carlo.

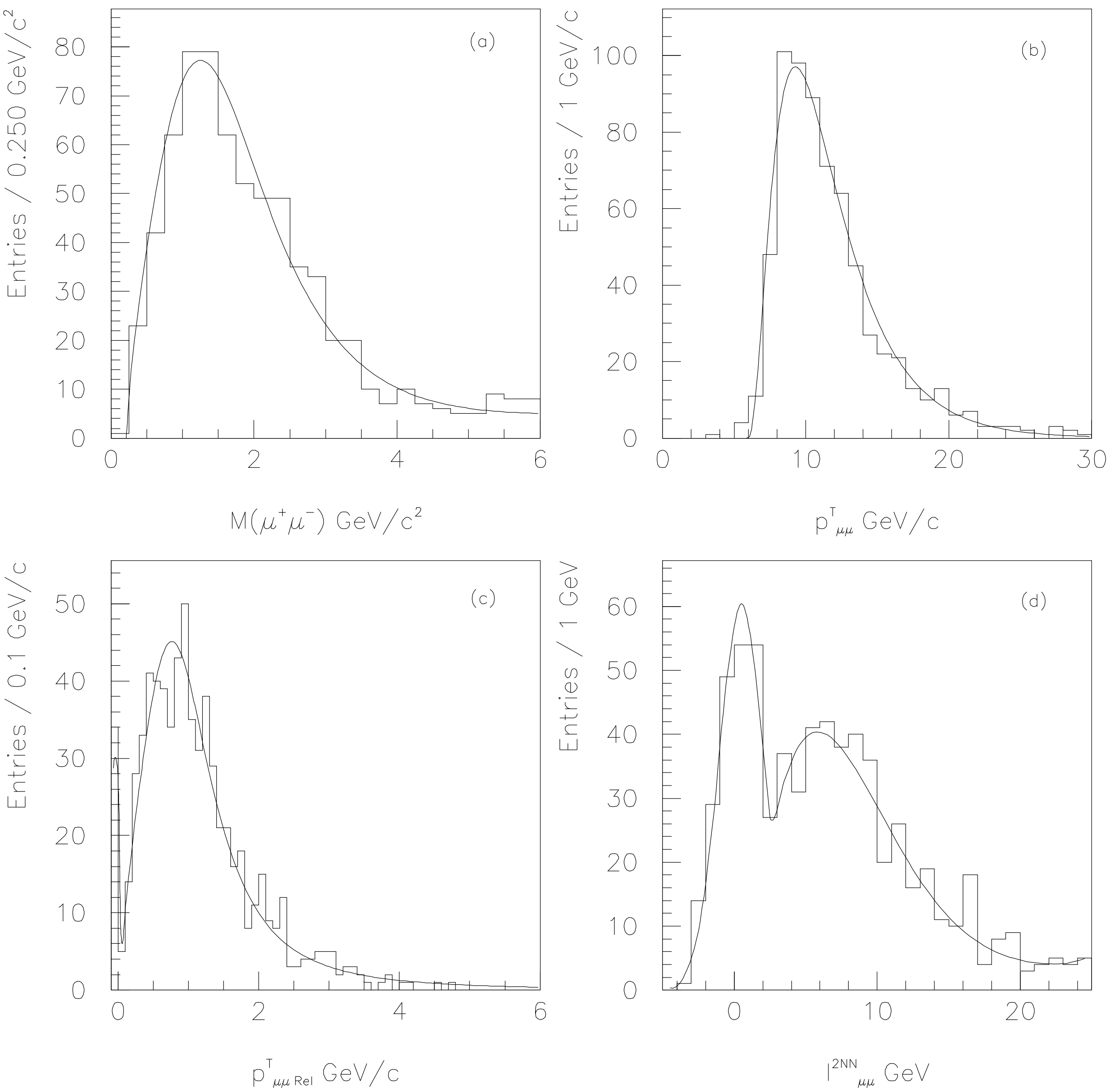


Figure 5.6: Distributions from $\pi - K$ Monte Carlo. (a) Invariant Mass (b) Dimuon $p_T$ (c) Dimuon $p_{TRel}$ and (d) Dimuon Isolation. Superimposed on the plots are parametrized fits.

# Chapter 6

# Determination of $J/\psi$ Acceptance and Detection Efficiency

In this chapter we discuss the methods used and the criteria employed in selecting $J/\psi$ events for further analysis. We also address the important problem of determining the efficiency and acceptance for observation of $J/\psi$ events based upon our event selection and trigger criteria.

## 6.1 Event Selection Cuts

Dimuons reconstructed from candidate muon tracks may in fact be fake dimuons that arise from wrongly identified muons, or they may be spurious dimuon candidates in that they arise from true muons which are wrongly associated with each other and so constitute a combinatorial background to signals of interest. In order to reduce as much as possible the background arising from fakes and combinatorics we apply a set of muon id selection criteria. We spend some time now to discuss the requirements used to define a good muon.

### 6.1.1 Muon ID Cuts

- **Muon Quality**. Each muon candidate has several quality flag indicators assigned to it by the muon reconstruction code. One such flag is called IFW4. This particular indicator serves to give a sense of the overall quality of the muon track candidate by summing other integral valued quality indicators that are set in order to flag candidates that have "bad" track characteristics for various reasons. Good muon candidates have an IFW4 value of 0. Such muons have reasonable vertex projection in both the bend and non-bend views, and also hit combinations that have allowed for good fits in both the bend and non-bend views. In general we require that muon candidates have IFW4 equal to zero or one.

- **A-Layer Requirement.** In order to reduce the possibility of picking up muons not associated with the primary event vertex, and to insure a good momentum determination of the muon track candidate, we have required that all muon candidates have A-layer hits along the track. This means that muons are required to have either 3 layer tracks A-B-C, or else 2 layer tracks that contain the A layer, that is A-B or A-C tracks.

- **Calorimeter MIP Requirement.** The muon reconstruction code asigns a series of words to muon candidates that represent the energy depositions observed in the calorimeter within the immediate vicinity of the reconstructed muon track. One such word is $E_{Cal}^{2NN}$ which sums the energy deposited in the calorimeter cells traversed by the muon as well the 2 nearest neighboring cells. A minimum ionizing particle (MIP) such as a muon is expected to have a value of $E_{Cal}^{2NN}$ on the order of 1 GeV. We therefore require that all muon candidates have $E_{Cal}^{2NN} \geq 1GeV$.

- **Magnetic Field Thickness.** Upon traversing the iron toroid between the A layer and the B-C layers of the muon system, a muon will suffer a transverse momentum kick in the bend view due to the presence of the magnetic field. It is this change in direction that allows one to infer the value of the muon momentum. This change in direction or bend is proportional to the integral of the magnetic field induction vector $B$ along the path of the muon. The reconstruction code calculates this integral $\int B \cdot dl$ and records its value in one of several Zebra bank structures associated with muons. In order to insure a good momentum determination for the muon we require that all candidates have $\int B \cdot dl \geq 0.5$ GeV.

- **CD Match.** Upon passing through the Central Detector system a good muon candidate will leave an ionizing trail within the CD that can be well matched to the track reconstructed in the muon system. The muon reconstruction code examines reconstructed CD tracks within a cone along the direction of the muon track and records whether or not a good matching CD track has been found ($\Delta\theta \leq 0.45$ radians and $\Delta\phi \leq 0.45$ radians). We require that all muon candidates have a matching CD track.

- **Muon Kinematic Cuts.** It has been determined that a muon requires a $p_T$ of approximately 3 $GeV/c$ in order to pass through the magnetic toroid in the central muon region. As we will show in the next chapter, $J/\psi$'s are not well observed outside the central region of the muon detector. We therefore require that a good muon candidate satisfy the following kinematic cut: $p_T^{\mu} > 3$ GeV/c and $|\eta_\mu| < 1$. Data distributions of the azimuthal angle of muons show a pronounced dip in the region $80^\circ \leq \varphi_\mu \leq 110^\circ$ . This is the region of the muon system near the main ring beam pipe. In this area the efficiency of the muon chambers is quite poor due to voltage sagging induced by main ring beam and halo effects. Since the efficiencies are not well understood here, we exclude whatever small number of muons appear to occupy this azimuthal region. Hence good muons are required to satisfy $\varphi_\mu \leq 80^\circ$ *or* $\varphi_\mu \geq 110^\circ$.

The above set of selection criteria constitute the minimal requirements used to identify good muons among all reconstructed muon track candidates. Since we are interested in studying dimuons we shall also institute a basic set of dimuon selection cuts with are further tailored to supress combinatoric and cosmic background. We now briefly discuss these dimuon requirements.

### 6.1.2 Dimuon Selection Cuts

- **Two Good Muons.** Each muon that constitutes the dimuon pair is required to satisfy the above listed set of muon id requirements.

- **Cosmic Ray Rejection.** In order to suppress the background due to cosmic rays, we require that the muons which constitute the dimuon candidate shall not be back-to-back. Essentially all true cosmic ray events exhibit this back-to-back topology as they pass through the muon system. In order to reject such cosmic rays we require the following tight cosmic cut: $\Delta\varphi_{\mu\mu} \leq 150^\circ$ *or* $(\theta_{\mu_1} + \theta_{\mu_2}) - 180^\circ \geq 30^\circ$.

- **Dimuon Kinematic Cut.** The next chapter will show that $J/\psi$ candidate events are not well observed outside the central region of the muon detector. In order to stay away from the tails of the observed pseudo- rapidity distribution and in order to have a sharp and well defined cut we require that good dimuon candidates shall have $|\eta_{\mu\mu}| \leq 0.6$.

## 6.2 Data Selection and Processing

### The Dimuon B2M Stream

The data sample that was analyzed derives from the so-called B2M stream. This subset of ALL STREAM data required that the following conditions be satisfied:

- **Dimuon Requirement.** The event should contain at least 2 reconstructed muons.

- **Muon Quality Requirement.** The sum of the quality flags for both muons should be less than or equal to 2.

- **Calorimeter Requirement.** Each muon was required to have a calorimeter energy deposition consistent with that expected for a minimum ionizing particle. In particular the energy summed along the cells traversed by the muon as well as the 2 nearest neighboring cells should be greater than 1 GeV.

- **Cosmic Ray Rejection Requirement.** Each muon pair was required to have a 3-d opening angle less than $160^\circ$. If the opening angle was greater than $160^\circ$, then at least one of the muons of the pair should have a floating T0 less than 100 ns.

Approximately 6% of ALL STREAM events satisfied these requirements. Further, for the inclusive cross section only B2M events corresponding to post shut-

| | All Triggers | MU-2-HIGH |
|---|---|---|
| Post Shutdown | 7.67 $pb^{-1}$ | 6.62 $pb^{-1}$ |
| Pre Shutdown | 5.64 $pb^{-1}$ | 4.80 $pb^{-1}$ |

Table 6.1: Luminosities observed at the DØ detector for the 1992 – 1993 collider run. The relative error on these numbers is 12%.

down data were analyzed since important hardware changes in the L1 muon trigger logic just prior to the beginning of the post shutdown run significantly affected the dimuon triggers. The runs included were those in the range 60832 to 65429. After removal of bad runs, the data, processed with version 11.17-11.19 of the reconstruction code, and corrected for pre-scaling of the MU-2-HIGH trigger, corresponded to an integrated luminosity of $\int \pounds dt = 6.62\ pb^{-1}$. Table 6.1 summarizes the observed luminosities.

**Dimuon Sub-Filter**

More restrictive selection criteria were imposed by running a subfilter on the B2M stream events. This subfilter imposed the following requirements on each muon of the pair that constituted a candidate dimuon:

- The event should contain at least 2 reconstructed muons.
- Each muon of the pair should have $|\eta_\mu| \leq 1.7$
- The sum of the quality flags for both muons in the pair should be $< 2$
- Each muon in the pair should have $E_{Cal}^{2NN} \geq 1\ GeV$
- Each pair of muons for the candidate dimuon should have $\Delta\varphi_{\mu\mu} \leq 160°$ or $(\theta_{\mu_1} + \theta_{\mu_2}) - 180° \geq 20°$

- Each pair of muons for the dimuon candidate should have $M_{\mu\mu} \leq 200\ GeV/c^2$

The number of events passed by the subfilter was 253285, representing approximately 4.8% of ALL STREAM post shutdown data.

## 6.3 $J/\psi$ Acceptance and Detection Efficiency

### 6.3.1 The Detection Efficiency for $J/\psi$ Mesons

We discuss first the efficiencies for our muon id requirements. These are various additional cuts applied to the output of our dimuon sub-filter as discussed above. The general intent of these cuts is to provide a dimuon data sample that is free from spurious or fake muon contamination.

#### Offline Muon ID Requirements

In order to insure that candidate muons correspond to good muons, the cuts described in Table 6.2 were made. Wherever possible we have checked the efficiencies of these cuts on a data sample of "virgin" ALL-SREAM events. These latter events have not been run through either the B2M dimuon stream or the Dimuon Sub-Filter discussed above. The only requirements made were that the event should contain at least two reconstructed muon candidates. Therefore these events should not be biased in any way with regards to the application of offline cuts. The reconstruction code used was V11.17-11.19. The integrated luminosity of these ALL-STREAM events is approximately 1.5 $pb^{-1}$. No trigger requirement has been imposed.

In the analysis that follows we have imposed a set of **muon kinematic cuts**:

- muon $p_T$ cut: $p_T^\mu\ > 3\ \ \mathrm{GeV/c}$
- muon $\eta$ cut: $|\eta_\mu| < 1$
- fiducial muon $\varphi$ cut: $\varphi_\mu < 80^\circ$ *or* $\varphi_\mu > 110^\circ$

The muon $\varphi$ cut excludes a poorly understood region of the muon system which has been significantly aged by main ring halo effects. These muon kinematic cuts further select the central or CF region of WAMUS where muon efficiencies and chamber performance are best understood.

As regards the other muon offline cuts, Fig.6.1 shows the dimuon mass spectrum for opposite sign muons before the application of any cuts whatsoever. The spectrum shows the overwhelming predominance of cosmic ray contamination. The next lower plot results from the application of the fiducial muon $\varphi$ and muon kinematic cuts. The next lower plot shows what results from the application of the muon quality flag cut requiring the sum of the IFW4 words for both muons to be less than or equal to 1, that is only 0-0 and 1-0 combinations are allowed. The next lower plot shows the result of applying the cosmic cut which requires that the muons not be back-to-back, that is $\Delta\varphi_{\mu\mu} \leq 150^\circ$ *or* $(\theta_{\mu_1} + \theta_{\mu_2}) - 180^\circ \geq 30^\circ$. There is, as yet, no clear evidence for a $J/\psi$ signal.

Fig.6.2 shows the dimuon mass spectrum where we left off in Fig.6.1. At this point we have required opposite sign muon pairs with the muon kinematic, muon quality flag, and cosmic cuts appplied. The next lower plot shows the result of applying the CD match requirement, namely both muons are required to have a matching CD track within a cone about the muon direction. It is here that we have the first evidence of a possible $J/\psi$ signal in the mass range $2-4.4\ GeV/c^2$.

Fig.6.3 again picks up where Fig.6.2 left off, the upper plot showing the status after the imposition of the CD match requirement. The next lower plot shows the result of aplying the muon MIP requirement, namely each muon should have $E_{Cal}^{2NN} \geq 1 GeV$. The next lower plot results when the muon BDL requirement is imposed. This requires that $\int B \cdot dl \geq 0.5$ GeV for each muon. The lowest plot shows what results when we impose the A-Layer requirement on each muon. This means that the muons are required to have either 3 layer tracks A-B-C, or else 2 layer tracks that contain the A layer, that is A-B or A-C tracks.

Fig.6.4 shows the dimuon $\eta$ distribution for the lowest plot in Fig.6.3 which has essentially all cuts applied with the exception of the fiducial $\varphi$ cuts on the muons and the dimuon kinematic cut of $|\eta_{\mu\mu}| < 0.6$. The bottom plot on Fig.6.4 shows the $\eta$ distribution for only those events in the nominal $J/\psi$ mass range $2 - 4.4\ GeV/c^2$. Essentially no $J/\psi$'s are observed beyond $|\eta_{\mu\mu}| = 0.9$. In order to stay away from the tails of the distribution and to have a sharp kinematic cut, we require that $|\eta_{\mu\mu}| < 0.6$.

We have estimated the efficiency of these cuts by selecting a sample of good muons. This sample was derived by applying the cuts listed in Table 6.2 along with the dimuon kinematic cut $|\eta_{\mu\mu}| < 0.6$ and the MU-2-HIGH trigger to the ALL-STREAM data. Fig.6.5 shows the resulting dimuon distributions. For a given offline cut we began with this sample and relaxed the cut under study. By counting the number of entries that came back in under the $J/\psi$ peak ($2 - 4.4\ GeV/c^2$) we were able to estimate the inefficiency (and therefore the efficiency) of this particular cut. We did this for each of the cuts in turn listed in Table 6.2. Fig.6.6 shows the dimuon mass distributions that were used. This same procedure was carried out on the $J/\psi$ Monte Carlo events. Consistent results were obtained. Fig.6.7 shows some of the distributions that result when the given cut is relaxed

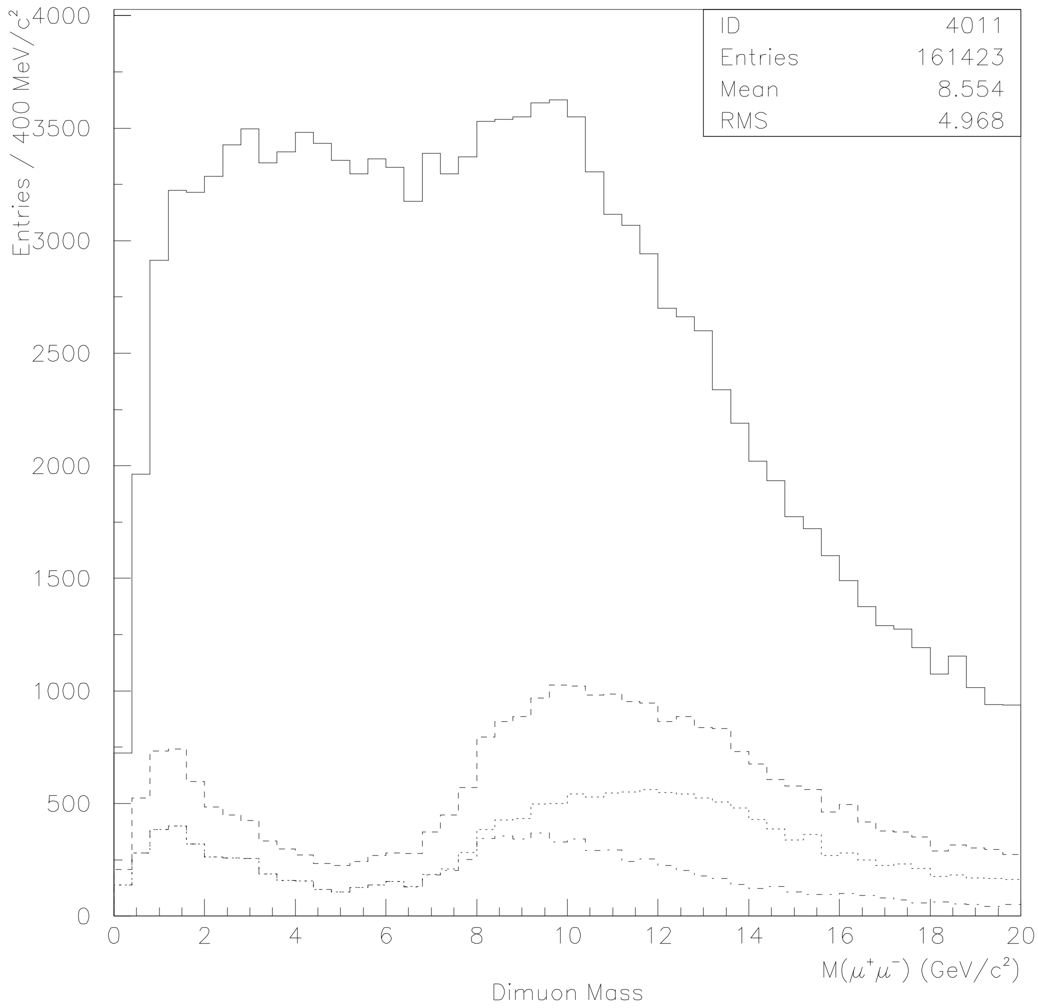


Figure 6.1: Dimuon mass spectrum showing sequence of offline cuts (None,Muon Kinematic,Muon Quality,Cosmic) applied to ALL-STREAM sample

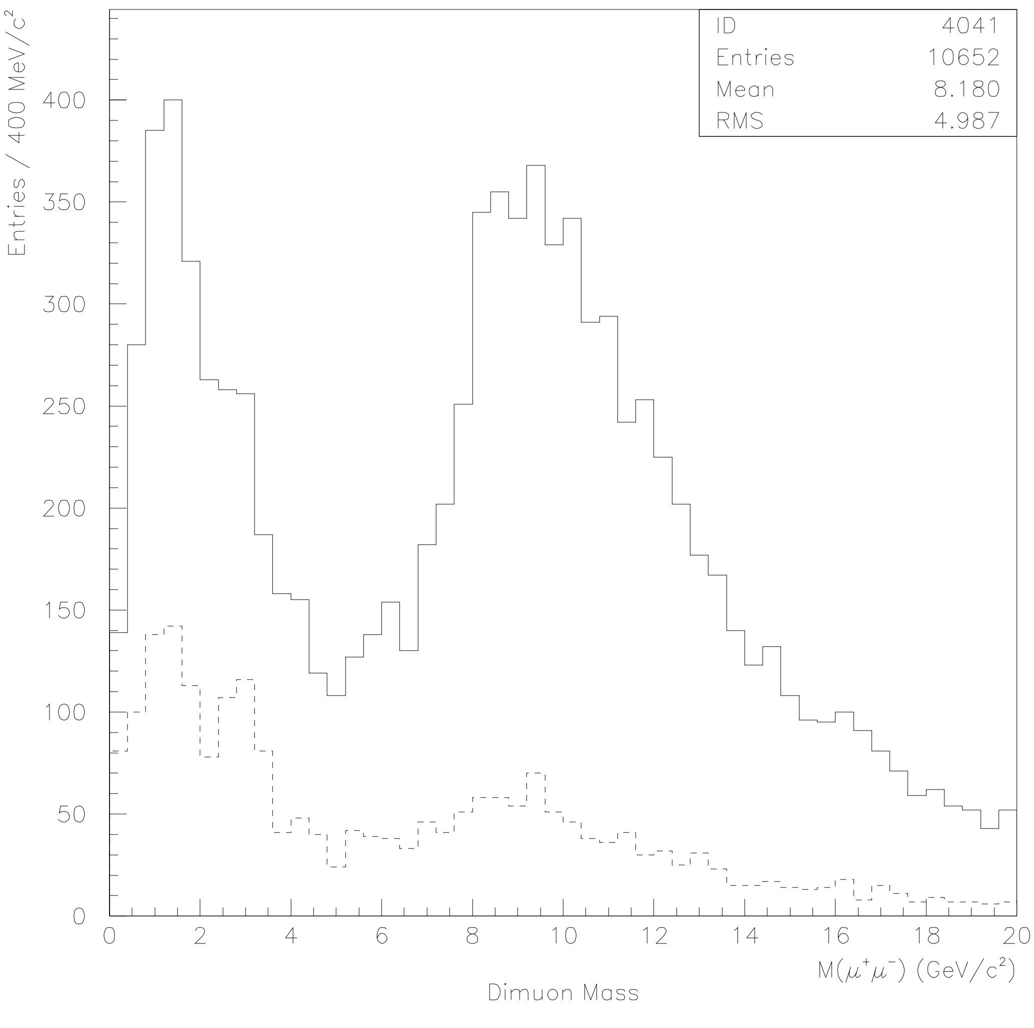


Figure 6.2: Dimuon mass spectrum showing sequence of offline cuts: (top) Muon Kinematic-Muon Quality-Cosmic, (bottom) above plus CD match

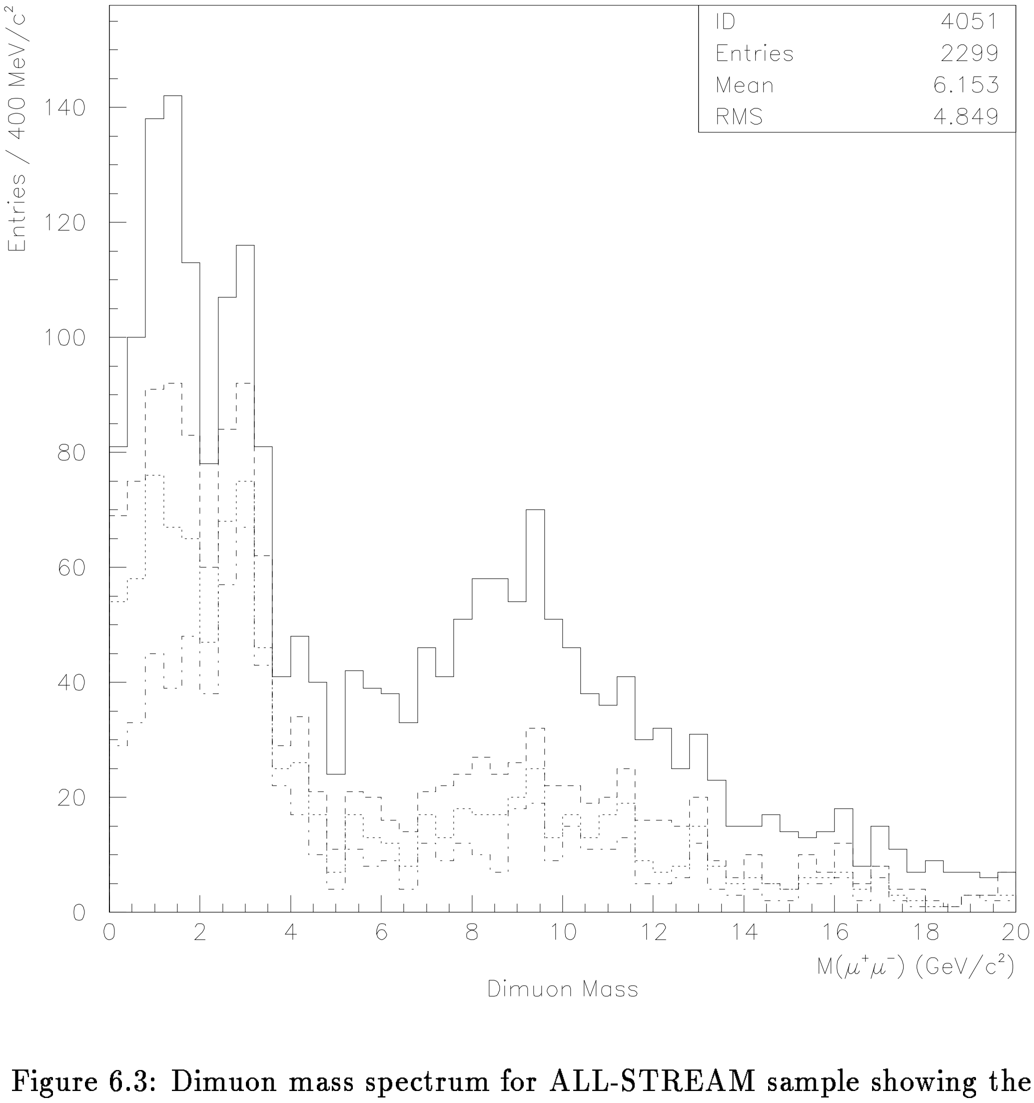


Figure 6.3: Dimuon mass spectrum for ALL-STREAM sample showing the effect of a sequence of offline cuts (Muon Kinematic-Muon Quality-Cosmic-CD),(above plus MIP),(above plus BDL),(above plus A-Layer)

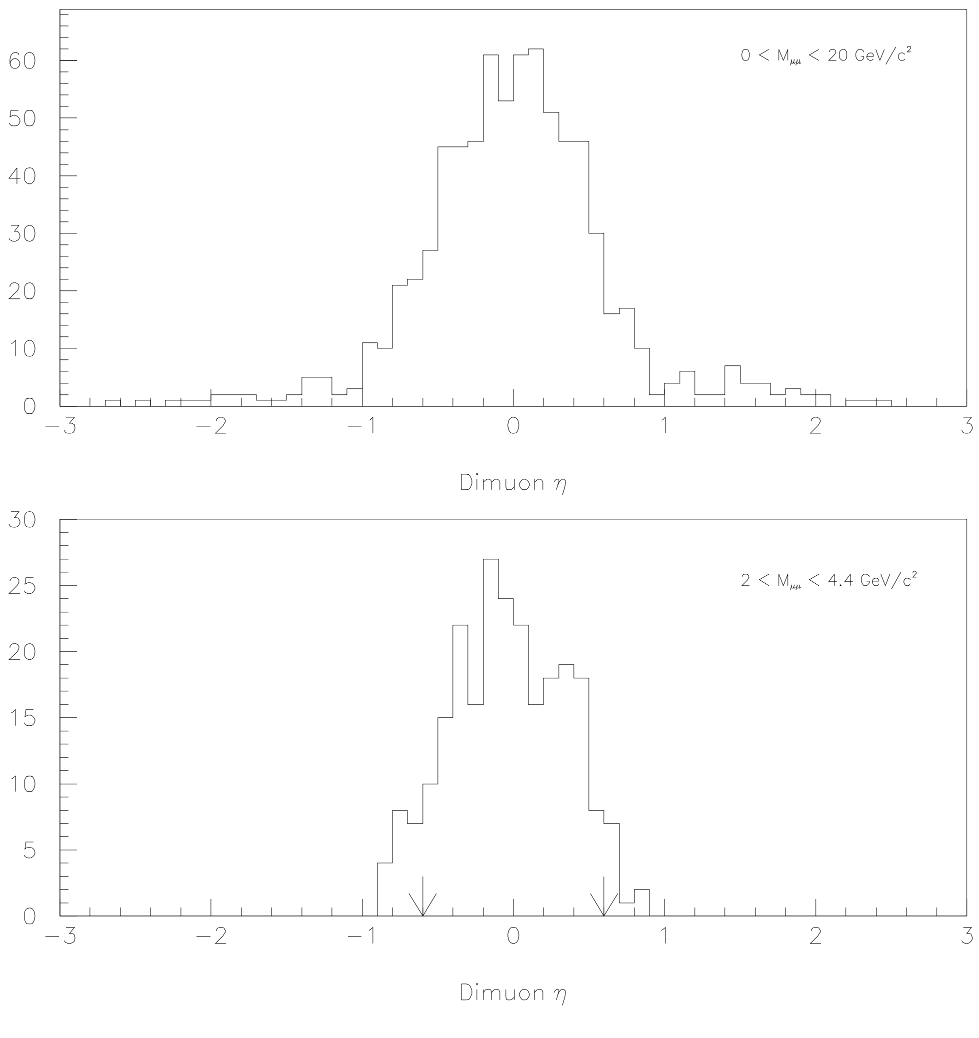


Figure 6.4: ALL-STREAM sample Dimuon $\eta$ distributions: upper ($0 < M_{\mu\mu} < 20\ GeV/c^2$) and lower ($2 < M_{\mu\mu} < 4.4\ GeV/c^2$)

while the others remain in place.

### Dimuon Requirements

Candidate dimuon events were selected by requiring:

1. At least two good muons
2. Dimuon Kinematic Cut: $|\eta_{\mu\mu}| \leq 0.6$

### Trigger Requirements

Events were required to pass the Level 1 and Level 2 MU-2-HIGH trigger. The general requirements of MU-2-HIGH are the following:

- Level 1 - two muons with $|\eta_{\mu}| < 1.7$
- Level 2 - two muons with $p_T^{\mu} > 3$ GeV/c and $|\eta_{\mu}| < 1.7$

### Efficiency for $J/\psi$ Selection

Efficiencies for $J/\psi$ selection were determined by running $J/\psi$ ISAJET Monte Carlo events through a complete simulation of the detector and Level-1 and Level-2 Triggers. Chamber Efficiencies were accounted for by employing the MU-SMEAR package, and Calorimeter Noise was simulated by using the NOISY package. $J/\psi$ selection proceeded as in the dimuon selection process described above, except that the muons were required to be of opposite sign and to give an invariant mass in the nominal $J/\psi$ mass region, namely 2.0 to 4.4 $GeV/c^2$. Table 6.3 summarizes the various cut efficiencies employed, while Fig.6.8 shows a comparison of individual cut efficiencies calculated in Monte Carlo ( the dotted line) and calculated using ALL-STREAM data (the solid line) as discussed earlier. The agreement between Monte Carlo and data is is good with the exception of the CD match. We

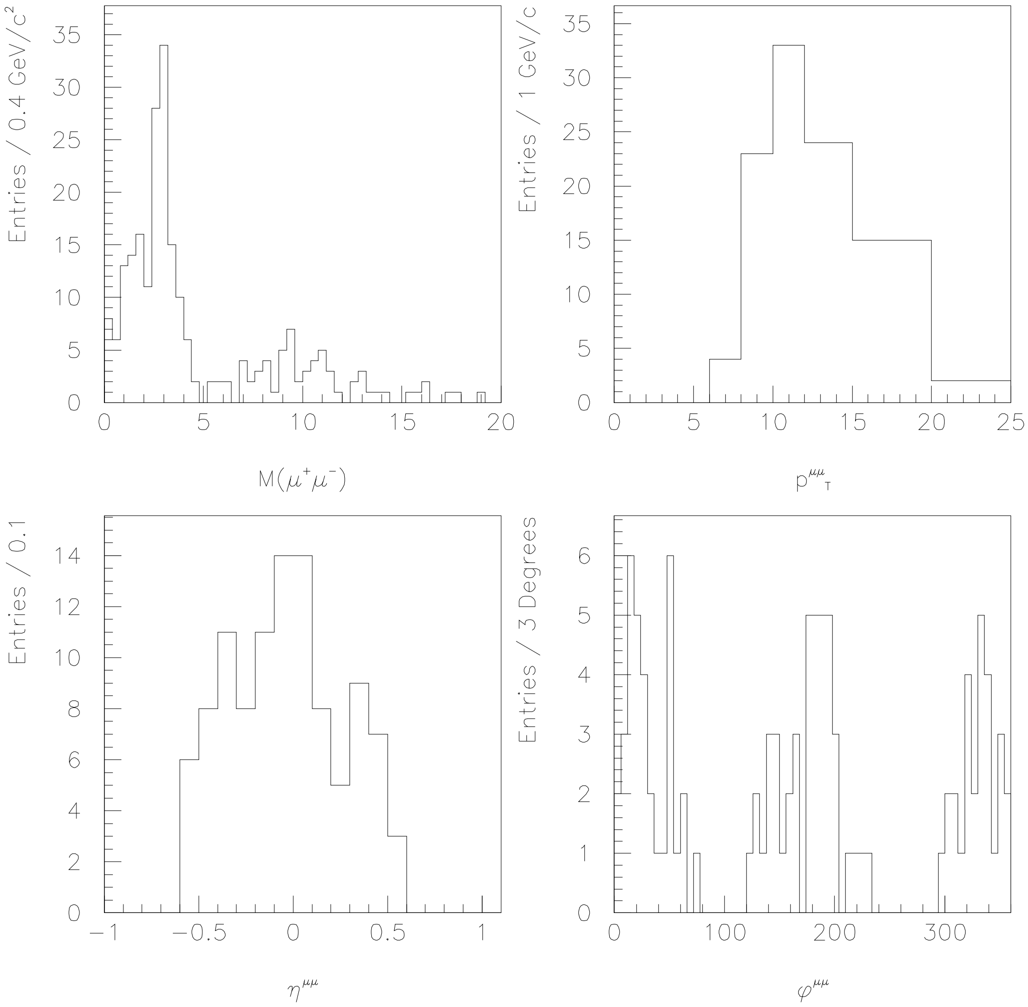


Figure 6.5: Dimuon distributions for ALL-STREAM sample with all offline cuts in place. This sample is used to estimate the efficiencies of our offline cuts.

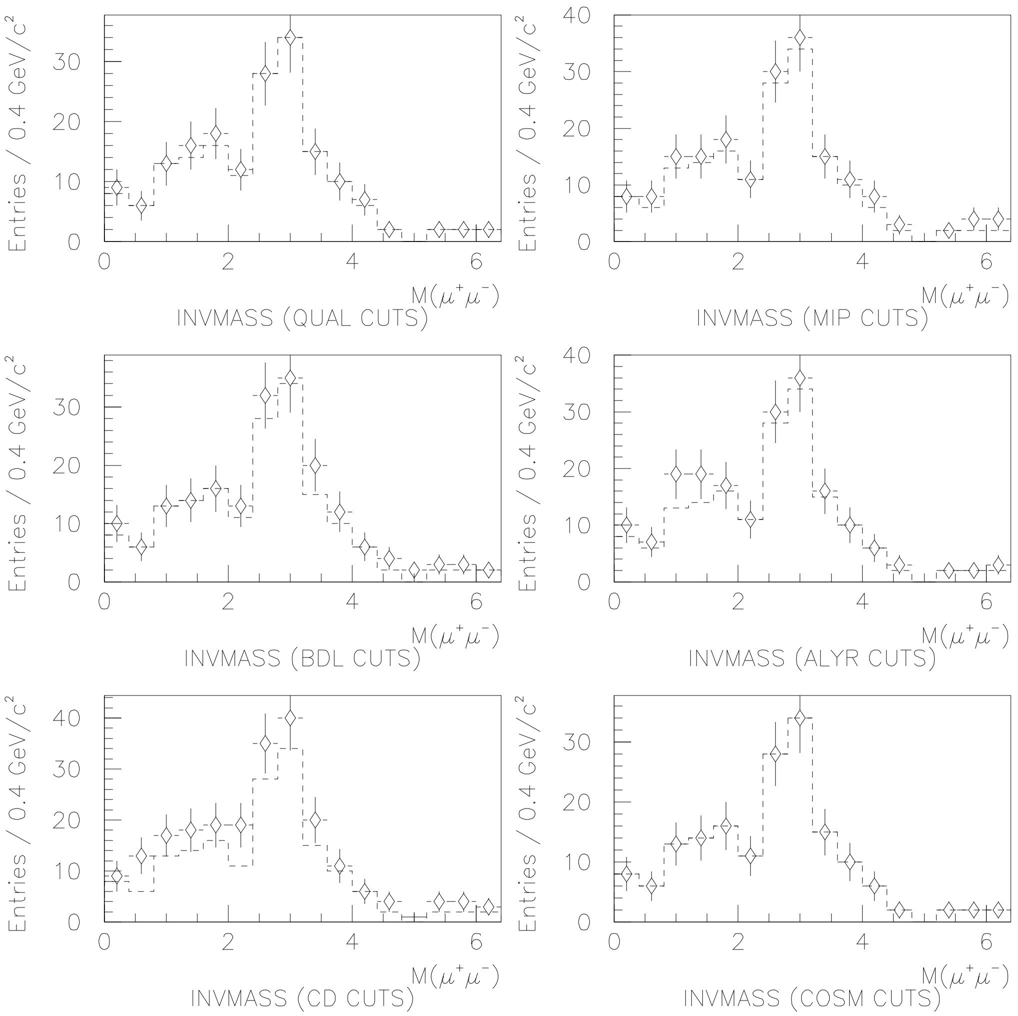


Figure 6.6: Dimuon mass distributions for ALL-STREAM sample used to estimate the efficiencies of our offline cuts. The dotted curve is for all cuts in place. The curve reperesented by the data symbols shows what results when the given cut is relaxed.

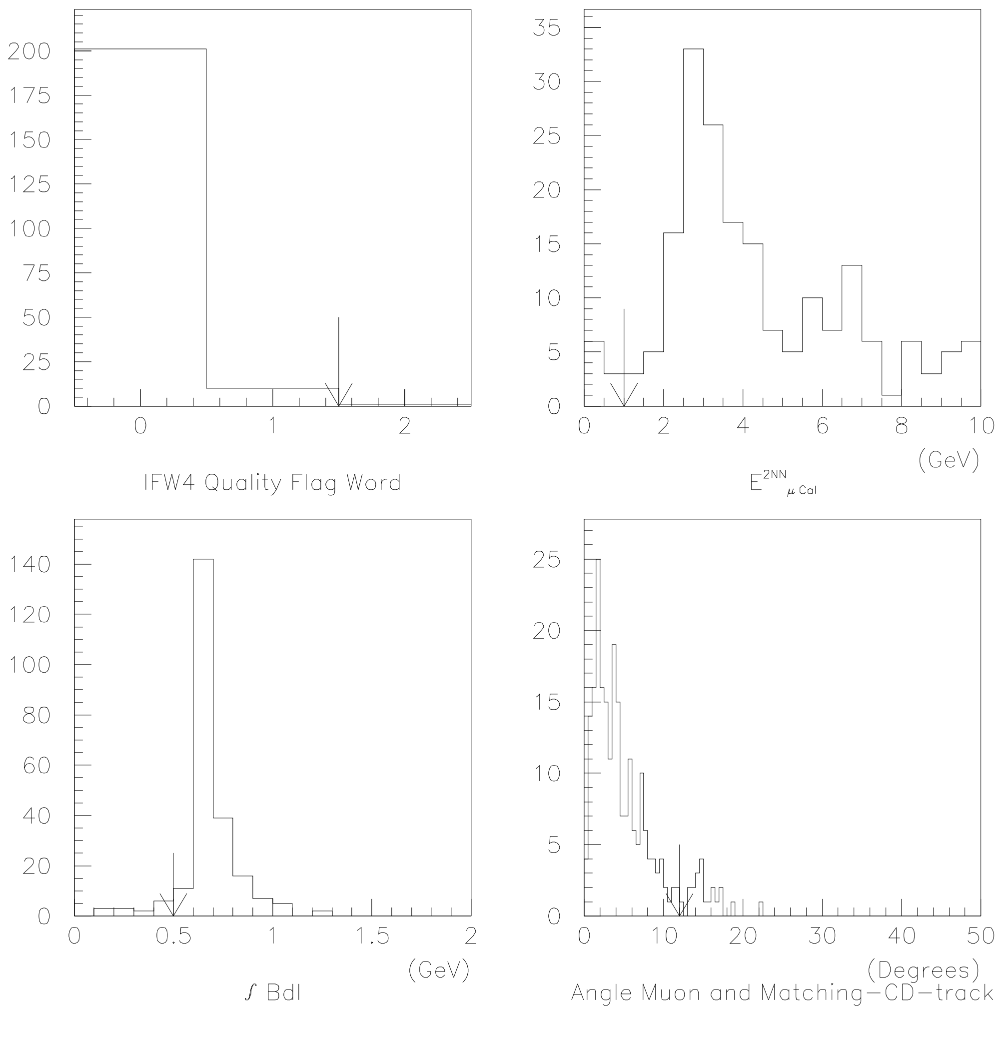


Figure 6.7: Selected offline cut distributions for ALL-STREAM sample (arrows indicate placement of the cut)

| | |
|---|---|
| Muon Quality Flag IFW4 | IFW4$\leq 1$ |
| A-Layer Requirement | IFW1 $\neq$ 1,4,11,14 |
| Muon MIP Deposition | $E_{Cal}^{2NN} \geq 1\ GeV$ |
| Magnetic Field Thickness | $\int B \cdot dl \geq 0.5$ GeV |
| Muon-CD track match | CD cone search $> 0$ |
| Tight Cosmic Cut | $\Delta\varphi_{\mu\mu} \leq 150°$ *or* $(\theta_{\mu_1} + \theta_{\mu_2}) - 180° \geq 30°$ |
| Muon Kinematic cut | $p_T^{\mu} > 3\ GeV/c$ and $\lvert\eta_\mu\rvert < 1$ and $\varphi_\mu \leq 80°$ *or* $\varphi_\mu \geq 110°$ |

Table 6.2: Requirements used to define a Good Muon

| Muon-Dimuon Cuts | Cut Specification | Efficiency/Dimuon (%) |
|---|---|---|
| Muon Quality Flag IFW4 | IFW4$\leq 1$ | $97 \pm 2$ |
| A-Layer Requirement | IFW1 $\neq$ 1,4,11,14 | $95 \pm 2$ |
| Muon MIP Deposition | $E_{Cal}^{2NN} \geq 1\ GeV$ | $95 \pm 1$ |
| Magnetic Field Thickness | $\int B \cdot dl \geq 0.5$ GeV | $91 \pm 3$ |
| Muon-CD track match | CD cone search $> 0$ | $79 \pm 3$ |
| Tight Cosmic Cut | $\Delta\varphi_{\mu\mu} \leq 150°$ or $(\theta_{\mu_1} + \theta_{\mu_2}) - 180° \geq 30°$ | $99 \pm 1$ |

Table 6.3: Efficiency per Dimuon due to Muon and Dimuon Cuts

have introduced into the Monte Carlo a residual efficiency factor of 90% in order to scale down the Monte Carlo estimate of CD match efficiency and bring it into closer agreement with what is observed in the data. If we refer to the above cuts as the BASE-CUTS, then the overall efficiency of these BASE-CUTS is $73 \pm 5$ %. Because of correlations between the various cuts, the overall BASE-CUT efficiency is not simply the product of the individual efficiencies.

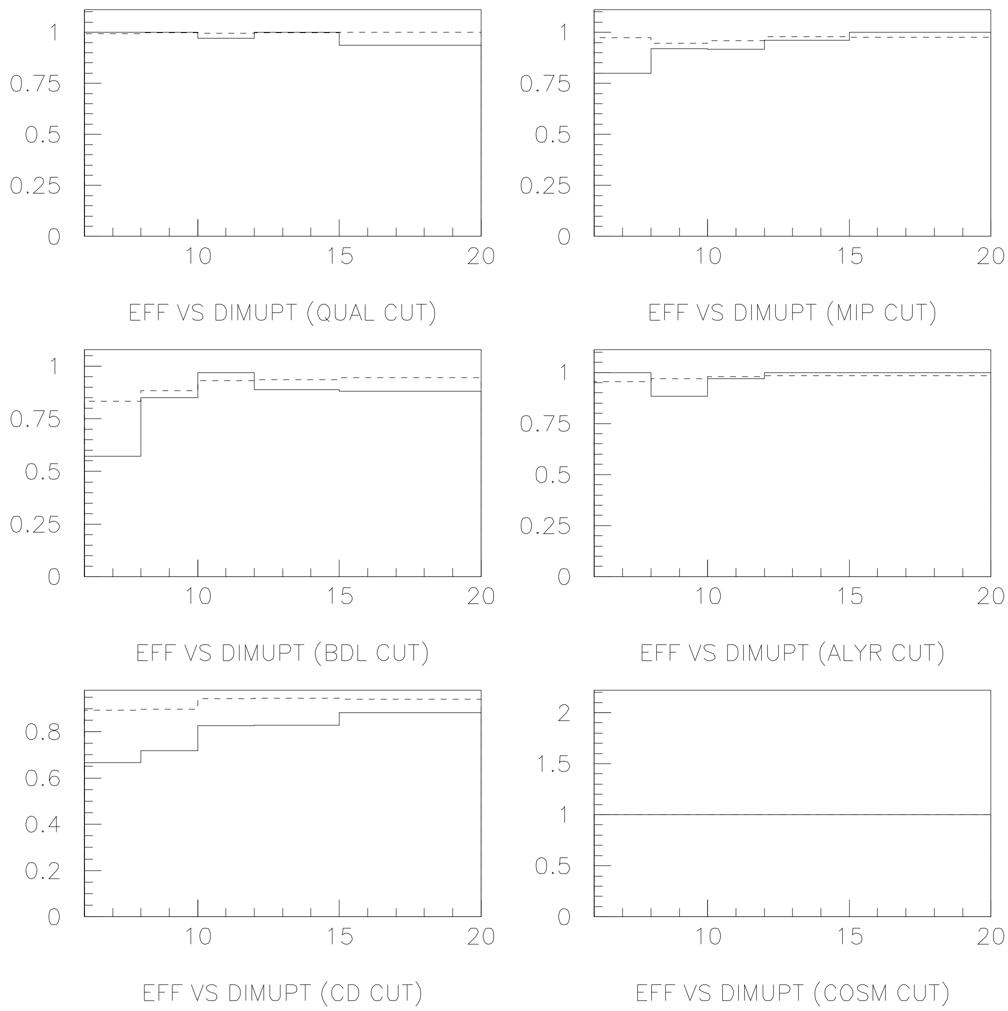


Figure 6.8: Various Offline Cut Efficiencies as a function of Dimuon $p_T$. The solid line is from the ALL-STREAM data sample, whereas the dotted line is from Monte Carlo.

### Trigger Efficiency

Events were analyzed offline under the MU-2-HIGH trigger. The general requirements of MU-2-HIGH are the following:

- Level 1 - two muons with $|\eta_\mu| < 1.7$
- Level 2 - two muons with $p_T^\mu > 3$ GeV/c and $|\eta_\mu| < 1.7$

We have estimated the trigger efficiency by using the $J/\psi$ ISAJET Monte Carlo. Fig.6.9 shows the $J/\psi$ trigger efficiency as a function of $J/\psi$ $p_T$. After accounting for pre-scaling, the total integrated luminosity under the MU-2-HIGH trigger was $\int \mathcal{L}\ dt = 6.6\ pb^{-1}$. Under the MU-2-HIGH trigger, we observed 1739 opposite sign dimuons and 623 same sign dimuons after imposing the above requirements. The dimuon mass spectrum is shown in Fig.6.10.

## 6.3.2 The Acceptance for $J/\psi$ Mesons

In this section we discuss the methods employed in determining the $J/\psi$ acceptance at the DØ detector. Naturally the acceptance is entirely dependent upon the corresponding muon acceptance. We must therefore carefully discuss the kinematic cuts made on the muons, why those cuts were made, and how they translate into the acceptance for $J/\psi$'s.

### Muon Kinematic Cuts

In order to simulate the acceptance for $J/\psi$'s at the DØ detector the $J/\psi$ ISAJET Monte Carlo samples were run through DOGEANT (version 3.14 of GEANT), then run through DORECO (version 11.19), and finally run through L12SIM ( global configuration file V7.2).

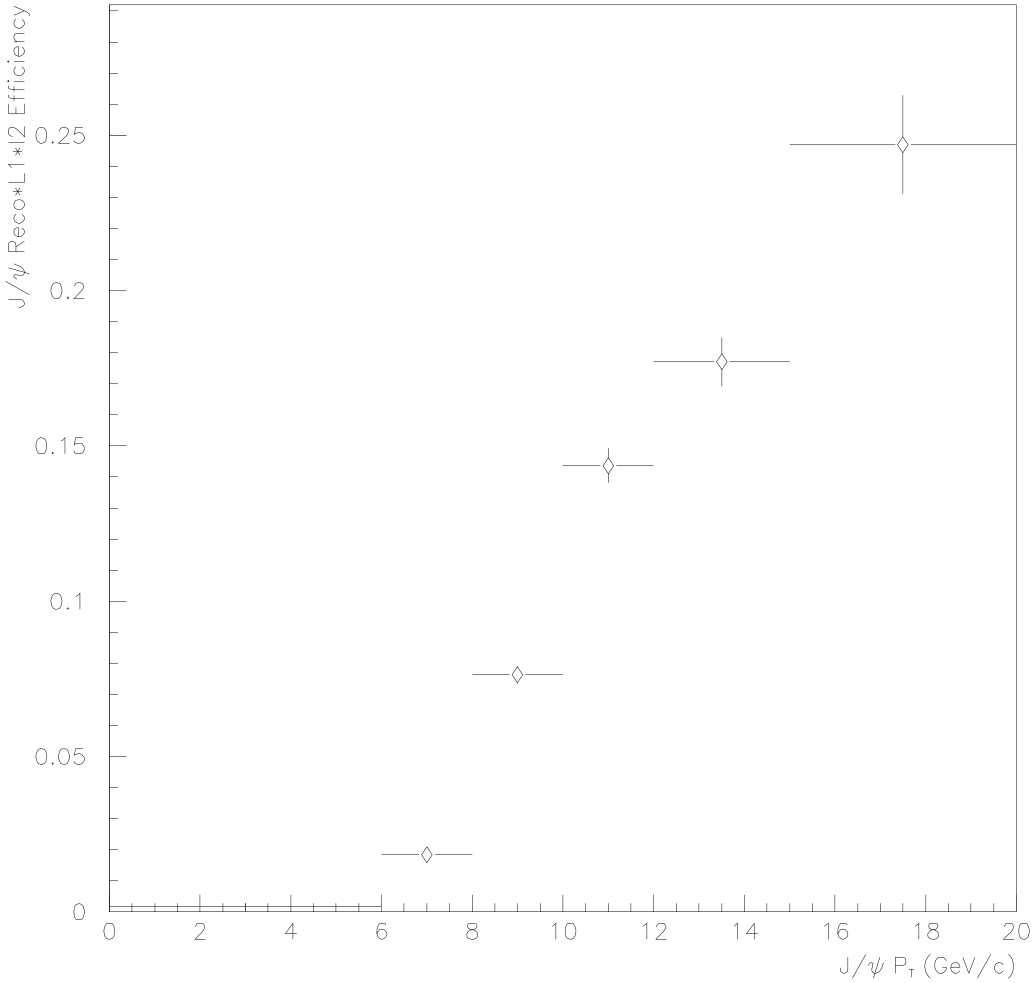


Figure 6.9: Combined Level 1-Level 2 Trigger Efficiency vs $J/\psi$ $p_T$

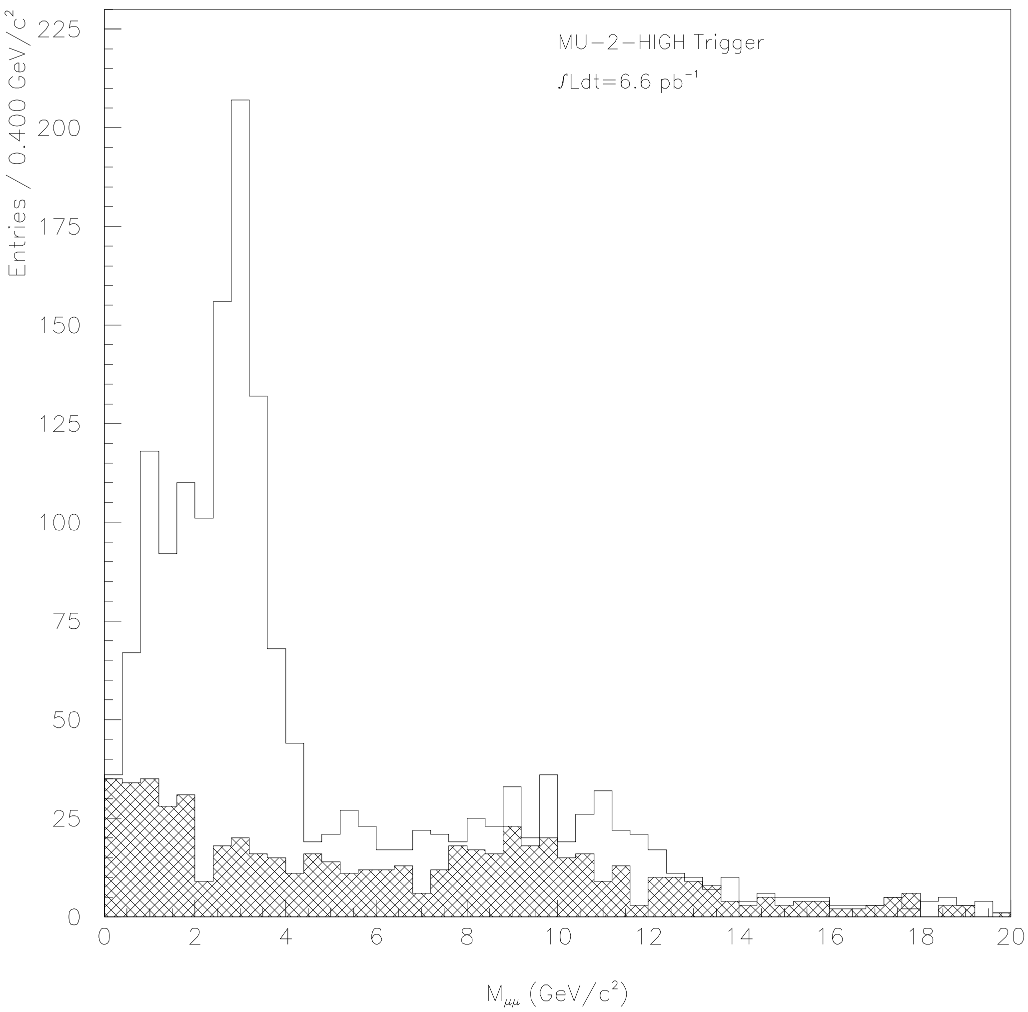


**Figure 6.10:** Dimuon Invariant Mass spectrum for opposite sign and same sign (shaded) muons

Since the efficiencies are not yet well understood for muons in the EF and beyond ($|\eta| > 1$), and since further the data do not seem to indicate any $J/\psi$ signal beyond $|\eta| = 0.9$, the muons in the Monte Carlo samples were required to be in the CF region ($|\eta| < 1$). Because of the detector thickness, muons in the CF region will range out unless their $p_T$ is greater than about 3 $GeV/c$. Therefore, in order to avoid high inefficiencies in GEANT, the following kinematic cuts were made on the muons that were produced in the ISAJET Monte Carlo samples discussed above:

$$p_T^{\mu} > 3\ GeV/c, \quad |\eta^{\mu}| < 1.$$

These muon cuts were made at the ISAJET generation stage, and so an event was not accepted in ISAJET unless the muons from the $J/\psi$ satisfied these cuts. Furthermore, as discussed previously, the muon chambers in the vicinity of the main ring beam line have suffered a significant depletion in performance due to aging caused by beam line effects. Since the chamber efficiencies are poorly understood in this region we have excluded from consideration any muons that occupy such affected areas. This amounts to a fiducial $\varphi$ cut wherein we require $\varphi_{\mu} \leq 80^{\circ}$ *or* $\varphi_{\mu} \geq 110^{\circ}$.

### Accounting for the Polarization of $J/\psi$ Mesons

The $J/\psi$ is a vector meson and therefore proper account must be taken of the possible effects of $J/\psi$ polarization on the muons accepted in ISAJET and how this in turn relates back to the $J/\psi$ acceptance. Fig.6.11 shows the $J/\psi$ acceptance as a function of $p_T$ of the $J/\psi$ after the kinematic cuts on the muons have been imposed. As the figure shows the acceptance is polarization dependent. $\theta^{*}$ is the angle in the $J/\psi$ rest-frame between the positive muon and the direction of the line of flight of the $J/\psi$ in the lab-frame. The case of longitudinal polarization shows the muons emitted at right angles to the direction of flight of the $J/\psi$. Here the acceptance is greatest since the boost of the muons into the lab frame does not greatly affect the muon momentum. The acceptance is least for transversely polarized $J/\psi$'s since here the muons tend to be produced in the forward and backward directions, and therefore the backward produced muon will suffer a large degradation of momentum after the boost back into the lab. For purposes of further analysis we have used the acceptance curve corresponding to the case of unpolarized $J/\psi$'s ($\alpha = 0$), and used the other two curves for estimating the systematic uncertainty that arises in overall $J/\psi$ acceptance·efficiency due to polarization effects.

### The Combined Acceptance and Efficiency for $J/\psi$ Mesons

We have computed efficiencies and acceptance separately for B-produced $J/\psi$'s and $\chi_c$-produced $J/\psi$'s. The next chapter will show that the data seems to indicate the presence of both an isolated and non-isolated component for the $J/\psi$ signal. The relative proportion of each is: 60% non-isolated and 40% isolated. We have taken the B-produced $J/\psi$'s as the paradigm for the non-isolated component and $\chi_c$-produced $J/\psi$'s as the corresponding paradigm for the isolated component. As a result we have calculated the overall acceptance times efficiency as a weighted sum of those obtained separately for each of the two types of $J/\psi$ Monte Carlo. Table 6.4 lists the values obtained for the combined efficiency times acceptance.

The overall efficiency of the reconstruction-trigger is $13 \pm 2$ %. The average offline cut efficiency is $73 \pm 5$ %.Finally, a correction to the $J/\psi$ combined efficiency must be made for acceptance due to the imposition of the muon kinematic cuts.

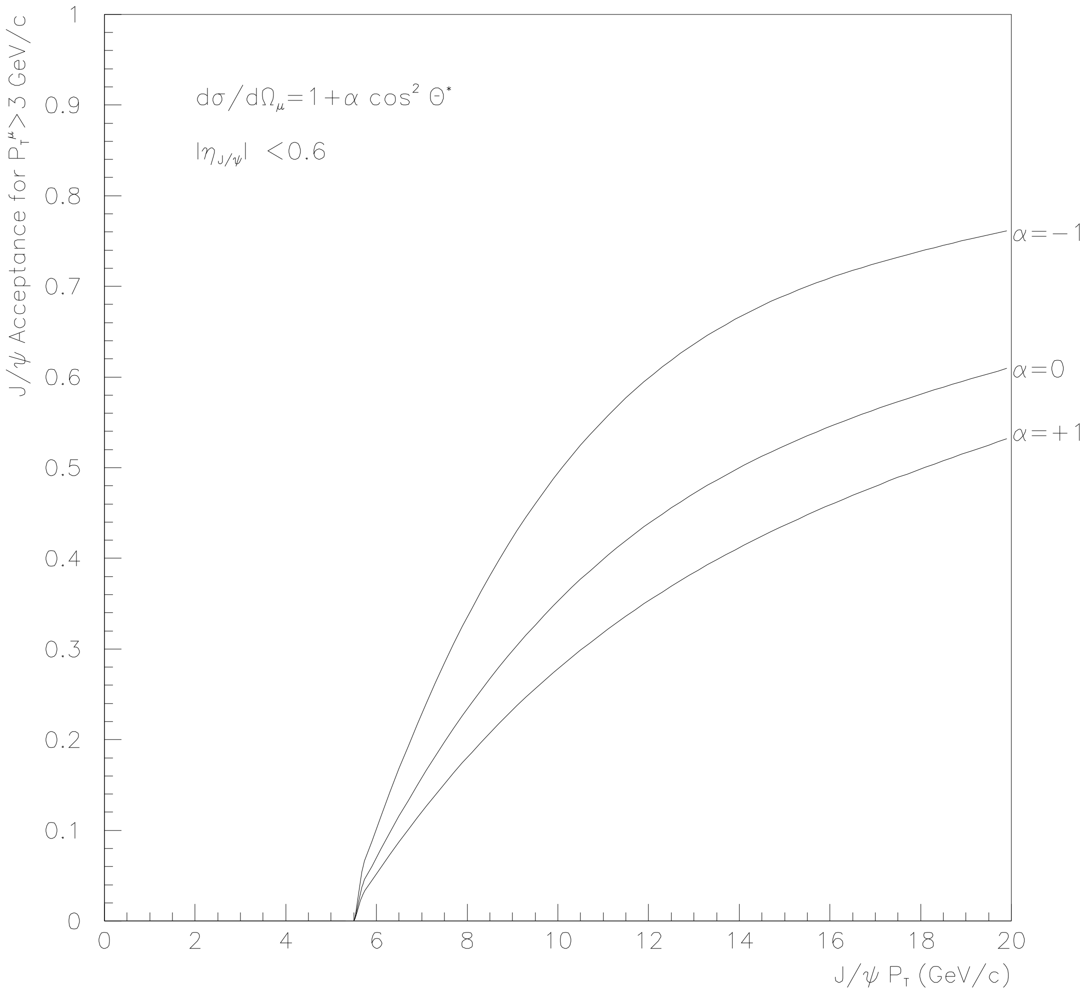


Figure 6.11: Acceptance as a function of $J/\psi P_t$ for cases of different polarizations of the $J/\psi$

| $p_T$ bin (GeV/c) | B-Produced | $\chi_c$-Produced | Weighted Combined |
|---|---|---|---|
| 6-8 | $0.0017 \pm 0.0001$ | $0.0016 \pm 0.0002$ | $0.0017 \pm 0.0001$ |
| 8-10 | $0.0159 \pm 0.0007$ | $0.0128 \pm 0.0010$ | $0.0147 \pm 0.0006$ |
| 10-12 | $0.0418 \pm 0.0017$ | $0.0391 \pm 0.0033$ | $0.0407 \pm 0.0017$ |
| 12-15 | $0.0653 \pm 0.0027$ | $0.0642 \pm 0.0064$ | $0.0649 \pm 0.0030$ |
| 15-20 | $0.1017 \pm 0.0048$ | $0.1119 \pm 0.0165$ | $0.1058 \pm 0.0072$ |

Table 6.4: $J/\psi$ Combined Efficiency·Acceptance

The integrated average of this efficiency correction amounts to 30$\pm$3 % for the case of unpolarized $J/\psi$'s. The integrated average overall $J/\psi$ efficiency-acceptance may be computed from

$$\varepsilon_{J/\psi} = \varepsilon_{(Offline-Cuts)} \cdot \varepsilon_{(Reco-Trigger)} \cdot \varepsilon_{(Acceptance)} \tag{6.1}$$

We have determined that $\varepsilon_{J/\psi} = 0.028 \pm 0.003$. Fig.6.12 shows the combined overall efficiency·acceptance for the $J/\psi$ (assuming unpolarized $J/\psi$'s).

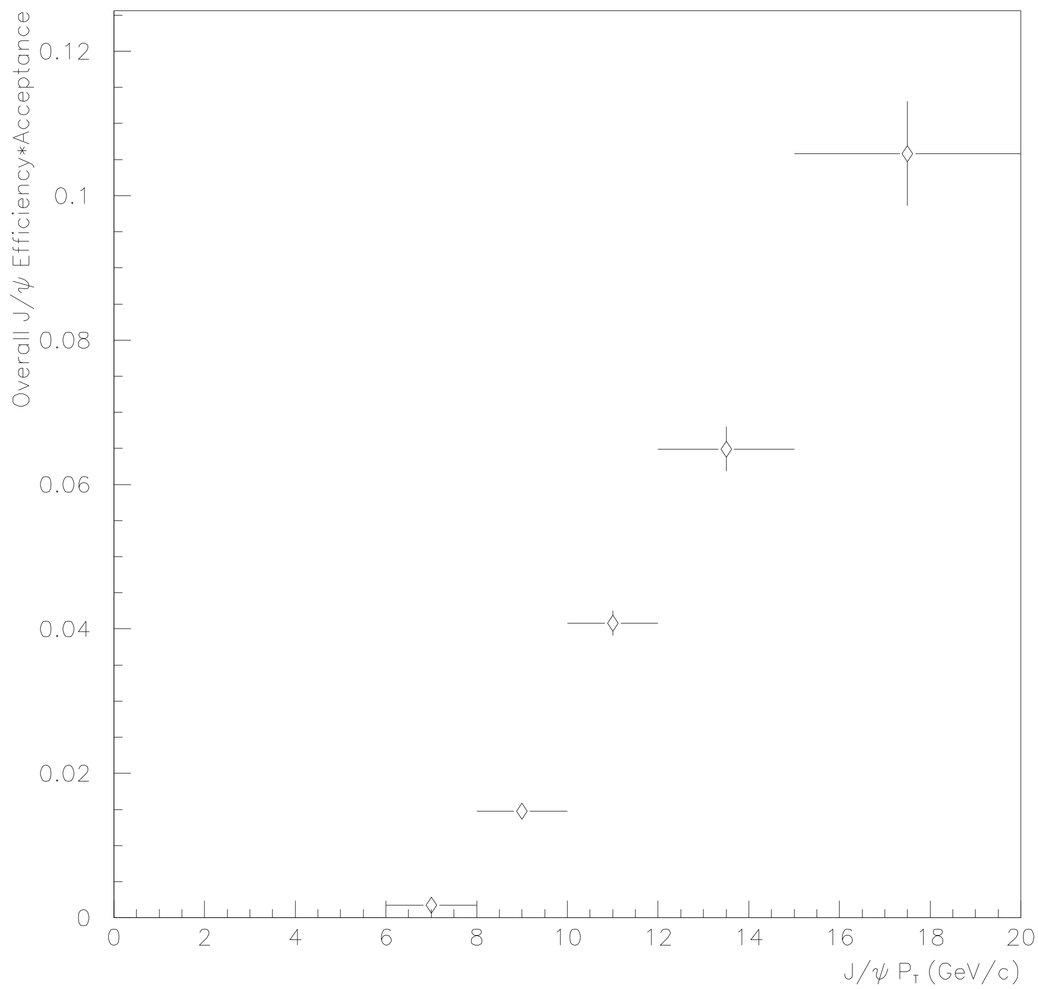


Figure 6.12: Combined Efficiency times Acceptance as a function of $p_T^{\psi}$ for the MU-2-HIGH Trigger

# Chapter 7

# The Inclusive $J/\psi$ Cross Section

## 7.1 Background and the $J/\psi$ Signal

In order to estimate the background and the relative mix of $J/\psi$ 's from the two processes; $B\bar{B} \rightarrow J/\psi X$ , as well as $\chi_c \rightarrow J/\psi + \gamma, J/\psi \rightarrow \mu\mu$ , we make use of the Maximum Likelihood Method as a means of sorting out the various physics processes. In this regard we have considered 6 physics processes, namely,

1. $J/\psi$ 's from B's
2. $J/\psi$ 's from $\chi_c$ 's
3. QCD dimuons from B sequential and parallel decays
4. Drell-Yan dimuons
5. Low-Mass mesons
6. $\pi - K$ decays

We have examined the MU-2-HIGH Post Shutdown data in the dimuon mass interval $0.2 < M_{\mu\mu} < 6.0\ GeV/c^2$. There are a total of 1137 opposite sign dimuons in this interval. Fig.7.1 shows the dimuon distributions obtained.

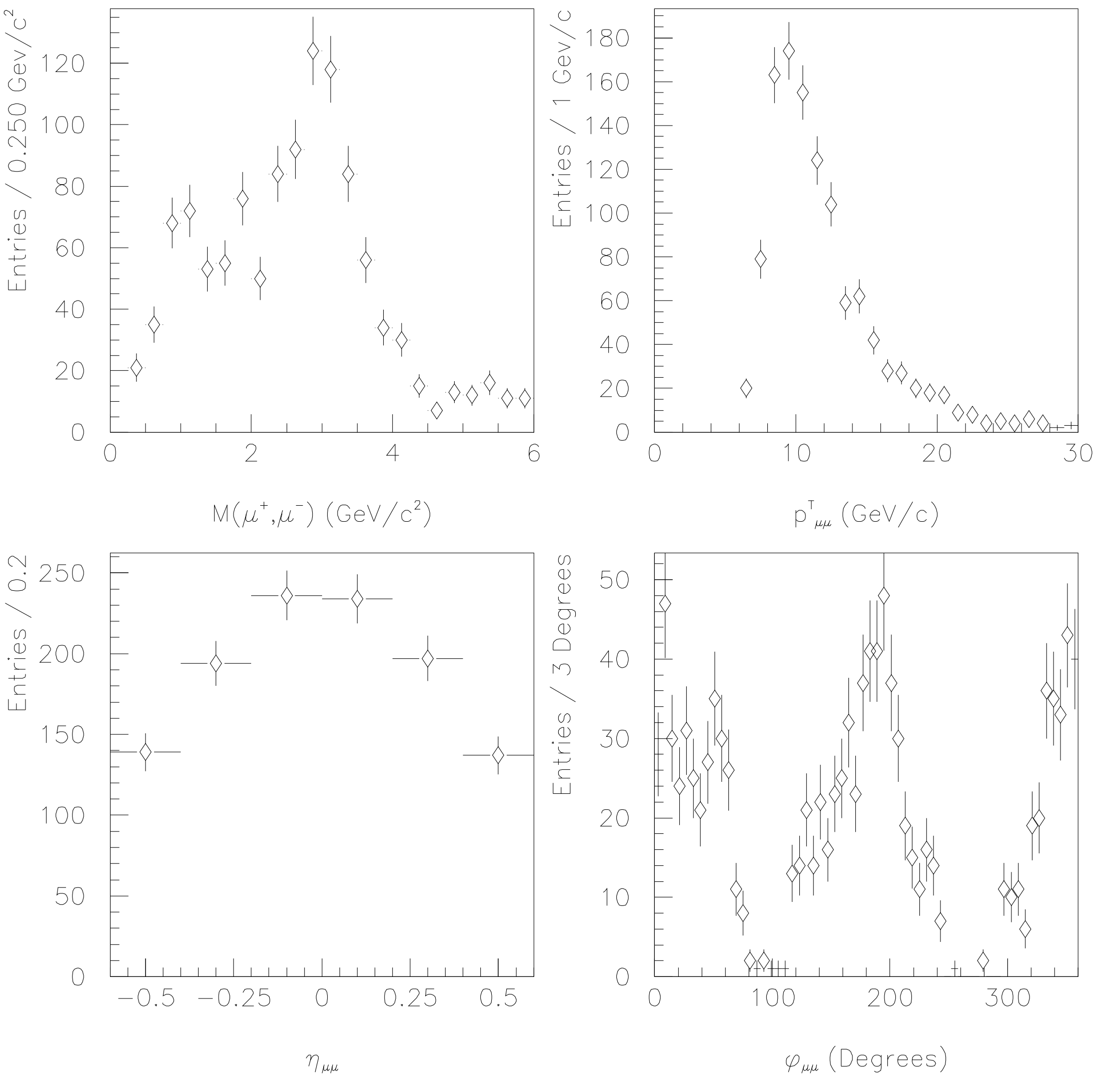


Figure 7.1: Dimuon Distributions obtained under MU-2-HIGH for the Post Shutdown Data.

## 7.2 Maximum Likelihood Determination of Signal and Background Contributions

For each of the previously mentined physics processes we have looked at the distributions of 4 variables: $M_{\mu^+\mu^-}$, $p^T_{\mu^+\mu^-}$, $I^{2NN}_{\mu\mu}$ (2NN isolation), and $p^T_{\mu\mu Rel}$ of the dimuons. From these distributions one may form normalized probability distributions (pdf's) and combine them for each of the physics processes assumed to be present. In this way one may form a correctly normalized Likelihood Function which may be maximized with respect to coefficients that serve to normalize the contribution of each process.

To be more specific, let $x_{ik}$ where $i = 1, \ldots, nevent$ and $k = 1, \ldots, nvar$ represent the $k^{th}$ physics variable for the $i^{th}$ event whose normalized distribution for the $j^{th}$ process is given by $f_{jk}(x_{ik})$, where $j = 1, \ldots, nproc$. Then we may take the Likelihood Function to be

$$£ = \prod_{i=1}^{nevent} \left( \sum_{j=1}^{nproc} A_j \prod_{k=1}^{nvar} f_{jk}(x_{ik}) \right) \tag{7.1}$$

Here the $A_j$ represent normalizing coefficients for the $j^{th}$ process. We may re-express the $A_j$ in terms of independent parameters $\xi_j$ by taking into account the constraint that the sum of the dimuons for each process has to add up to the total number of dimuons observed in the data. For example for the 6 processes considered we may write

$$\begin{aligned}
A_1 &= \xi_1 \\
A_2 &= (1-\xi_1)\xi_2 \\
A_3 &= (1-\xi_1)(1-\xi_2)\xi_3 \\
A_4 &= (1-\xi_1)(1-\xi_2)(1-\xi_3)\xi_4 \\
A_5 &= (1-\xi_1)(1-\xi_2)(1-\xi_3)(1-\xi_4)\xi_5 \\
A_6 &= (1-\xi_1)(1-\xi_2)(1-\xi_3)(1-\xi_4)(1-\xi_5)
\end{aligned} \tag{7.2}$$

By minimizing $-\ln \pounds$ with respect to the $\xi_i$ we obtain likelihood estimates of the $A_j$ giving the amount of the contribution for the $j^{th}$ process. The pdf's $f_{jk}(x_{ik})$ used in the likelihood fit were each normalized to unity, and we employed the 3 distributions corresponding to the dimuon mass (cmass(i,j)), dimuon $p_{T,Rel}$ (cptrel(i,j)), and dimuon isolation $I^{2NN}$ (cisol(i,j)). The distribution corresponding to dimuon $p_T$ (cpt(i,j)) was **not** used in the fitting process. Here $i$ refers to the $i^{th}$ event and $j$ refers to the $j^{th}$ process.

The shapes of the normalized distributions for each process were obtained from ISAJET Monte Carlo events run through the full detector and trigger simulations. These shapes were then parametrized and evaluated within the Likelihood Function using the actual data points themselves. Fig. 7.2 shows the results of the Maximum Likelihood fit to the data. The figure showing the dimuon $p_T$ is a pure prediction of the fitting process, since it was not part of the likelihood fitting procedure. With regard to the figure showing the dimuon $p^T_{\mu\mu\ rel}$, the first bin indicates those events for which no jet was reconstructed. Fig.7.3 shows plots of the negative log likelihood function versus the primary fit parameters $\xi_k, (k = 1, \ldots, 5)$. Each of these plots shows a good parabolic behaviour in the neighborhood of its corresponding minimum. From the simultaneous maximum likelihood fit we summarize the contributions of the fitted processes in Table 7.1.

The parametrizations used in the Likelihood fit are those that were shown in Chapter 5, with two exceptions. The variable $I^{2NN}_{\mu\mu}$ was not described well by either the Low Mass Meson (LMM) Monte Carlo or the $\pi - K$ Monte Carlo. In general the data apppears to be more non-isolated than the Monte Carlo predicts for these two processes. The basic shapes of the parametrizations were used but these shapes were translated along the abscissa axis in the positive direction by

| Physics Process | Number of Events |
|---|---|
| B-produced $J/\psi$ | $238 \pm 40$ |
| $\chi_c$ produced $J/\psi$ | $176 \pm 31$ |
| QCD | $305 \pm 37$ |
| Drell-Yan | $152 \pm 20$ |
| Low-Mass Mesons | $45 \pm 17$ |
| $\pi - K$ decays | $220 \pm 21$ |

Table 7.1: Fitted Contributions of various Dimuon Physics Processes.

an amount determined from fits to the data.

Having fitted for the normalizing coefficients $A_j$ we have checked for consistency of these fits by using as weights the probability that a given event is due to a given process. For each event the weight or probability that the $i^{th}$ event was caused by the $j^{th}$ process was calculated as:

$$W_{i,j} = \frac{A_j \cdot cmass(i,j) \cdot cptrel(i,j) \cdot cisol(i,j)}{\sum_j A_j \cdot cmass(i,j) \cdot cptrel(i,j) \cdot cisol(i,j)} \tag{7.3}$$

Fig.7.4 shows the projected mass distributions obtained for each of the 6 different processes by weighting the histograms with the probabilties as calculated above. Superimposed on each plot is the parametrization used for each process normalized to $A_j \cdot N_{\mu\mu}$ where $N_{\mu\mu}$ represents the total number of observed dimuons. Similarly, Fig.7.5 and Fig.7.6 show the projected dimuon $p_{T,Rel}$ and dimuon isolation $I_{\mu\mu}^{2NN}$ distributions respectively. In Fig.7.7 we show the purely predicted dimuon $p_T$ using the probabilities calculated above.

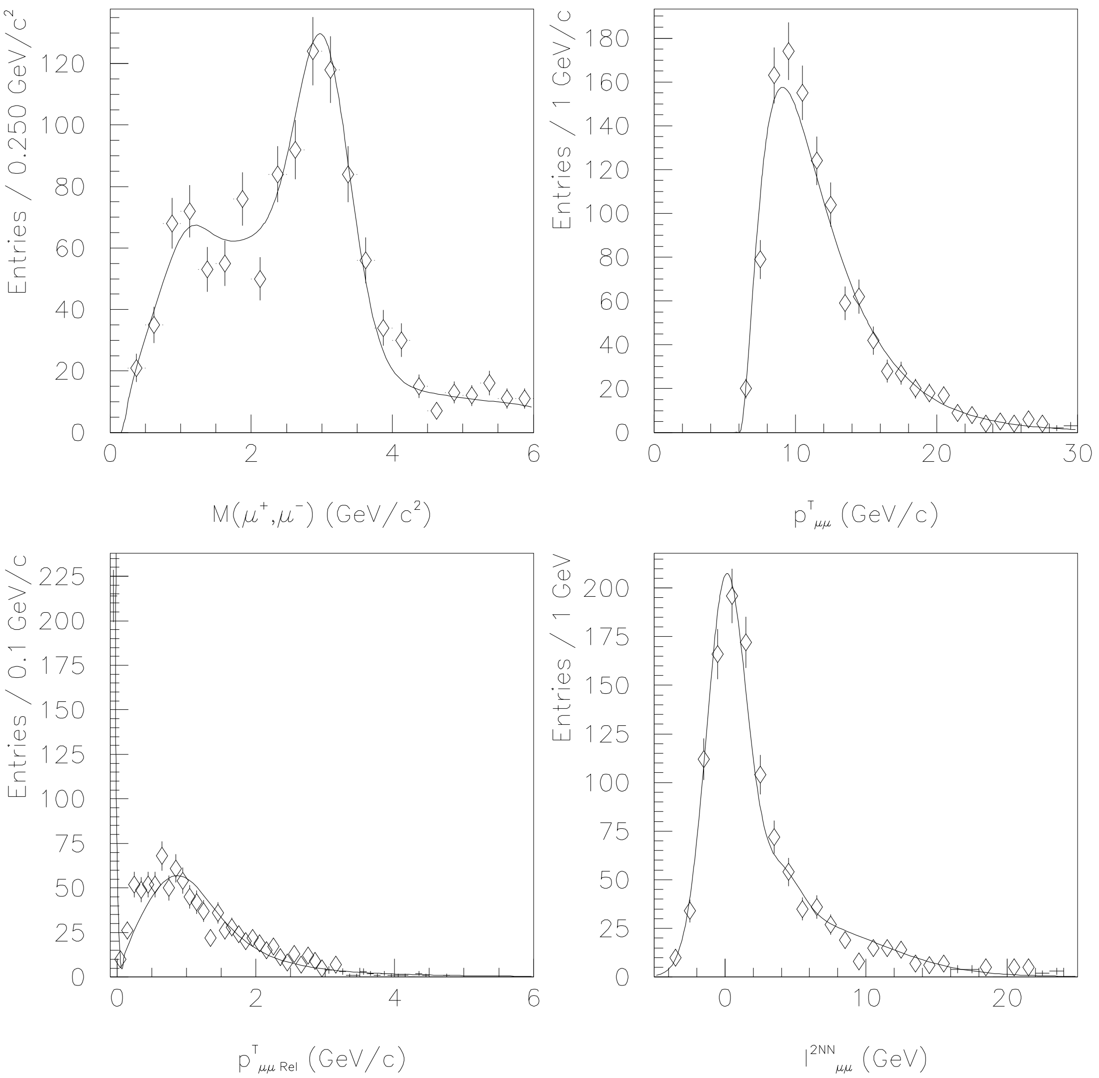


Figure 7.2: Simultaneous Maximum Likelihood Fit to the data for various distributions. The fit to the distribution for the dimuon $p^T_{\mu\mu}$ is actually a prediction of the likelihood calculations.

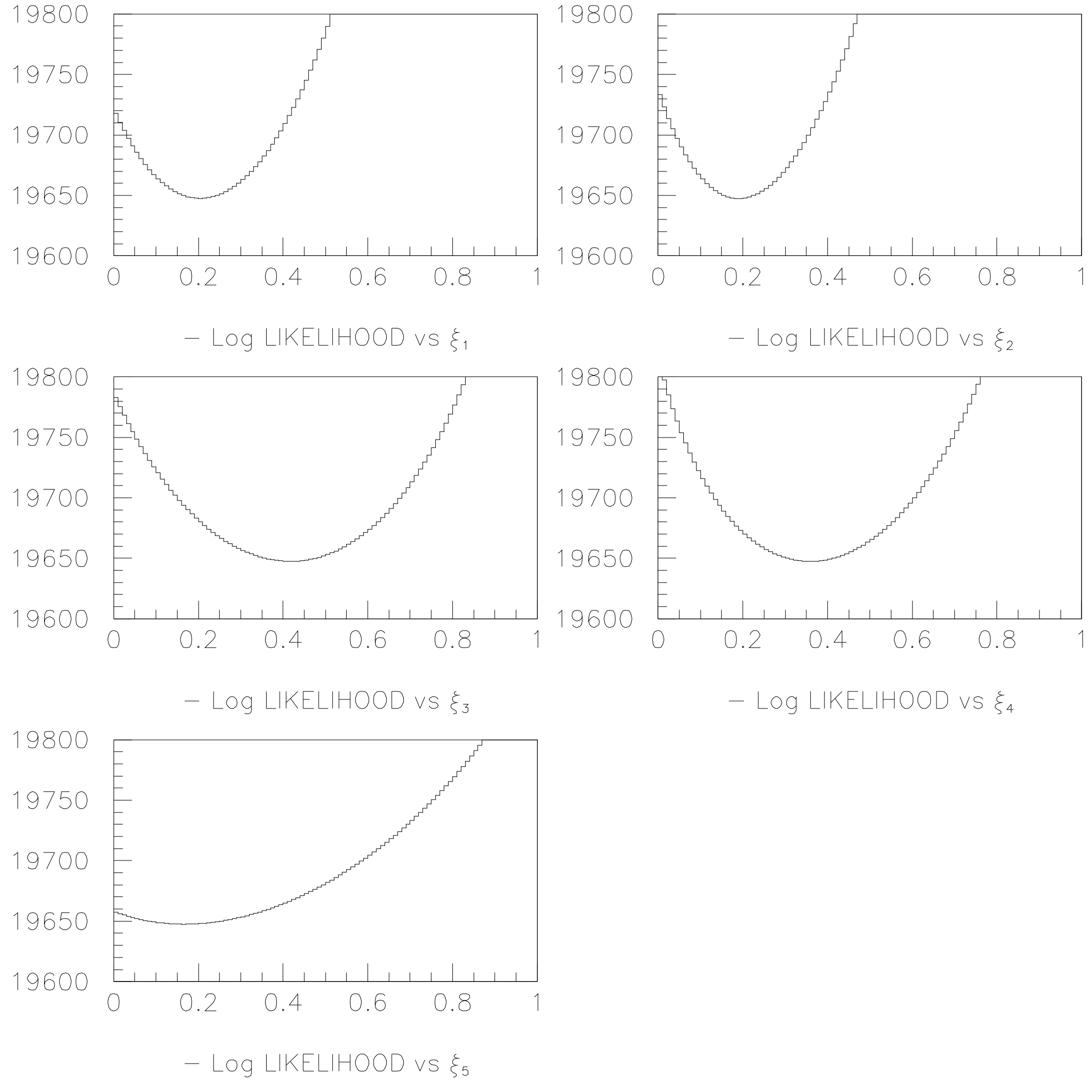


Figure 7.3: Negative Log Likelihood vs Primary Fit Parameters $\xi_k, (k = 1, \ldots, 5)$.

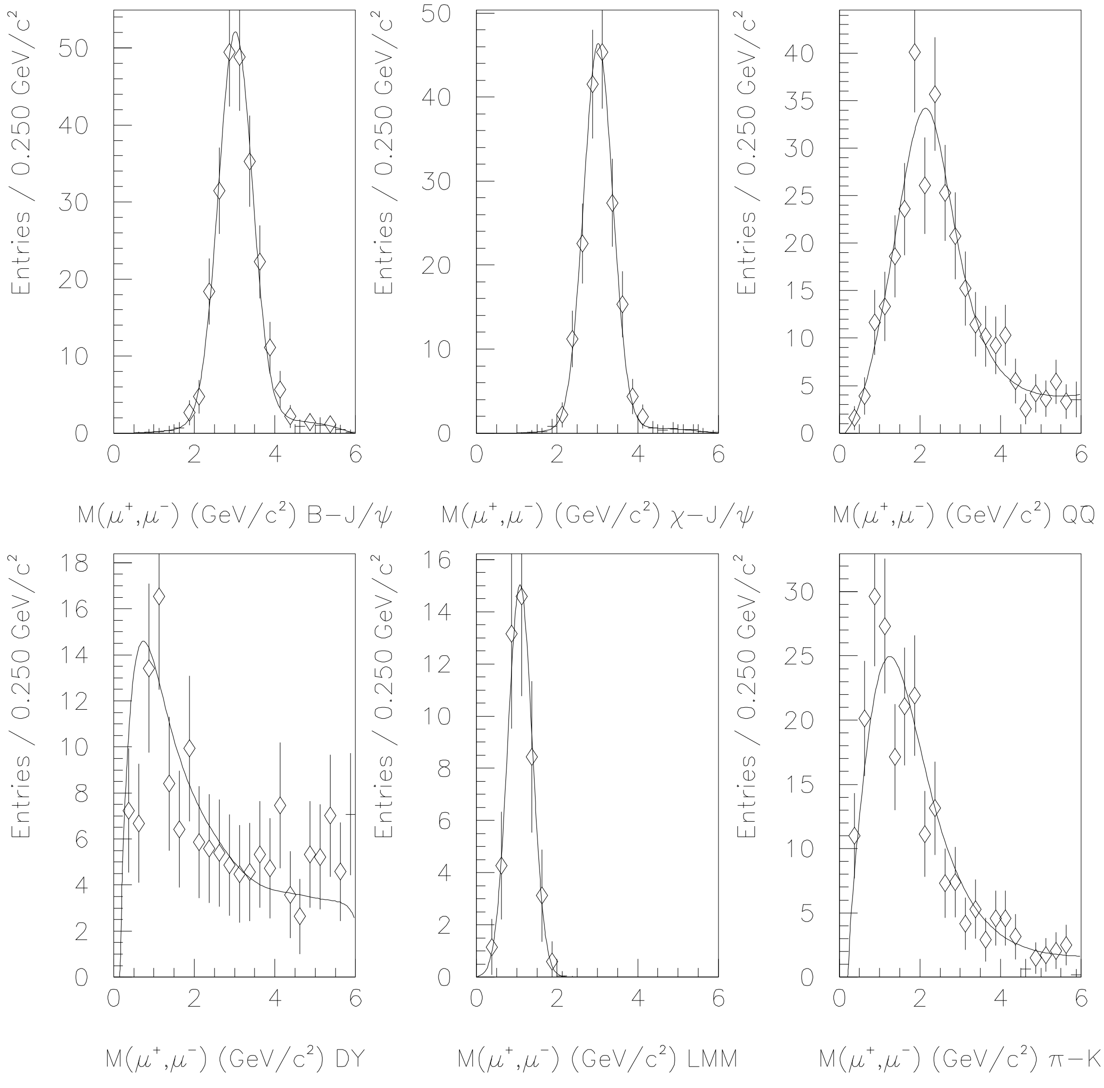


Figure 7.4: Projected mass distributions for each of the processes based upon the Maximum Likelihood fit to the data: (a) B-produced $J/\psi$'s, (b) $\chi_c$-produced $J/\psi$'s, (c) $Q\bar{Q}$, (d) Drell-Yan, (e) Low Mass Mesons, (f) $\pi - K$.

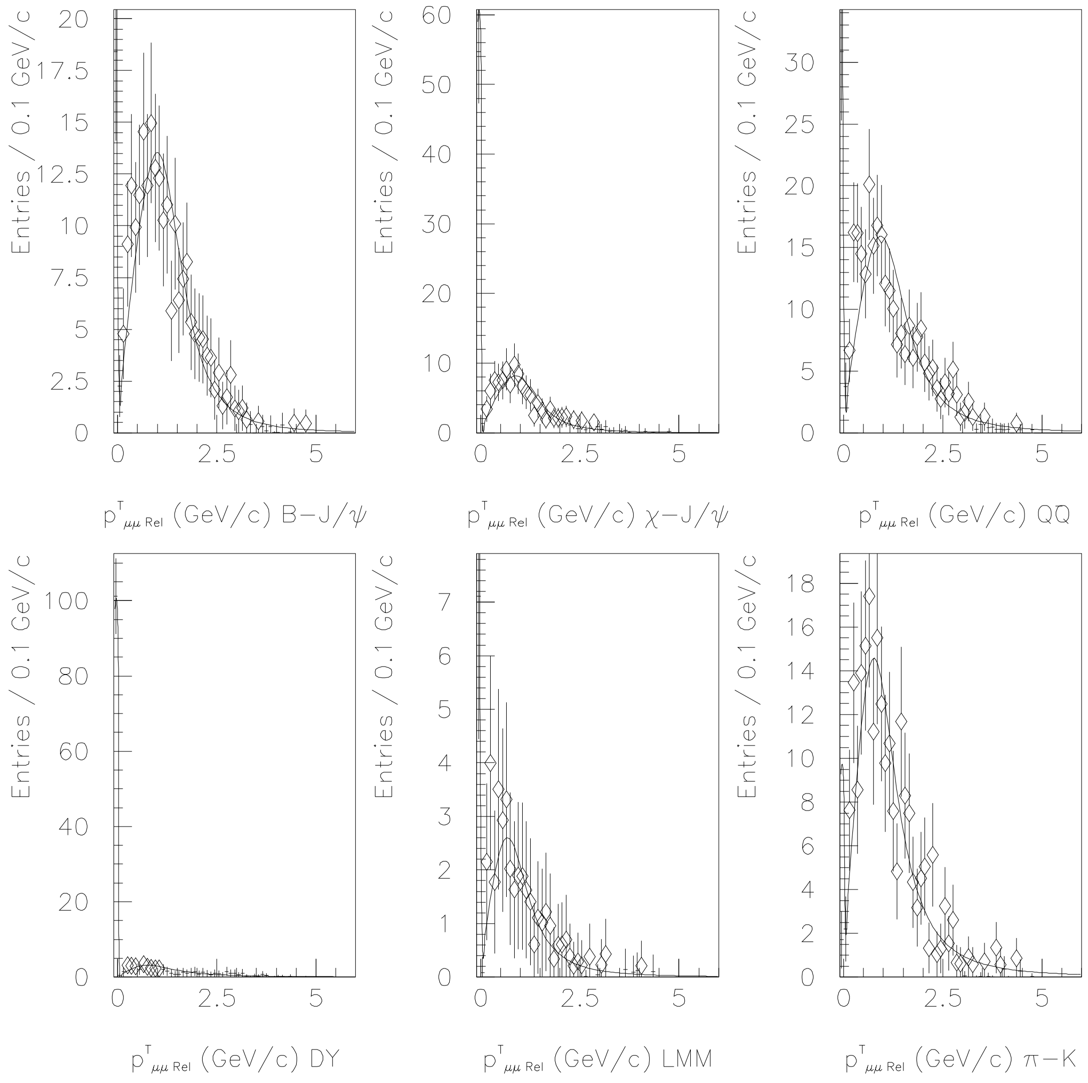


Figure 7.5: Projected $p_{T,Rel}$ distributions for each of the processes based upon the Maximum Likelihood fit to the data: (a) B-produced $J/\psi$'s, (b) $\chi_c$-produced $J/\psi$'s, (c) $Q\bar{Q}$, (d) Drell-Yan, (e) Low Mass Mesons, (f) $\pi - K$.

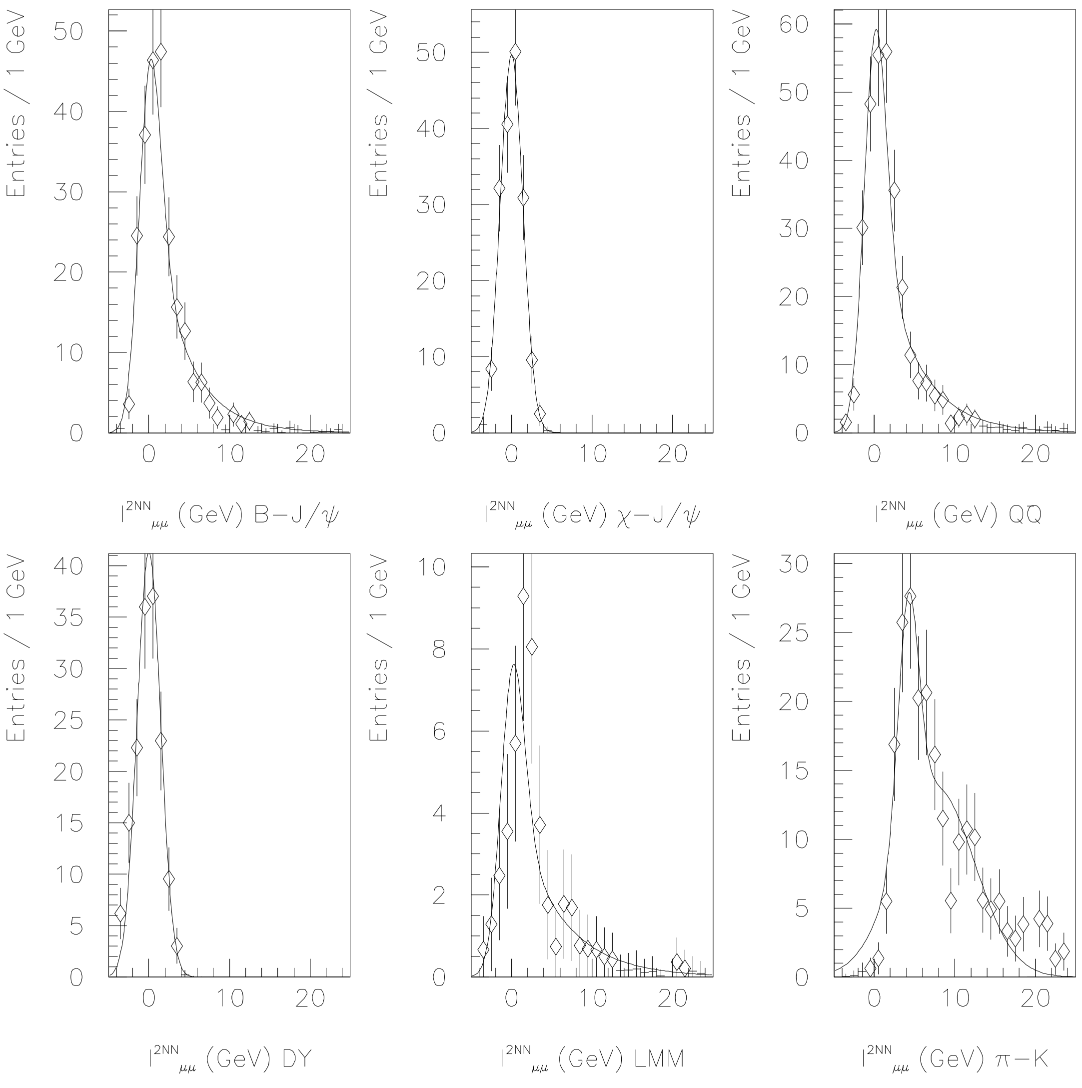


Figure 7.6: Projected isolation distributions for each of the processes based upon the Maximum Likelihood fit to the data: (a) B-produced $J/\psi$'s, (b) $\chi_c$-produced $J/\psi$'s, (c) $Q\bar{Q}$, (d) Drell-Yan, (e) Low Mass Mesons, (f) $\pi - K$.

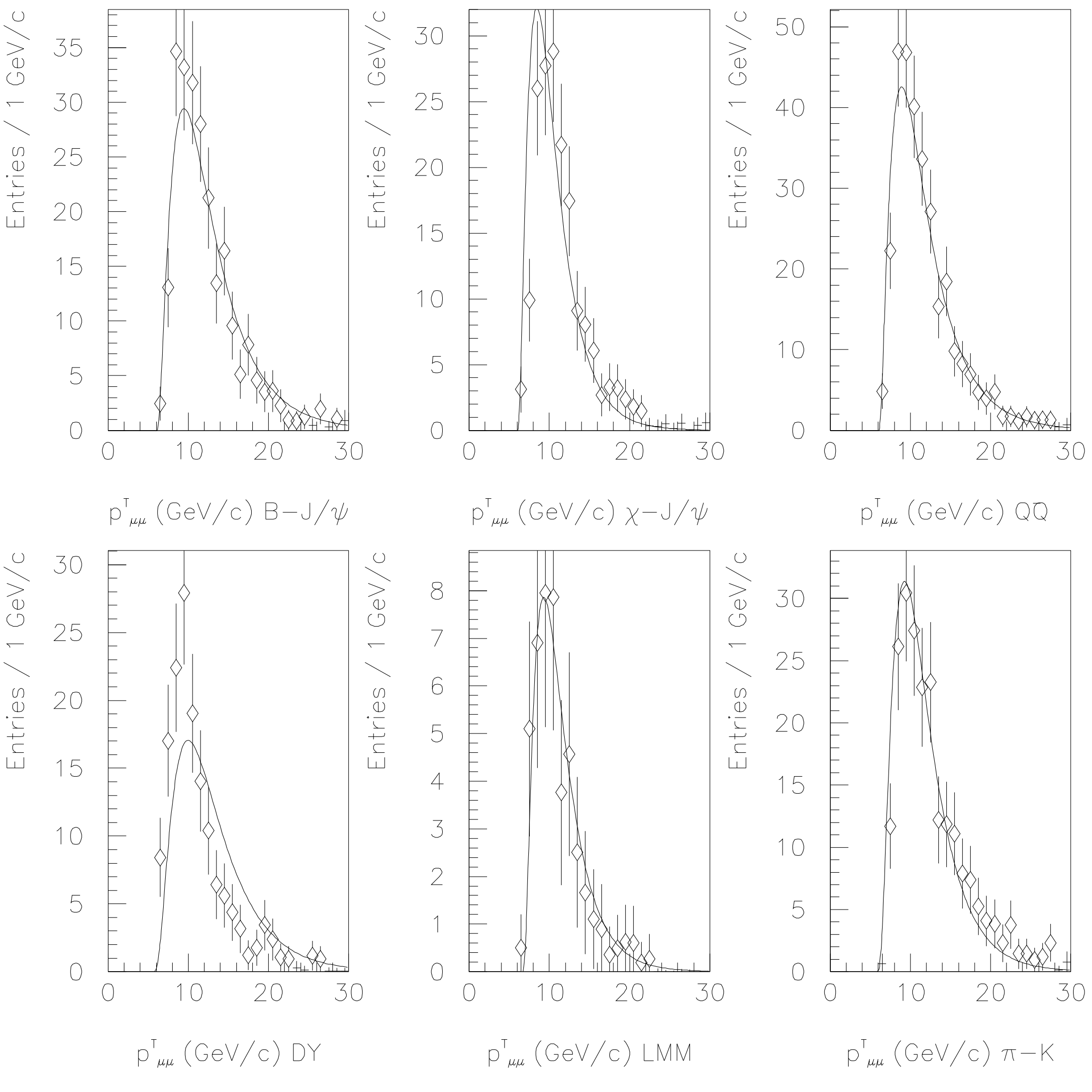


Figure 7.7: Predicted $p_T$ distributions for each of the processes based upon the Maximum Likelihood fit to the data: (a) B-produced $J/\psi$'s, (b) $\chi_c$-produced $J/\psi$'s, (c) $Q\bar{Q}$, (d) Drell-Yan, (e) Low Mass Mesons, (f) $\pi - K$.

## 7.3 The Inclusive $J/\psi$ Cross Section

The result of the fit discussed in the previous section indicated that the number of $J/\psi$ events is $414 \pm 50$. Fig.7.8 shows the fitted dimuon mass spectrum with the sum of all background processes that interfere with the $J/\psi$ signal. The errors quoted here take account of the full covariance matrix that resulted from the fit. Hence all correlations between signal and background have been properly taken into account.

As a check on the likelihood fitting procedure we have done a separate fit to the mass alone in bins of dimuon $p_T$. The same mass parametrizations were used in the bin-by-bin fit as in the likelihood fit, however the $\chi_c$ produced $J/\psi$ mass parametrization was dropped and only the $B$ produced $J/\psi$ mass parametrization was used in the fitting process. The mass and width of the $B$ produced $J/\psi$ mass parametrization were fixed at 3.05 $GeV/c^2$ and 0.38 $GeV/c^2$ respectively. We did not notice any significant change in the mass or width of the $J/\psi$ signal as we progressed through the various dimuon $p_T$ bins. Fig.7.10 shows the results of the bin-by-bin mass fit. We summarize the binned fitting procedure in Table 7.2. The results are consistent with those obtained on the basis of the full likelihood fit. In particular we obtain $416 \pm 32$ $J/\psi$ events for $p^T_{J/\psi} > 8$ $GeV/c$.

In order to extract the inclusive $J/\psi$ cross section we have separately unfolded the likelihood fitted $p_T$ spectra for the B-produced and $\chi_c$-produced $J/\psi$'s. This unfolding technique makes use of Bayes Theorem [67] in conjunction with $p_T$ smearing matrices derived from the $J/\psi$ Monte Carlo. Fig.7.9 shows the results of unfolding the $J/\psi$ $p_T$ spectra individually for B-produced and $\chi_c$-produced $J/\psi$'s and then adding the two unsmeared distributions together to obtain the inclusive $p^T_{J/\psi}$ spectrum. Since we know the integrated luminosity is 6.6 $pb^{-1}$, and since the efficiency is known as a function of the $J/\psi$ $p_T$, we may compute the inclusive $J/\psi$ cross section. Fig.7.11 shows the inclusive $J/\psi$ cross section. The two solid curves represent the range of theoretical uncertainty in the total cross section due to the choice of possible factorization and renormalization scales, and $\Lambda_{QCD}$ [68]. The results are also summarized in Table 7.3.

The cross section calculation did not make use of the $6-8$ $GeV/c$ or the $20-30$ $GeV/c$ $J/\psi$ $p_T$ bins since there did not appear to be a clear enough $J/\psi$ signal present in either of these. In the bins that were used the likelihood fit gave $375 \pm 31$ $J/\psi$ events. The statistical errors quoted for the $p_T$ bins listed in Table 7.3 were obtained by calculating the square root of the number of equivalent events, $\sqrt{N_e}$, that fell into each of the 4 indicated $J/\psi$ $p_T$ bins. For a given $J/\psi$ $p_T$ bin the number of equivalent events was obtained as follows:

$$N_e = \frac{(\sum_{i=1,N}(W_i(b) + W_i(\chi_c)))^2}{\sum_{i=1,N}(W_i(b) + W_i(\chi_c))^2} \tag{7.4}$$

where the sum is over all events that fell into the given $J/\psi$ $p_T$ bin, and $W_i(b)$ and $W_i(\chi_c)$ are the probabilities for $B$-produced and $\chi_c$-produced $J/\psi$ s calculated as in equation 7.3. On the basis of these results we choose to estimate our overall statistical error as 8.3%. We interpret a part of the error obtained by using the full covariance matrix derived from the likelihood fit as being due to this 8.3% statistical error, and the balance as being attributable to an 8.8% systematic error on our ability to normalize the background to the $J/\psi$ signal.

For the integrated cross section we obtain

$$\begin{aligned} Br(J/\psi \rightarrow \mu^+\mu^-) \cdot \sigma(p\bar{p} \rightarrow J/\psi + X) &= 2.00 \pm 0.17(stat) \pm 0.50(sys) nb \\ & \quad p^T_{J/\psi} > 8.0\ GeV/c, |\eta_{J/\psi}| < 0.6. \end{aligned}$$

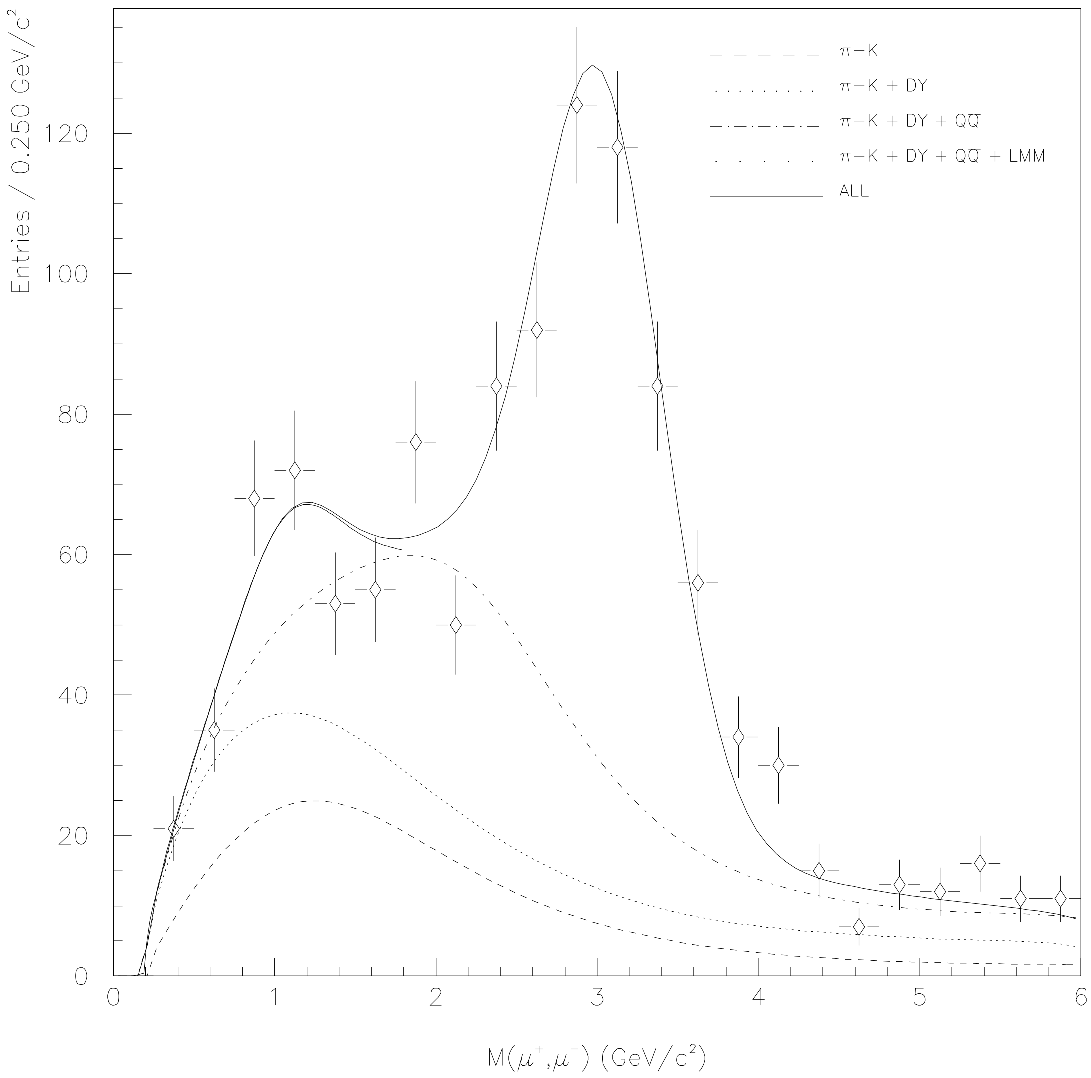


Figure 7.8: Fitted dimuon mass spectrum showing sum of all background to the $J/\psi$ signal

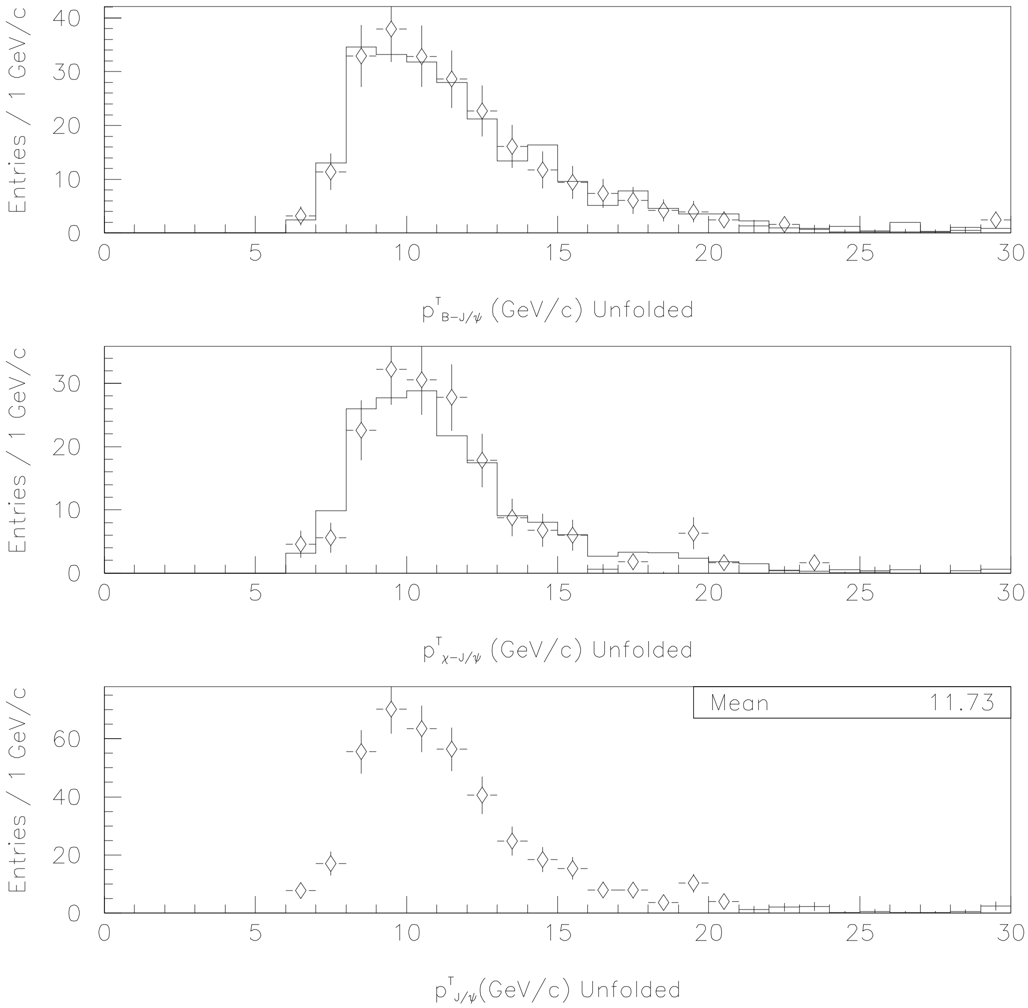


Figure 7.9: Unfolded $J/\psi$ $p_T$ spectra. (Top) B-produced $J/\psi$'s. (Middle) $\chi_c$-produced $J/\psi$'s. (Bottom) the sum of both distributions. Superimposed on the upper plots is the fitted prediction.

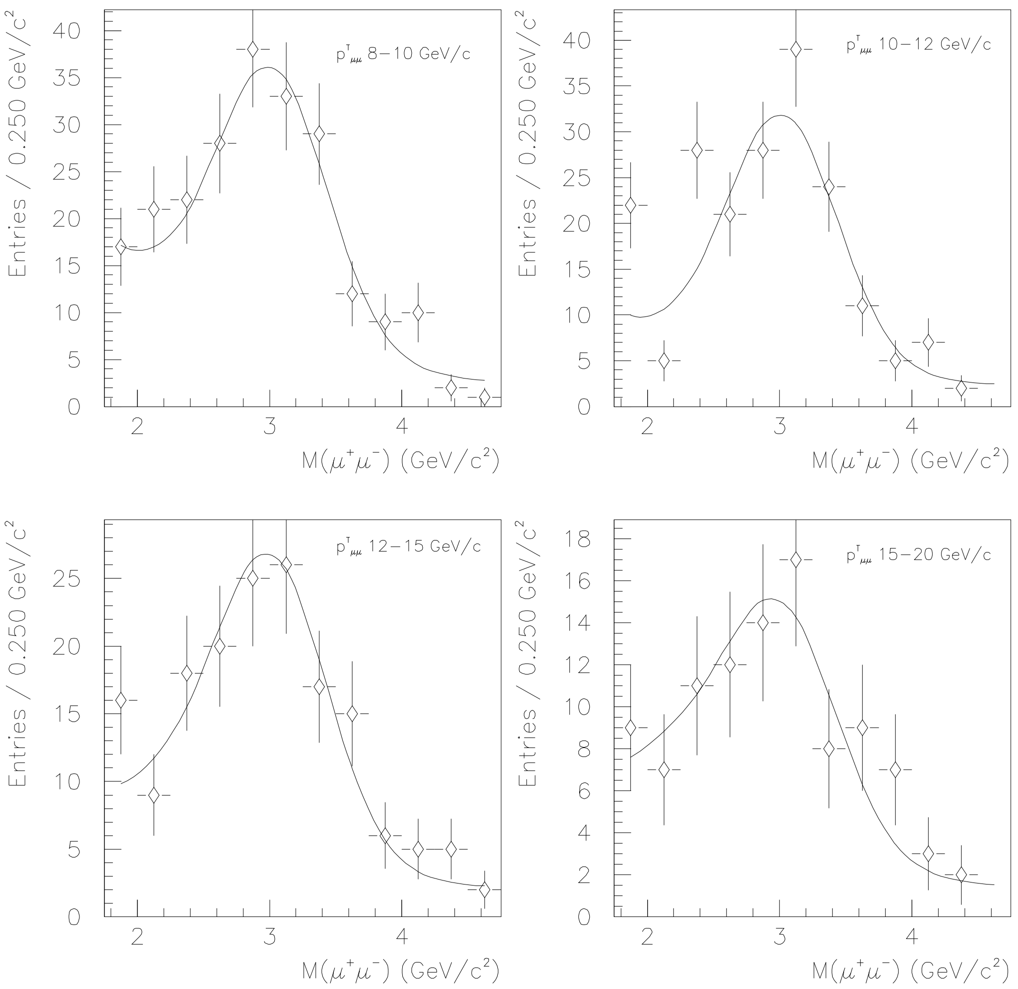


Figure 7.10: Mass fit to $J/\psi$ signal in bins of dimuon $p_T$.

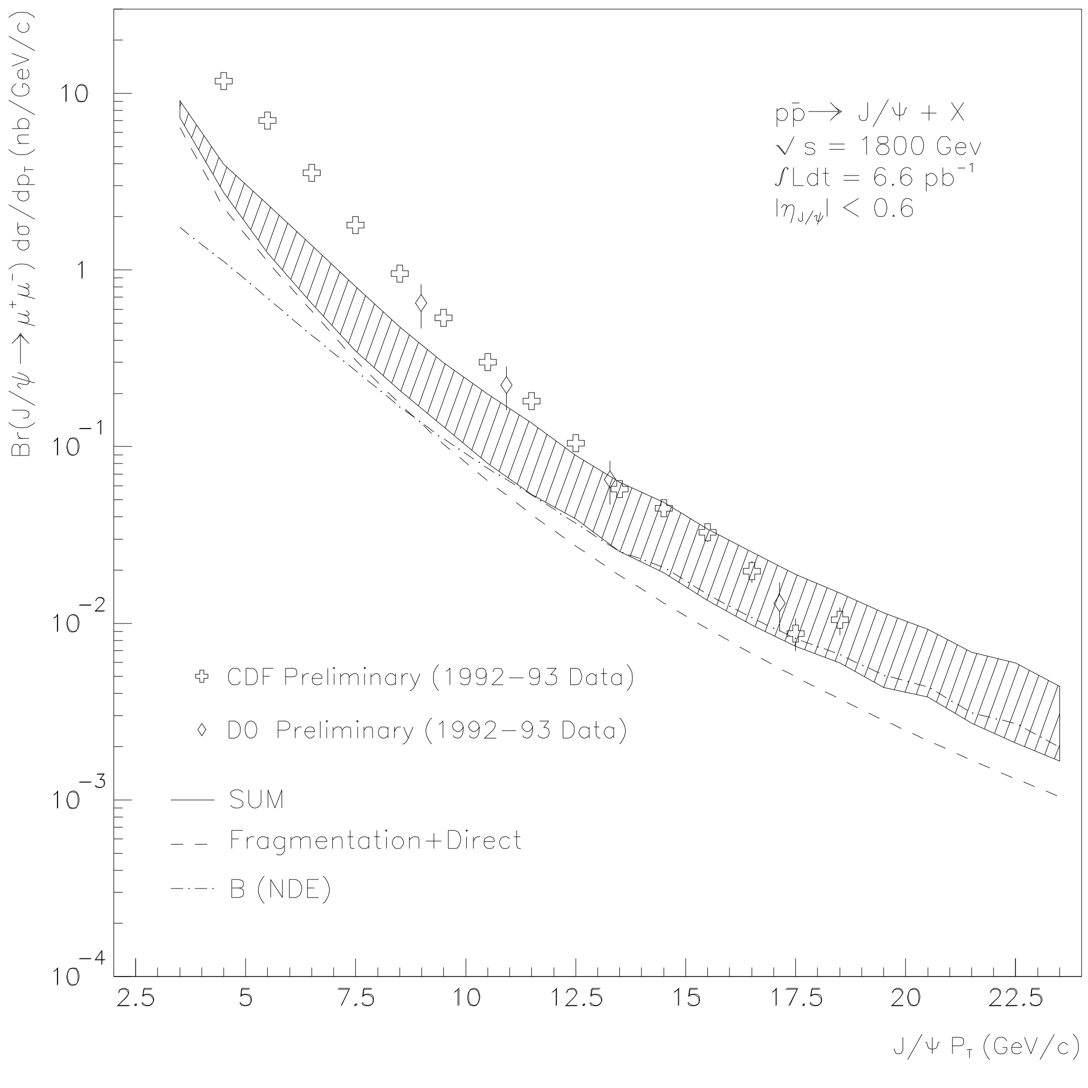


Figure 7.11: Inclusive $J/\psi$ cross section as a function of $J/\psi$ $p_T$

| $p^T_{J/\psi}$ Bin | $\langle p^T_{J/\psi} \rangle$ | $N_{J/\psi}$ |
|---|---|---|
| 8-10 | 8.99 | $137 \pm 22$ |
| 10-12 | 10.93 | $129 \pm 15$ |
| 12-15 | 13.28 | $100 \pm 14$ |
| 15-20 | 17.14 | $50 \pm 11$ |

Table 7.2: Results of Mass fit to $J/\psi$ signal in bins of dimuon $p_T$.

| $p^T_{J/\psi}$ Bin | $\langle p^T_{J/\psi} \rangle$ | Efficiency | $N_{J/\psi}$ | $Br \cdot d\sigma/dp^T$ (nb) |
|---|---|---|---|---|
| 8-10 | 9.06 | 0.0147 | $126 \pm 18$ | $0.649 \pm 0.093$ |
| 10-12 | 10.97 | 0.0407 | $120 \pm 17$ | $0.223 \pm 0.032$ |
| 12-15 | 13.24 | 0.0649 | $84 \pm 15$ | $0.065 \pm 0.012$ |
| 15-20 | 17.18 | 0.1058 | $45 \pm 11$ | $0.013 \pm 0.003$ |

Table 7.3: Inclusive $J/\psi$ cross section from Maximum Likelihood Fit

### 7.3.1 Systematic Errors

The main sources of systematic error involved in the calculation of the inclusive $J/\psi$ cross section are the following:

- **Offline Cuts.**
- **Detector Simulation**. We include as parts of this error contributions arising from chamber efficiencies, and the Monte Carlo trigger simulation [69].
- **Background Subtraction**. We estimate a 12% error that arises from uncertainties on the overall shapes of the parametrizations of background physics processes and, as discussed previously, an 8.8% error due to our inability to acheive a perfect estimate of the background normalizations.

| Source | Systematic Error |
|---|---|
| Offline Cuts | 6% |
| Detector Simulation | 15% |
| Background Subtraction | 15% |
| $J/\psi$ Polarization | $\pm^{25\%}_{28\%}$ |
| Luminosity | 12% |

Table 7.4: Sources of Systematic Error on the $J/\psi$ crosss section

- **Luminosity**
- **Polarization**. There is an additional systematic uncertainty of $\pm^{25\%}_{28\%}$ due to the unknown polarization of the $J/\psi$. However we have not included this error in our cross section plot.

Table 7.4 summarizes the errors on the $J/\psi$ cross section due to the above mentioned sources.

## 7.4 Discussion

We have noted previously that the fitted number of $B$-produced $J/\psi$'s is $238 \pm 40$, while the fitted number of $\chi_c$-produced $J/\psi$'s is $176 \pm 31$. In all, we have calculated the total number of fitted $J/\psi$'s at $414 \pm 50$. We shoud further mention that due to our limited mass resolution of 0.38 $GeV/c^2$ for the $J/\psi$ we are unable to observe any evidence of a $\psi(2S)$ signal (the mass of the $\psi(2S)$ is given as 3.686 $GeV$). However we hold open the possibility that there may be some unknown but probably quite small admixture of $\psi(2S)$ states present in the $J/\psi$ sample. Thus all of our results pertaining to the $J/\psi$ should be considered with this proviso in mind.

One of the primary goals of this thesis is to determine $F_b$, the fraction of

$J/\psi$'s that are produced by the weak decays of B mesons. However we do **not** claim at this point that $F_b = 238/414 = 0.575$. On several previous occasions we have stated that we are unable to simulate the production of $J/\psi$'s via the Fragmentation mechanism (due to lack of the relevant Monte Carlo). We therefore expect that if the fragmentation mechanism is indeed at work, then our collection of $J/\psi$ data includes some unknown contribution from this mechanism whose gross topological properties should be closest in nature to those exhibited by the $B$-produced $J/\psi$'s. The chief distinction between $B$-production and $\chi_c$-production of $J/\psi$ mesons (apart from displaced vertices, which we intend to consider in the next chapter) centers around their calorimeter isolation properties. Both $B$-produced and Fragmentation-produced $J/\psi$'s should be more non-isolated than the $\chi_c$-produced variety. Indeed we have stated previously our intention to take the $B$-produced Monte Carlo as the paradigm for non-isolated $J/\psi$ production, while the $\chi_c$ Monte Carlo is taken as the corresponding paradigm for isolated $J/\psi$ production. We therefore choose to interpret the ratio $238/414 = 0.575$ as the fraction of non-isolated $J/\psi$'s, that is we take

$$F_{non-iso} = 0.575 \pm 0.119 \tag{7.5}$$

$$F_{iso} = 0.425 \pm 0.119 \tag{7.6}$$

We feel justified in making this interpretation by examining the $p^T_{\mu\mu rel}$ and $I^{2NN}_{\mu\mu}$ distributions obtained for $B$ and $\chi_c$ produced $J/\psi$'s. In particular, the former distribution indicates that 33% of the $\chi_c$-produced $J/\psi$ mesons do not have an associated reconstructed jet, whereas only 11% of $B$-produced $J/\psi$'s have no associated jet.

# Chapter 8

# Separation of $J/\psi$ Production Mechanisms

As mentioned several times previously, there are expected to be three significant sources of $J/\psi$ production. In this chapter we attempt to determine $F_b$ , that is the fraction of B-Produced $J/\psi's$, amd $F_\chi$ , the fraction of $J/\psi's$ that are produced via radiative decays through $\chi_c$ states. Table 8.1 lists the salient characteristics to be expected for each mechanism associated with $J/\psi$ production.

## 8.1 Impact Parameter Analysis

Without a Monte Carlo description of the Fragmentation Mechanism for the production of $J/\psi$ mesons, the determination of $F_b$ based upon $J/\psi$ event topology as typified in calorimeter isolation is perhaps ambiguous. The fragmentation mechanism should produce $J/\psi$'s which exhibit the same non-isolation characteristics as $b$-produced $J/\psi$'s. However one clear distiction between the two mechanisms centers around the idea of displaced vertices. B-produced $J/\psi$'s should show displaced vertices and therefore be of a non-prompt nature [70]. Although the fragmentation mechanism will produce non-isolated $J/\psi$'s there certainly should

| Production Mechanisms | Expected Characteristics |
|---|---|
| BPM-produced $J/\psi$ | Non-isolated<br>Non-Prompt (displaced vertex)<br>Addditional $b$-jet in event |
| CPM-produced $J/\psi$ | Isolated<br>Prompt |
| Fragmentation-produced $J/\psi$ | Non-Isolated<br>Prompt |

Table 8.1: Characteristicics expected in $J/\psi$ events for the various production mechanisms

be no indication of any displaced vertices in this mechanism. Hence the distinction of being either prompt or non-prompt should enable us to unambiguously separate out the contribution of $b$-production in the overall process of $J/\psi$ production.

The presence of displaced vertices in $J/\psi$ events may be detected by examining muon impact parameters relative to the primary event vertex. Events which are of a prompt nature should show impact parameter distributions that do not exhibit any long decay-like tails. To first order we might even expect that such events would exhibit nearly Gaussian distributions in the impact parameters of the muons. However muons originating from decaying particles with relatively long lifetimes (such as the B-hadrons) should exhibit skewed distributions with significant tails that reflect the underlying decay mechanism at work. We therefore proceed to a detailed examination of impact parameters observed in $J/\psi$ events. We make note of the fact that the impact parameters we deal with are projections of the $3-d$ or space impact parameters onto the $r-\phi$ plane, that is the plane transverse to the beam axis. We also note that the impact parameters are signed. The sign convention is as follows: If a muon from a dimuon pair appears to cross the direction of the associated jet axis (or dimuon axis if there is no asscociated jet) in front of the primary vertex then the impact parameter is positive, otherwise it is negative. Fig.8.1 shows in more detail the impact parameter sign convention.

### 8.1.1 Central Detector Performance and Beam Position Determination

#### Central Detector Performance

The impact parameter analysis makes use of two of the component detectors that comprise the DØ Central Tracking System; namely the CDC and VTX central tracking chambers. Fig.8.2 shows an $r-z$ profile view of the entire CD tracking system. As stated earlier we intend to deal with transverse $r-\phi$ impact parameters, therefore we show in Fig.8.3 an end-on, or $r-\phi$ view of several segments of the CDC, while Fig.8.4 shows a similar end-on view of a quadrant of the VTX.

The sense wires are used to determine $r-\phi$ positions of hits. The delay liness propagate signals induced from the nearest sense wire and a measurement of the difference of arrival times at the two ends gives the $z$ position of the hits. Pattern recognition algorithms assemble the hit information into reconstructed tracks in both the $r-\phi$ and $r-z$ projections. Full 3-d fits are then made and Zebra bank structures retain the track information thus obtained. Each track has asssociated with it the following quantities: $x, y$ coordinates of the $xy$ center of gravity of hits along the track, the azimuthal angle $\phi$ in the $r-\phi$ plane, the $z$ coordinate obtained from delay line readout, and the polar angle $\theta$ in the $r-z$ plane.

As stated in Chapter 3, the $r-\phi$ position resolution for the CDC has been measured to vary between $150-200$ $\mu m$, while the VTX $r-\phi$ position resolution is approximately 60 $\mu m$. Since the average B-hadron lifetime is $\approx 1.537\times10^{-12}$ $s$, this implies a $c \cdot \tau = 459\ \mu m$. If the B-hadrons are assumed to be unpolarized then their decays are isotropic in their rest-frames and this implies that the mean impact parameter is given by [71]

$$\langle s \rangle = \frac{1}{2}\pi \cdot c\tau \approx 721\ \mu m \tag{8.1}$$

Therefore, even allowing for moderate boosts, we expect that the CDC and VTX should provide sufficiently sensitive measurements of the muon impact parameters that may arise from B decay.

**Beam Position Determination**

Since muon impact parameters are measured relative to the primary event vertex, we require as precise a determination of the position of this vertex as is possible. The beam $xy$ position has been calculated on a run-by-run basis [72]. The raw information for determining beam positions is collected during data taking by running a sophisticated collection of online monitoring algorithms called CD-EXAMINE. For each event CDC tracks are used to determine the primary interaction points. Tracks which have $r - \phi$ impact parameters less than 2 $cm$ and $r - z$ impact parameters less than 4 $cm$ are extrapolated into the VTX. Information on these $r - \phi$ matched VTX tracks is stored along with the $z$ position of the interaction point. At the end of each run this stored information is analyzed for the determination of beam $xy$ positions, $X_0, Y_0$, by minimizing the following quantity:

$$S = \sum_{i=1}^{tracks} ((Y_i - Y_0 - \frac{dY}{dZ} \cdot ZVTX_i)\cos(\phi_i) + (X_i - X_0 - \frac{dX}{dZ} \cdot ZVTX_i)\sin(\phi_i))^2/\sigma_{\phi_i}^2 \tag{8.2}$$

where $X_i, Y_i, \phi_i$ are the center of gravity (COG) and angle of each VTX track in the $r - \phi$ view, and $\sigma_{\phi_i}$ is the error associated with the $\phi$ measurement. The $z$

position of the vertex to which the $i^{th}$ track is associated is given by $ZVTX_i$, while $\frac{dX}{dZ}$ and $\frac{dY}{dZ}$ are the beam slopes in DØ coordinates. This minimization procedure is iterated 3 times and the beam position is stored in a run summary database. Using this procedure the resolution on the beam $xy$ position has been measured to be 60 $\mu m$.

### 8.1.2 Muon Track Selection Criteria

For a given event an initial loop is made over all existing CDC tracks. Each such track has a road in $\theta$ and $\phi$ projected into the VTX. Hits are found in sectors of the VTX that contain the projected road. These hits are assembled into track segments in each of the layers of the VTX. VTX track candidates (called ladders) are then made by linking together these track segments.

Another looping process is then made over all muons in a given event to determine whether or not they have been matched up with a CDC track. If the muon has a CDC match, then a check is made for a matching VTX track. We pause for a moment to explain the CDC-VTX matching criteria. Denote by $X_{cdc}, Y_{cdc}, X_{vtx}, Y_{vtx}$ the $x$ and $y$ coordinates of the centers of gravity of the $x-y$ projections of the CDC and VTX tracks under consideration. Define the angle $\phi_{cog}$ by $\phi_{cog} = \arctan(Y_{cdc} - Y_{vtx}, X_{cdc} - X_{vtx})$. Next define the following differences: $\Delta\phi_{cdc} = \phi_{cdc} - \phi_{cog}$ and $\Delta\phi_{vtx} = \phi_{vtx} - \phi_{cog}$. Then the a CDC-VTX match is said to occur when $(\Delta\phi_{cdc})^2 + (\Delta\phi_{vtx})^2 < 5 \times 10^{-5}$. Once a CDC-VTX match has been established for a muon, a final combined 3-d fit is made by using the track parameters for the matching CDC and VTX tracks.

In order to have sufficient statistics we have decided for this analysis to use both the pre-shutdown and post-shutdown data. Furthermore we no longer impose the MU-2-HIGH trigger requirement, that is, we accept all triggers. Fig.8.5 shows the mass distribution obtained for CDC and CDC-VTX matched opposite sign dimuons. By examining these two plots we have noticed the interesting fact that the CDC-VTX match requirement seems to have significantly supressed the lowmass dimuon background.

### 8.1.3 Parametrizations of Muon Impact Parameters

Before looking at the distributions of muon impact parameters, we must consider some mathematical preliminaries. These serve to motivate the form chosen to parametrize impact parameter distributions [73].

In a decaying particle's rest frame let $t$ denote a measured interval of proper time before the decay of the particle whose lifetime is $\tau$. If $N$ denotes the number of particles remaining after time $t$, while $N_0$ denotes the number initially present then we have that

$$N = N_0 \exp(-t/\tau) \tag{8.3}$$

Now let $f(t)$ denote a normalized exponential distribution and $g(t)$ denote a normalized gaussian distribution, that is

$$f(t) = \frac{1}{\tau} \exp(-t/\tau) \tag{8.4}$$

and

$$g(t) = \frac{1}{\sqrt{2\pi}\sigma_t} \exp(-t^2/2\sigma_t^2) \tag{8.5}$$

We define a Convolution PDF (probability density function) by

$$C(\tau, t, \sigma_t) = \int_0^\infty f(t')g(t-t')dt' = \frac{1}{2\tau} \exp\left(\frac{\sigma_t^2}{2\tau^2} - \frac{t}{\tau}\right) \cdot erfc\left(\frac{\sigma_t}{\sqrt{2}\tau} - \frac{t}{\sqrt{2}\sigma_t}\right) \tag{8.6}$$

With some re-interpretation these same expressions can be used to fit the muon impact parameter distributions. We set up the following correspondences:

$$
\begin{array}{lcr}
t & \rightarrow & s \;\; (impact\ parameter) \\
\tau & \rightarrow & \langle s \rangle \;\; (mean\ impact\ parameter) \\
\sigma_t & \rightarrow & \sigma_s \;\; (resolution\ on\ the\ impact\ parameter)
\end{array}
$$

In particular we may obtain parametrizations of the signed impact parameter distributions observed both in data and in Monte Carlo for various physics processes of interest and attempt to fit them to the following form:

$$p(1) \cdot C(\langle s \rangle, s, \sigma_s) + p(2) \cdot C(\langle -s \rangle, -s, \sigma_s) + p(3) \cdot g(s, \sigma_s) \tag{8.7}$$

where the first term above describes the decay component, the second term describes mismeasured signs and resolution tails in the negative direction, and the third term describes any prompt component that may be present. In these fits we allow $p(1), p(2), p(3)$, and $\langle s \rangle, \langle -s \rangle$, and $\sigma_s$ to vary.

We have used the form above to fit the muon impact parameters for opposite sign muons constituting a dimuon in the mass range $0-6\ GeV/c^2$. Both muons were required to have a CDC-VTX match. In this fit we allowed $p(1), p(2), p(3)$, and $\langle s \rangle, \langle -s \rangle$, and $\sigma_s$ to vary. Of immediate interest is the value of $\sigma_s$ obtained in the fit. Fig.8.6 shows the result of the fit and indicates an impact parameter resolution of $\sigma_s = 221\ \mu m$. A similar fit in the mass range $2-4.4\ GeV/c^2$ gives a value of $\sigma_s = 210\ \mu m$. Distributions of electron impact parameters in $W \rightarrow e + \nu$ indicate resolutions of $\approx 180\ \mu m$. We feel that a reasonable value to work with is $\sigma_s = 200 \pm 20\ \mu m$.

We turn now to a discussion of muon impact parameters in the Monte Carlo. The Monte Carlo samples generated have been described earlier. The impact parameters in the Monte Carlo showed near perfect resolution. Therefore, in order to resemble the data, we have smeared the muon impact parameters with a gaussian resolution function of width $200\ \mu m$. We then fit each of the smeared distributions with the functional form described above. The dimuons were required to be of opposite sign in the nominal $J/\psi$ mass range $2-4.4$ $GeV/c^2$. We further required that the dimuon $p_T$ be greater than 8 $GeV/c$ and the dimuon $|\eta|$ be less than 0.6. Both muons that comprised the dimuon were required to have a combined CDC-VTX match. The signs of the impact parameters were determined with the reference direction given by the vector sum of the momentum of the jet associated with the muons (corrected for muon energy loss expected) and the dimuon momentum, or if there was no jet associated with the muons, then simply the dimuon momentum vector. Recall that an associated jet is one within an $\eta-\phi$ cone of radius $R=0.7$ about the direction of the object under study (the muon or dimuon). Fig.8.7 shows the fitted distributions obtained in the Monte Carlo. We note the clear difference between the distributions for the two $J/\psi$ samples. The $\chi_c$-produced $J/\psi$'s are clearly prompt in nature since a simple gaussian was found to be a good description of the impact parameter distribution. By contrast, the $B$-produced $J/\psi$'s appear to be non-prompt and show an obvious decay-like tail similar to that shown for the $Q\bar{Q}$ Monte Carlo.

### 8.1.4 The Likelihood Function

For the determination of $F_b$ we have used a simultaneous maximum likelihood fit to the dimuon mass and the muon impact parameter distributions on an event by event basis. The mass parametrizations were discussed in Chapter 5. The processes that were fitted for were:

- B-produced $J/\psi$'s
- $\chi_c$-produced $J/\psi$'s

- $Q\bar{Q}$ produced dimuons

- Drell-Yan produced dimuons

The explicit form for the likelihood function was taken to be

$$\pounds = \prod_{i=1}^{nevent} (A_1 \cdot \ f_{signal} + B_1 \cdot f_{Q\bar{Q}} + B_2 \cdot f_{Drell-Yan}) \tag{8.8}$$

where

$$f_{signal} = F_b \cdot f_{J/\psi_b} + (1 - F_b) \cdot f_{J/\psi_{\chi_c}} \tag{8.9}$$

and where

$$f_{J/\psi_b} = M(M_{\mu\mu}) \cdot S(s_{\mu_1}) \cdot S(s_{\mu_2}) \tag{8.10}$$

and similarly for the other processes. Here $M$ and $S$ represent the process-specific parametrizations of the mass and impact parameter distributions respectively. Each of these parametrized distributions has been normalized to unity for use in the fit. As in the previous chapter, we have taken into account the constraint that the sum of the number of dimuons for each process add up to the total number of dimuons observed in the data. Therefore, for the normalizing coefficients $A_1, B_1, B_2$, we have written

$$\begin{aligned} A_1 &= \xi_1 \\ B_1 &= (1-\xi_1)\xi_2 \\ B_2 &= (1-\xi_1)(1-\xi_2) \end{aligned} \tag{8.11}$$

In minimizing the negative log likelihood function we have taken the primary fit parameters to be $F_b, \xi_1, \xi_2$.

### 8.1.5 Determination of $F_b$

Ultimately we are interested in deriving a $b$-quark cross section from the $J/\psi$ data. To this end it is necessarry to determine the fraction of b-produced $J/\psi$'s, that is, $F_b$. We have performed a maximum likelihood fit to the opposite sign dimuon data in the mass range $2 - 4.4\ GeV/c^2$. Impact parameters were fitted in the range $-0.08\ cm$ to $0.16\ cm$. As stated earlier, we further required that the dimuon $p_T$ be greater than $8\ GeV/c$ and the dimuon $|\eta|$ be less than 0.6. Both muons that comprised the dimuon were required to have a combined CDC-VTX match. The signs of the impact parameters were determined with the reference direction given by the vector sum of the momentum of the jet associated with the muons (corrected for muon energy loss expected) and the dimuon momentum, or if there was no jet associated with the muons, then simply the dimuon momentum vector. Fig.8.8 shows the result of the simultaneous mass and impact parameter fit. We observe a $J/\psi$ signal of $143 \pm 17$ events over a background of $120 \pm 15$ $Q\bar{Q}$ events and $8 \pm 4$ Drell-Yan events. The fitted value of the $J/\psi$ b-fraction is

$$F_b = 0.35 \pm 0.09\ (stat) \pm 0.10\ (sys) \tag{8.12}$$

Fig.8.9 shows the behaviour of the negative log Likelihood function in the neighborhood of its minimum. The function is plotted versus $F_b$ and shows a clear minimum at $F_b = 0.35$. Also shown are the 1-sigma points indicating the range of statistical error. We should note here that we have actually used -2 times the log likelihood so that the 1-sigma points are obtained by noting where the function changes by 1 unit (rather than the usual change of 0.5 units). We estimate the overall CDC-VTX match efficiency per dimuon to be 0.79 (from the CDC match) times 0.26 (from the VTX match), or approximately 21%.

## 8.2 The $b$-Quark Cross Section

By using the $J/\psi$ data and the fraction $F_b$ of $J/\psi$'s produced from the weak decay of B-mesons, we may work backwards and calculate the integrated $b$-quark cross section above a certain minimum value $p_{b\ min}^{T}$.

The $b$-quark cross section may be estimated from the $J/\psi$ data sample by utilizing the following relation [74]:

$$\sigma(p\bar{p} \to b+X, p_T^b > p_{b\ min}^T, |y_b| < 1) = \frac{F_b \cdot \sigma(p\bar{p} \to J/\psi + X, p_T^{J/\psi} > c)}{2 \cdot Br(b \to J/\psi + X) \cdot Br(J/\psi \to \mu^+\mu^-) \cdot A_c} \tag{8.13}$$

The quantity $p_{b\ min}^{T}$ is that value of $p_b^T$ for which 90% of the accepted $b$'s satisfy $p_b^T > p_{b\ min}^T$. The factor of 2 in the denominator arises because the $J/\psi$ may have been produced by either the $b$ or $\bar{b}$ quark. Here $A_c$ represents the acceptance for $b$-quarks that give rise to $J/\psi$'s satisfying the kinematic cut $p_T^{J/\psi} > c$. An expression for $A_c$ can be derived from Monte Carlo and is given by

$$A_c = \frac{\sigma^{mc}(p\bar{p} \to b + X, |y_b| < 1, p_T^{J/\psi} > c)}{\sigma^{mc}(p\bar{p} \to b + X, |y_b| < 1)} \tag{8.14}$$

We have determined that for $p_T^{J/\psi} > 8\ GeV/c$, we have $A_c = 0.20 \pm 0.04\ (sys)$. This determination is based upon use of the Peterson fragmentation function in conjunction with MNR $b$-quark $p_T$ spectra. We have assumed only two-body decays of B-hadrons into $J/\psi$ and $K$ and $K^*$ mesons. Fig.8.10 shows the fragmentation and hadronization characteristics calculated for the $b$-quark using MRSDO structure functions.

In Fig.8.11 we show the appropriate $b$-quark $p_T$ spectra both for all $b$ decays and for $b$ decays that produce $J/\psi$'s with $p_T^{J/\psi} > 8\ GeV/c$. If we substitute the

| Minimum $p_T^{J/\psi}$ | $p_{b\ min}^T$ | $A_c$ |
|---|---|---|
| $8\ GeV/c$ | $9.90\ GeV/c$ | $0.20 \pm 0.04\ (sys)$ |
| $10\ GeV/c$ | $12.36\ GeV/c$ | $0.17 \pm 0.05\ (sys)$ |

Table 8.2: $b$-quark acceptances for different cuts on the Minimum value of $p_T^{J/\psi}$

appropriate numbers into the cross section equation above we have that

$$\begin{aligned} \sigma(p\bar{p} \to b + X, p_T^b > p_{b\ min}^T, |y_b| < 1) &= 2.25 \pm 0.60\ (stat) \pm 1.01\ (sys)\ \mu b \\ & \quad for\ \ p_{b\ min}^T = 9.90\ GeV/c \end{aligned} \tag{8.15}$$

Fig.8.12 shows a plot of this value on an integrated $b$-quark $p_T$ spectrum based upon MRSDO structure functions. Examination of the data shows that the behaviour of $F_b$ is consistent with having the constant value of 0.36 for $p_T^{J/\psi} > 8\ GeV/c$ [75]. Therefore we have generated one more $b$-quark integrated cross section point for $p_T^{J/\psi} > 10\ GeV/c$. The corresponding value of the $b$-quark acceptance and $p_{b\ min}^T$ is: $A_c = 0.17 \pm 0.05\ (sys)$ and $p_{b\ min}^T = 12.36\ GeV/c$. Table 8.2 summarizes our results. The systematic errors on $A_c$ were estimated by varying the structure functions used and also by varying the value of $\epsilon$ appearing in the Peterson fragmentation function. The single muon results shown in Fig.8.12 are described in ref.[55].

## 8.3 $\chi_c$ Production of $J/\psi$ Mesons

Although the production of $J/\psi$'s via the radiative decay of $\chi_c$ states is the subject of another thesis [76], we have decided for completenes' sake to mention some of the highlights found from the analysis of candidate $\chi_c \rightarrow J/\psi + \gamma$ events. In the following discussion we note that the full statistics for pre and post-shutdown data (all triggers with integrated luminosity $\approx 11.4\ pb^{-1}$) was used.

The most compelling evidence for the detection of $\chi_c$ states at the DØ collider is the mass difference spectrum presented in Fig.8.13. The mass difference $\Delta M = M_{\mu^+\mu^-\gamma} - M_{\mu^+\mu^-}$ gives the characteristic energy of the decay photon in the rest frame of the decaying $\chi_c$ (neglecting the kinetic energy of the $J/\psi$). This energy is approximately 0.4 $GeV/c^2$. The figure shows a clear $\chi_c$ signal at $\Delta M =$ 0.43 $GeV/c^2$, where the width of the peak is approximately 0.063 $GeV/c^2$. The width is determined by the photon energy resolution which is given by $15\%/\sqrt{E}$. Since the photon energy in the Lab is generally on the order of $E_\gamma = 1\ GeV/c^2$, we expect an energy resolution of approximately $0.15 \cdot \Delta M = 0.064\ GeV/c^2$. This resolution is insufficient to distinguish the separate $\chi_{cj}, j = 0, 1, 2$ states: all results therefore pertain to inclusive $\chi_c$ production. A fit to the data shows that the number of $\chi_c$ events is $N_{\chi_c} = 66 \pm 15\ (stat) \pm 5\ (sys)$.

The muon and dimuon selection criteria were essentially identical to those discussed earlier in Chapters 5 and 6 for the inclusive $J/\psi$ cross section, except that, as stated above, no specific trigger requirement was imposed, and the full statistics of Run 1A was used. The fitted number of $J/\psi$ events is $N_{J/\psi} = 722 \pm 52\ (stat) \pm 72\ (sys)$.

We now discuss the photon selection criteria. The standard DØ threshold on the energy of electromagnetic clusters is 1.5 $GeV$. With the threshold set this high only 22% of the photons from $\chi_c$ decays would be reconstructed. Therefore, the photon energy threshold was lowered to 0.8 $GeV$. The entire sample of Run 1A events with dimuons whose invariant masses were in the range $2-4$ $GeV/c^2$ was re-reconstructed. An offline photon energy cut of 1.0 $GeV$ was then imposed on photon candidates. The acceptance for photons with $E_\gamma > 1$ $GeV$ was calculated to be $60 \pm 0.76\%$. The reconstruction efficiency for such photons was estimated to average $50.0 \pm 2.4\%$. Thus the overall efficiency for the detection of photons originating from radiative $\chi_c$ decays was determined to be $30.0 \pm 1.5\%$. Fig.8.14 shows the efficiency for photon reconstruction as a function of $E_\gamma$.

From the information presented above it is possible to estimate $F_\chi$, that is, the fraction of $J/\psi$ events that originate from $\chi_c$ radiative decays. This fraction is defined as follows:

$$F_\chi = \frac{N_{\chi_c}}{N_{J/\psi} \cdot \epsilon_\gamma} \tag{8.16}$$

where $N_{\chi_c}$ is the number of reconstructed $\chi_c$ events, $N_{J/\psi}$ is the number of $J/\psi$'s, and $\epsilon_\gamma$ is the combined acceptance times efficiency for photon reconstruction from $\chi_c$ decay. Substituting the numbers above yields

$$F_\chi = \frac{N_{\chi_c}}{N_{J/\psi} \cdot \epsilon_\gamma} = 30 \pm 7 \pm^{4.2}_{5.6} \ \% \tag{8.17}$$

A study of the isolation characteristics of $\chi_c$ events has also been carried out. The isolation criterion chosen was the absence of any jet within a $\eta-\phi$ cone defined by $R < 0.7$ around the dimuon direction. Using this requirement the fitted number of isolated $\chi_c$ events was determined to be $N_{isol\chi_c} = 40 \pm 12(stat) \pm 4(sys)$. By assuming that all isolated $\chi_c$ events come from direct charmonium production the relative contribution of this mechanism to overall $\chi_c$ production was estimated to

| Process | Branching Ratio |
|---|---|
| $B \rightarrow \psi(2S) + X$ | 0.46% |
| $B \rightarrow \chi_{c1} + X$ | 1.1% |
| $B \rightarrow J/\psi + X$ | 1.3% |
| $\psi(2S) \rightarrow J/\psi + X$ | 0.57 |
| $\chi_{c1} \rightarrow J/\psi + X$ | 0.27 |

Table 8.3: Branching ratios for B hadrons into charmonium.

be

$$F_{direct} = \frac{N_{isol\chi_c}}{N_{\chi_c} \cdot \epsilon_{isol}} = 73 \pm 24 \pm 8.8\ \% \tag{8.18}$$

where $\epsilon_{isol} = 83 \pm 4\%$ is the acceptance for this isolation cut.

## 8.4 Discussion

In this chapter we have made an attempt to disentangle the various mechanisms that contribute to inclusive $J/\psi$ production. We have calculated that appprox-imately 35% of all $J/\psi$'s appear to originate from the weak decay of B mesons. Similarly, approximately 30% of all $J/\psi$'s appear to come from the radiative decay of $\chi_c$ charmonium states. Furthermore, in the previous chapter we have established that $F_{non-iso}$ is approximately 57%, with $F_{iso}$ being about 43%. Based on this information let us now attempt to put forward our best guesses as to the detailed breakdown of the various mechanisms that are believed to be operative in $J/\psi$ production.

Consider first the categorization of the B-produced mechanisms. To do this we calculate the following estimated contributions based on known branching ratios involving B hadrons and the $J/\psi$.

$$
\begin{aligned}
B \to \psi(2S) \to J/\psi: \quad & \tfrac{0.46\% \times 0.57}{1.3\%} && = 0.20 \Rightarrow 0.20 \times 0.35 = 0.07 \\
B \to \chi_{c1} \to J/\psi: \quad & \tfrac{1.1\% \times 0.27}{1.3\%} && = 0.23 \Rightarrow 0.23 \times 0.35 = 0.08 \\
B \to J/\psi: \quad & 0.35 - 0.07 - 0.08 && = 0.20
\end{aligned}
$$

where we have used the branching ratios shown in Table 8.3. We have assumed that B production is non-isolated in nature and therefore there remains an unexplained fraction of $0.57 - 0.35 = 0.22$ non-isolated and prompt $J/\psi$ production. We appear to be describing a class of prompt, non-isolated, directly-produced $J/\psi$ states. This could herald the appearance of the fragmentation mechanism at work, however fragmentation is thought to be dominated by $\chi_c$ production.

With regard to isolated $J/\psi$ production we note that we should have a fraction of $0.30 - 0.08 = 0.22$ isolated $J/\psi$ events directly from $\chi_c$ and **not** through B. This compares well with the estimate of isolated $\chi_c$ production discussed in the previous section. There it was determined that the CPM mechanism for $\chi_c$ production, which we have agreed to classify as isolated, contributes a fraction equal to $F_{direct} \cdot F_{\chi} = 0.73 \times 0.30 = 0.22$. Assuming that $\chi_c$ production is exhausted by the CPM and BPM mechanisms this further implies a non-isolated, non-prompt contribution of 0.08 which again agrees well with the 8% estimate derived above. This leaves an unexplained fraction of $0.43 - 0.22 = 0.21$ isolated, directly-produced, and prompt $J/\psi$ events. Perhaps the classical CPM mechanism for direct $J/\psi$ production has been underestimated by the theorists.

Let us denote the unexplained non-isolated, prompt, directly produced process by $X_F \to J/\psi$. Similarly, let us denote the isolated, prompt, directly produced

| | ISOLATED | NON-ISOLATED |
|---|---|---|
| PROMPT | $X_D \to J/\psi$ $0.21 \pm 0.15$<br>$\chi_c \to J/\psi$ $0.22 \pm 0.09$ | $X_F \to J/\psi$ $0.22 \pm 0.18$ |
| NON-PROMPT | | $B \to J/\psi$ $0.20 \pm 0.14$<br>$B \to \chi_c \to J/\psi$ $0.08 \pm 0.03$<br>$B \to \psi(2S) \to J/\psi$ $0.07 \pm 0.03$ |

Table 8.4: Classification of the various mechanisms for $J/\psi$ production.

process by $X_D \to J/\psi$. Then we may summarize our results in Table 8.4.

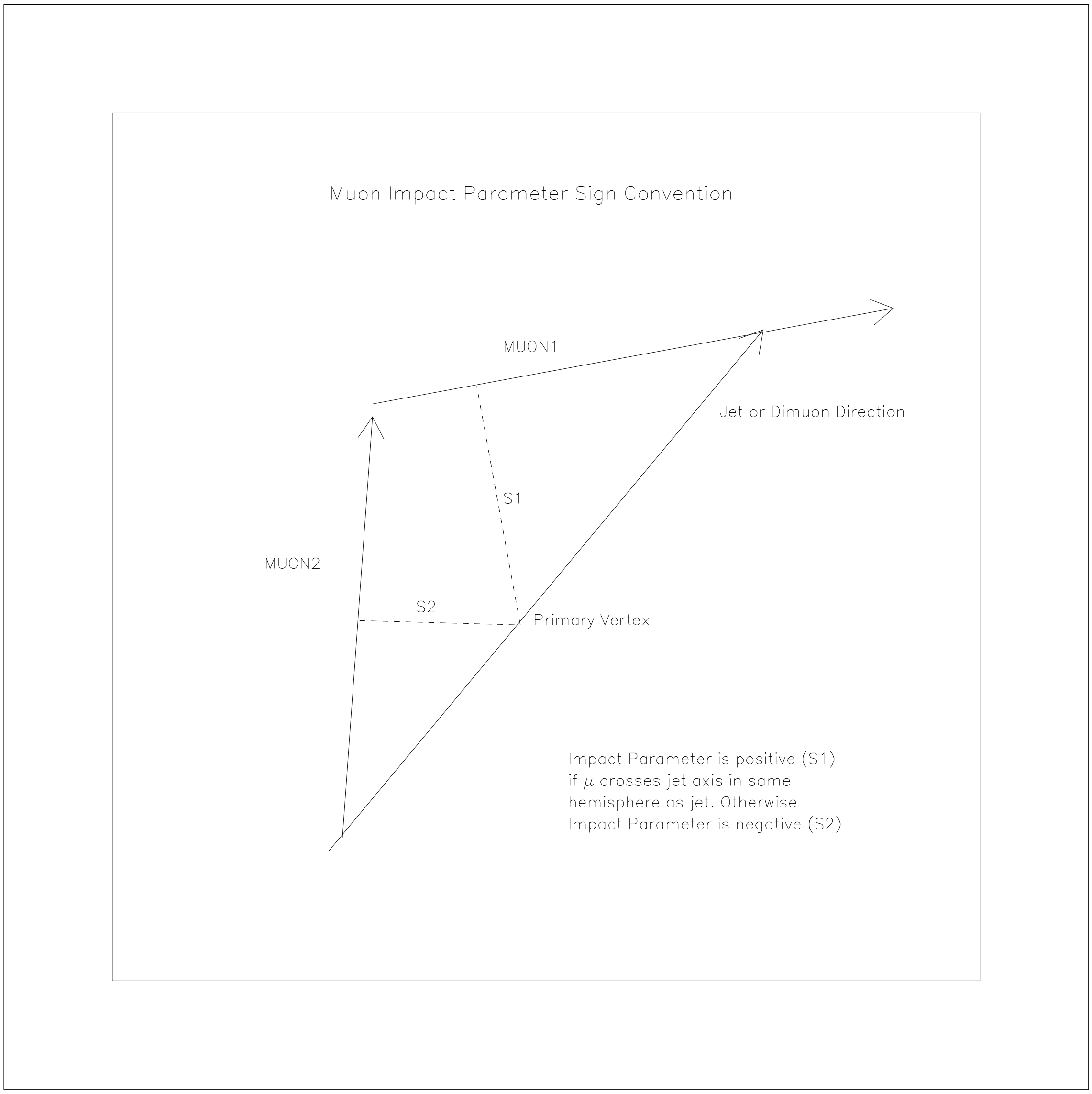


Figure 8.1: Muon Impact Parameter Sign Convention

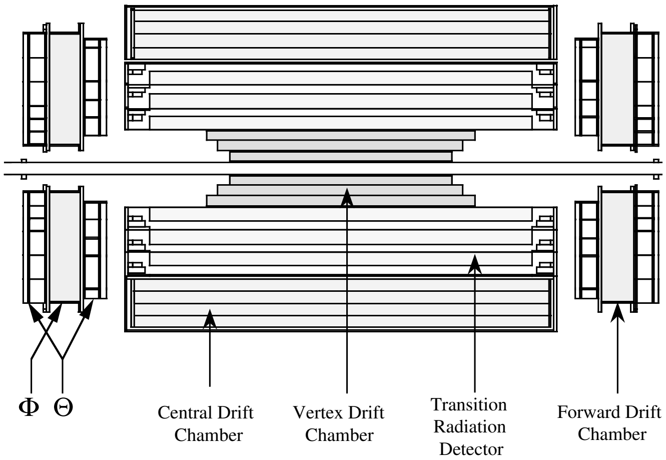


Figure 8.2: A cross section of the DØ central detectors

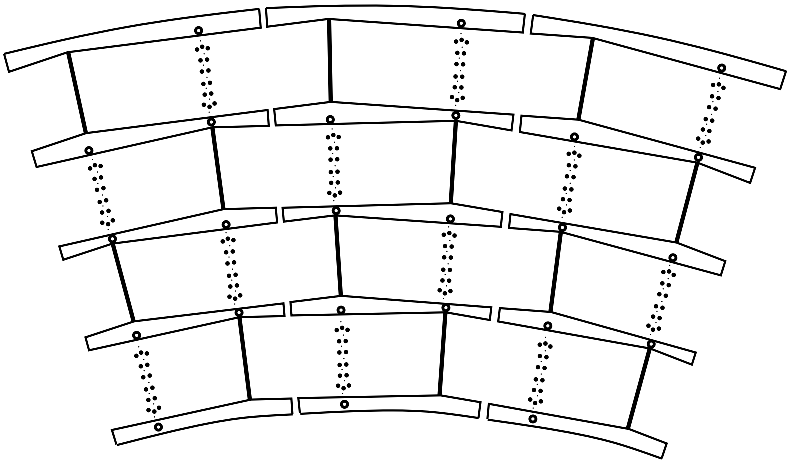

Figure 8.3: End-view of the central drift chamber, shown are the 7 sense wires per cell as well as the delay-lines embedded in the walls of the cells.

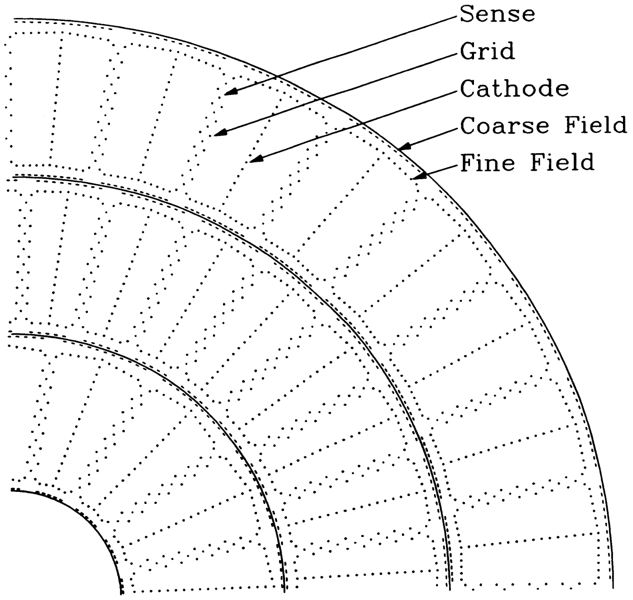


Figure 8.4: End view of one quadrant of the vertex chamber

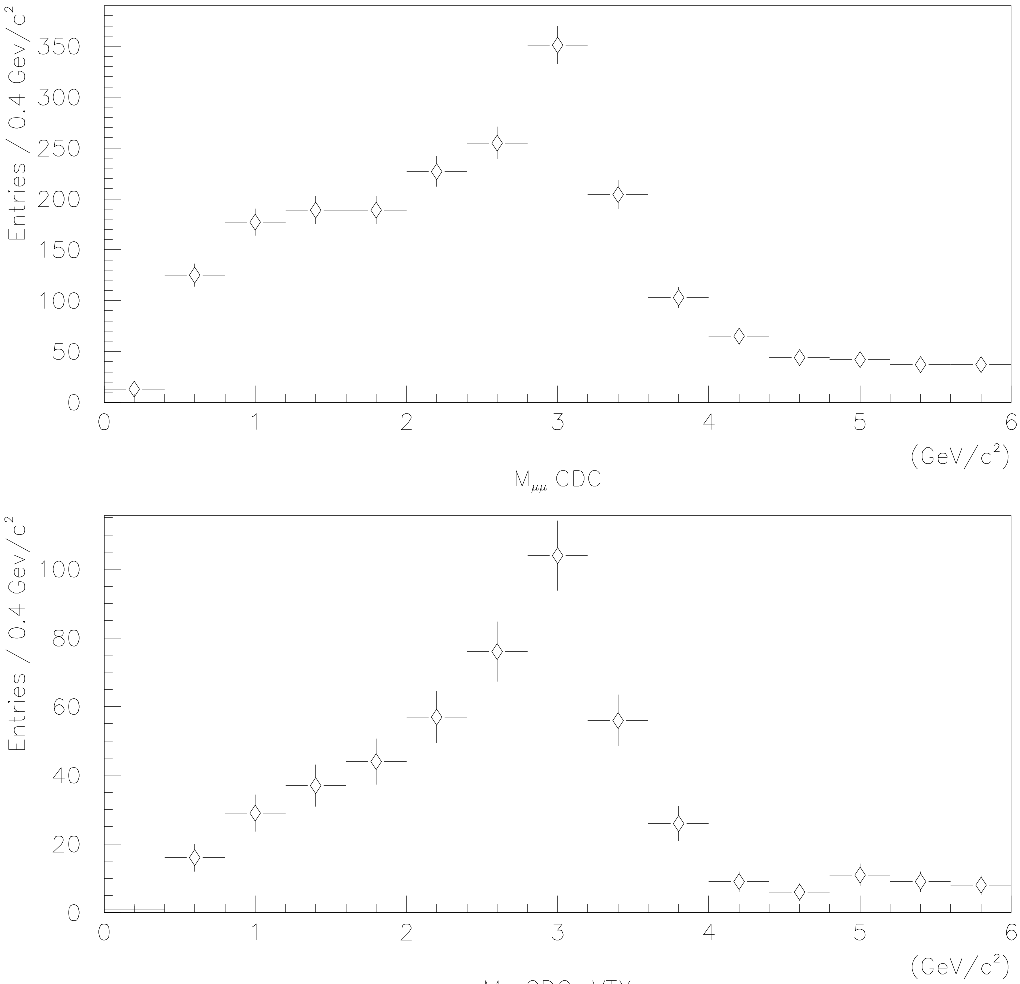


Figure 8.5: Oppsosite sign dimuon mass spectrum for: (top) CDC matched muons and (bottom) CDC-VTX matched muons

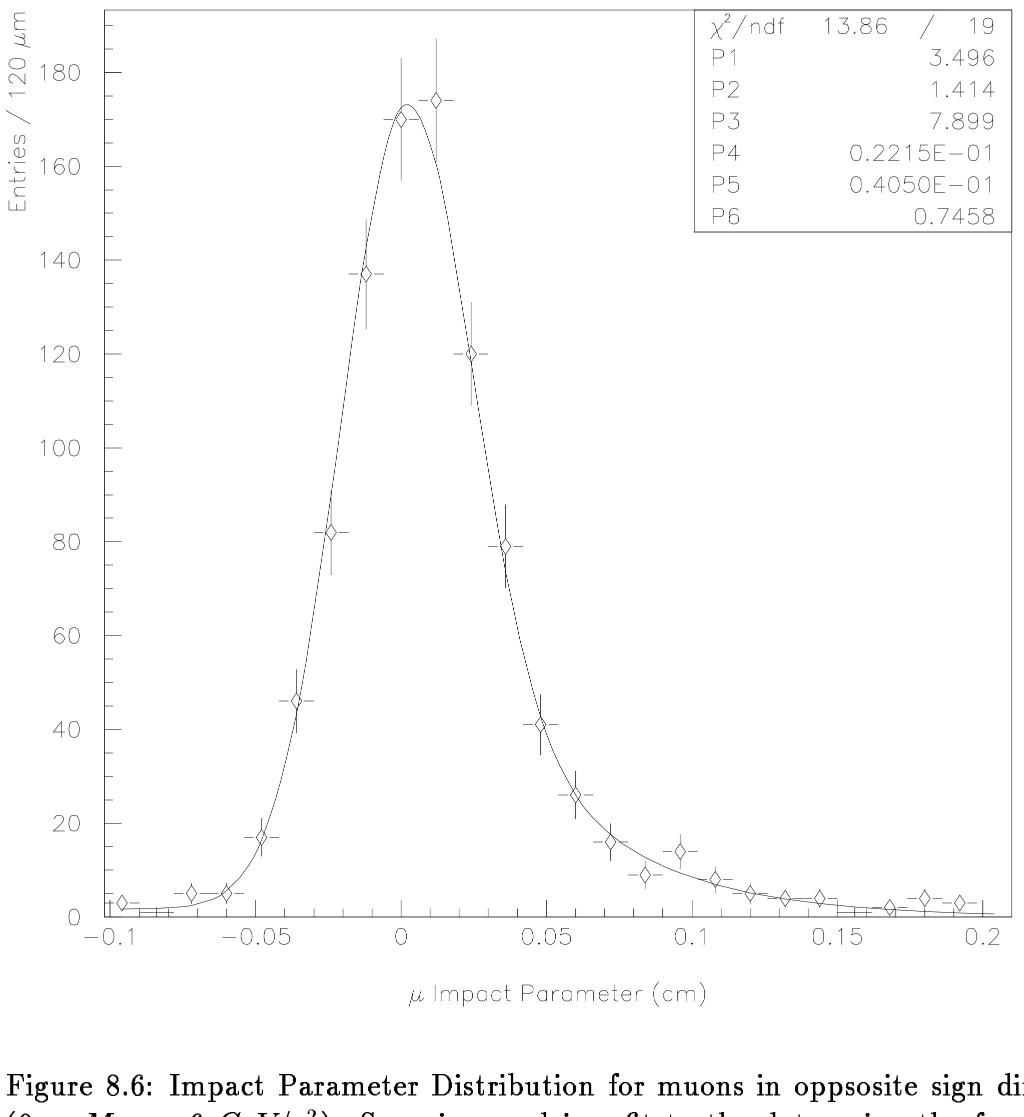


Figure 8.6: Impact Parameter Distribution for muons in oppsosite sign dimuons ($0 < M_{\mu\mu} < 6\ GeV/c^2$). Superimposed is a fit to the data using the functional form discussed in the text.

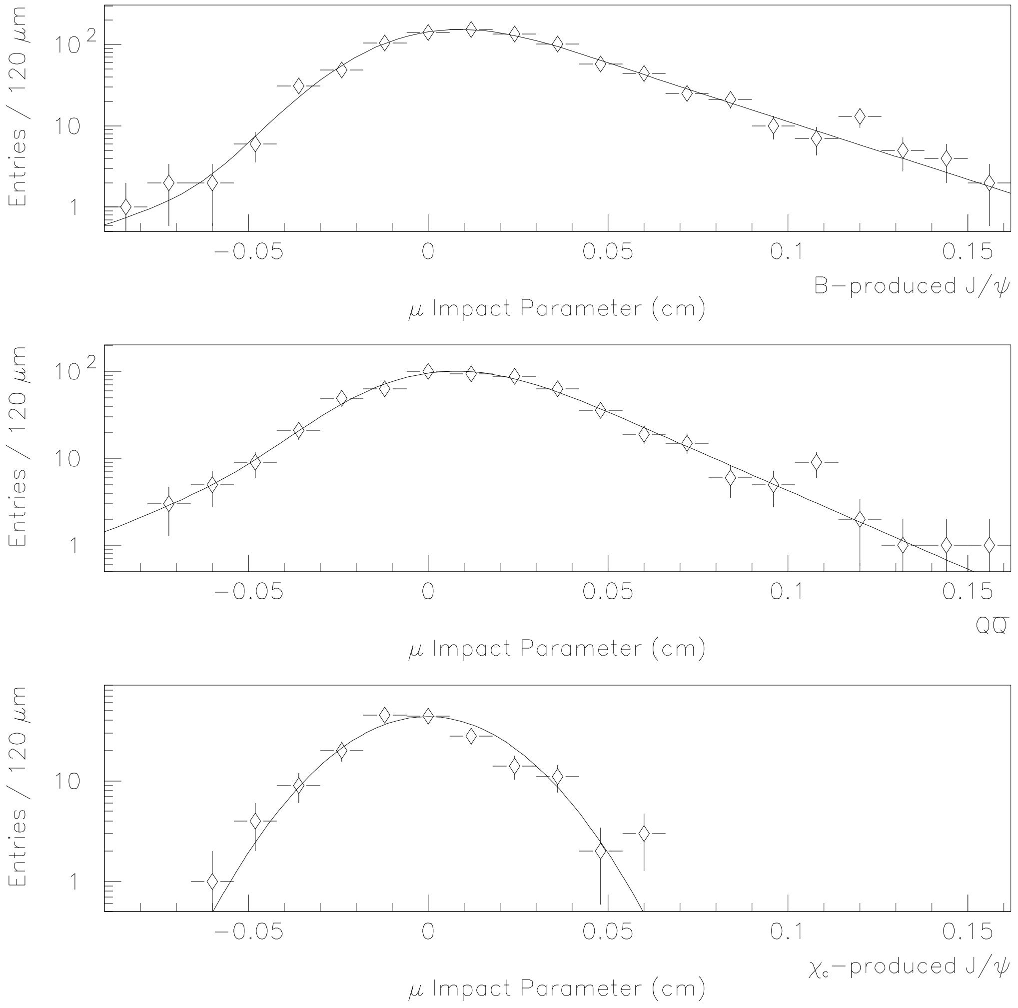


Figure 8.7: Monte Carlo Impact Parameter Distributions for muons in oppsosite sign dimuons ($0 < M_{\mu\mu} < 6\ GeV/c^2$). Superimposed are fits to the data using the functional form discussed in the text.

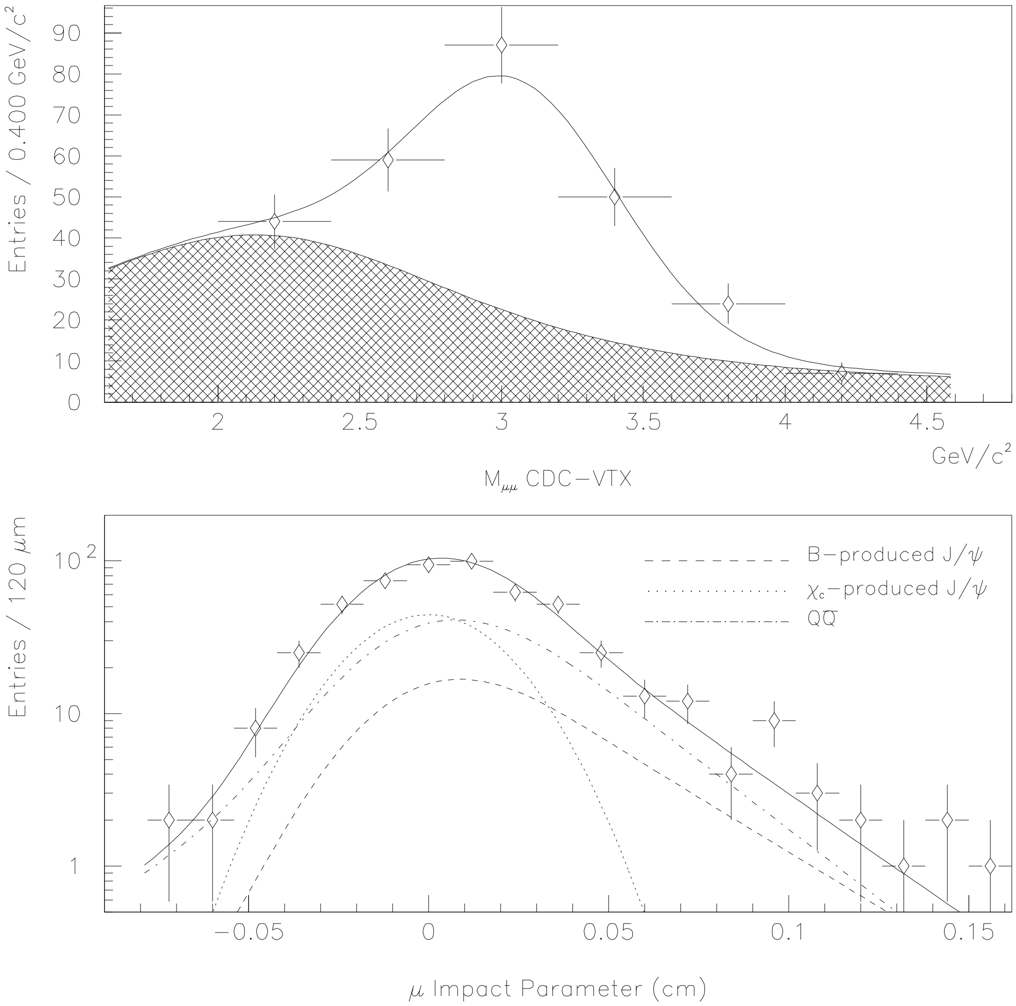


Figure 8.8: Observed mass and impact parameter distributions for all triggers. Superimposed are the results of the simultaneous Maximum Likelihood fit to the mass and impact parameter data. The lower plot shows the fitted B-produced $J/\psi$ contribution, the $\chi_c$-produced $J/\psi$ contribution and the $Q\bar{Q}$ background.

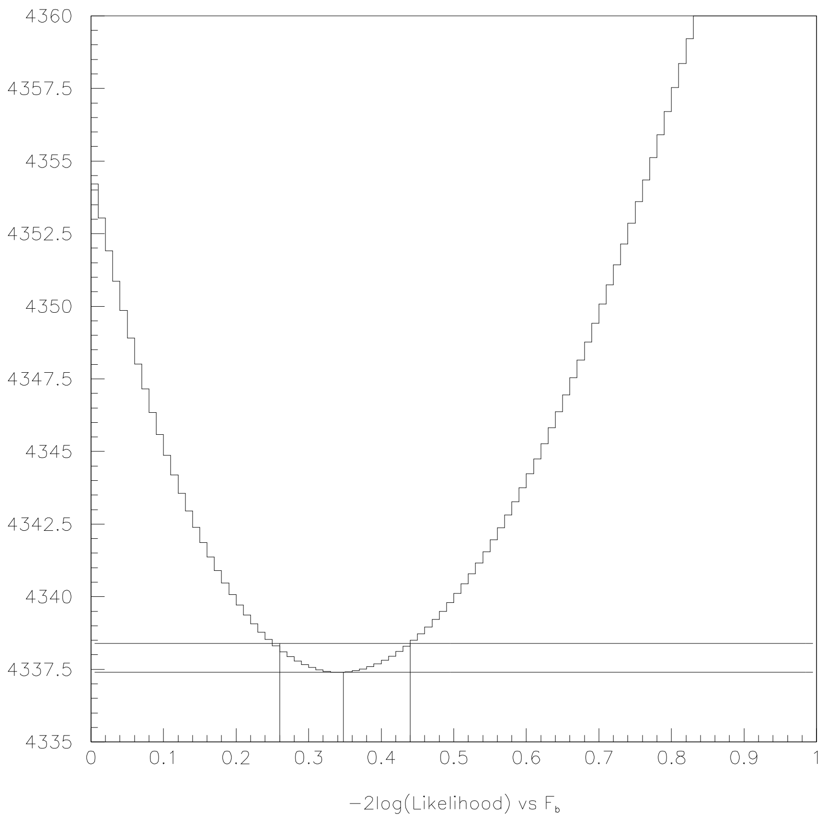


Figure 8.9: - log Likelihood vs Fraction $F_b$ of b-produced $J/\psi$'s

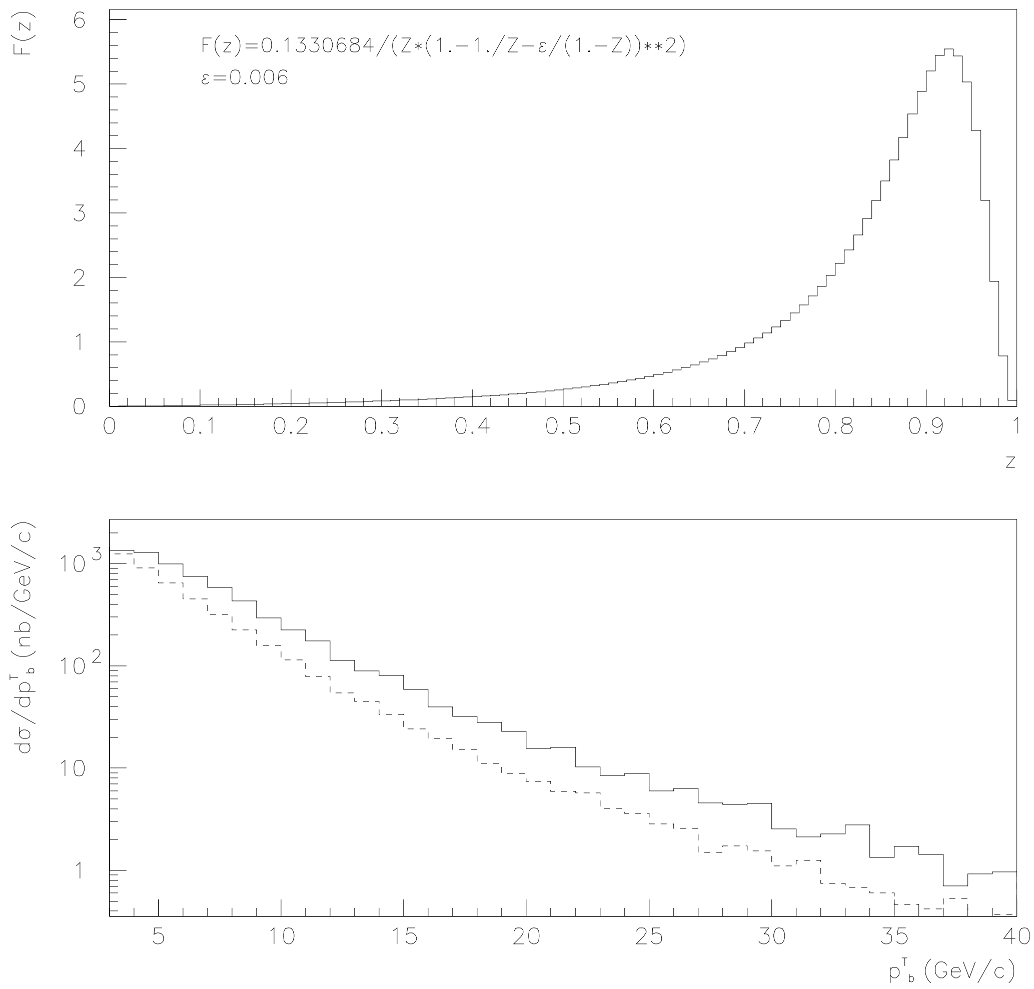


Figure 8.10: $b$-quark Fragmentation: (upper) Peterson Fragmentation Function, (lower) $b$-quark and B-hadron $d\sigma/dp_T$ spectra.

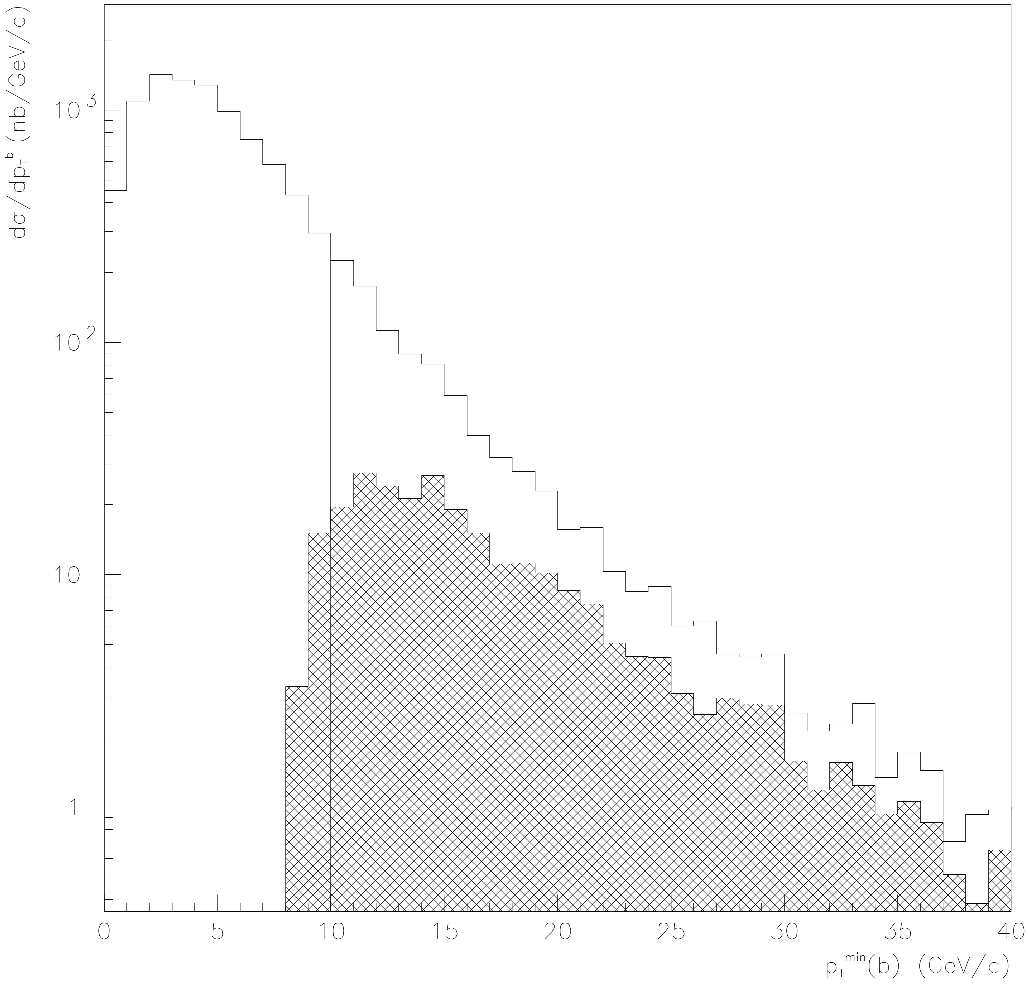


Figure 8.11: $b$-quark $p_T$ spectra for all $b$'s and $b$'s satisfying $p_T^{J/\psi} > 8\ GeV/c$

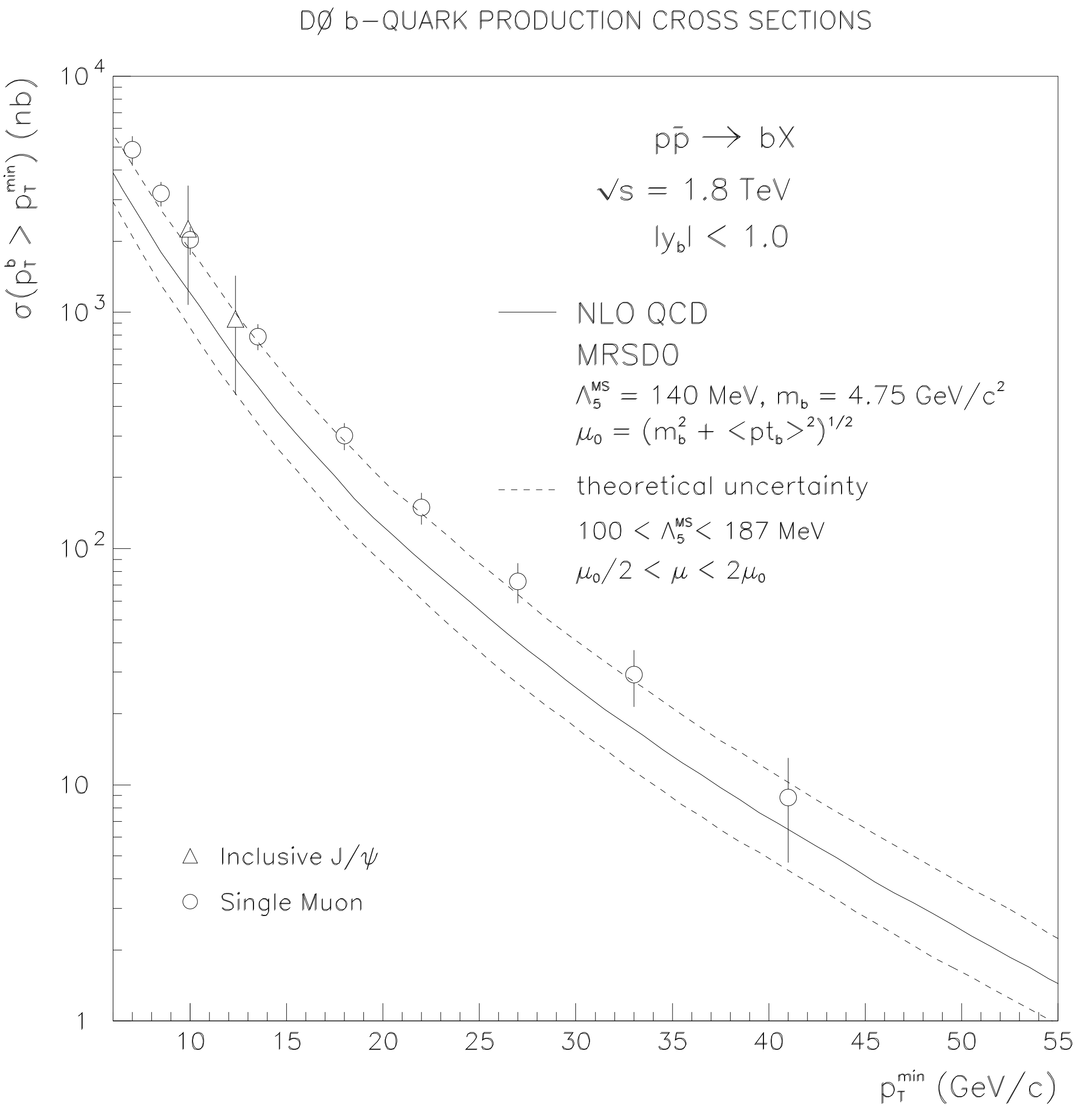


**Figure 8.12: Integrated $b$-quark $p_T$ spectrum vs $p^T_{b\ min}$**

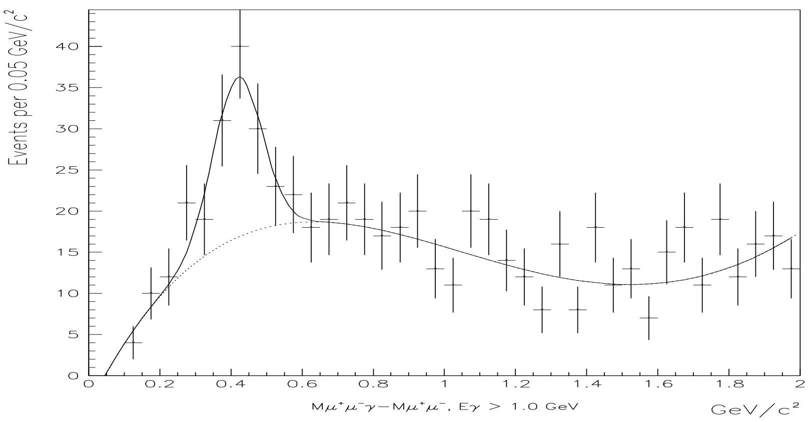


Figure 8.13: Mass difference spectrum ($\Delta M = M_{\mu^+\mu^-\gamma} - M_{\mu^+\mu^-}$) for candidate $\chi_c$ events.

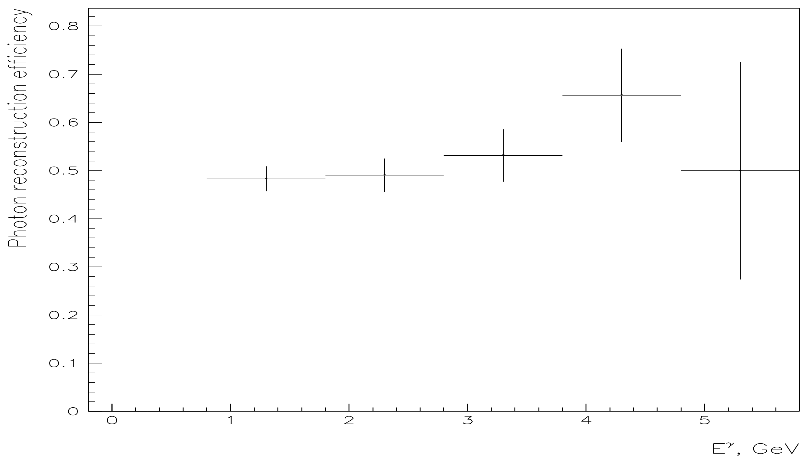


Figure 8.14: Efficiency for photon reconstruction as a function of $E_\gamma$ for candidate $\chi_c$ events.

# Chapter 9

# Conclusions

We have analyzed $6.6 \pm 0.8\ pb^{-1}$ of data collected under the MU-2-HIGH dimuon trigger at DØ. From this data we have extracted the inclusive $J/\psi$ differential cross section for the kinematic region $p_T(J/\psi) > 8\ GeV/c$ and $|\eta(J/\psi)| < 0.6$. The cross section results are in very good agreement with a similar analysis done by the CDF collaboration in the same kinematic region. The agreement with theoretical calculations for inclusive $J/\psi$ production is poor for $p_T(J/\psi) < 11\ GeV/c$, theory being low by about a factor of 2. Above 11 $GeV/c$ the agreement is better, but in general the data appears to be more steeply sloped than the theoretical predictions. The best agreement is obtained for low values of the factorization-renormalization scale, namely $\mu = \frac{1}{4} \cdot \mu_0$, where $\mu_0 = \sqrt{\langle p_T \rangle^2 + M^2}$ is the transverse mass of the charmonium system. The integrated $J/\psi$ production cross section has been calculated to be $2.00 \pm 0.17(stat) \pm 0.50(sys)\ nb$ for $p_T(J/\psi) > 8\ GeV/c$ and $|\eta(J/\psi)| < 0.6$.

It has been one of the goals of this thesis to attempt to determine the relative contributions of at least some of the different mechanisms that are currently thought to contribute to overall $J/\psi$ production. Towards this end we have analyzed a larger dimuon data set of $11.4 \pm 1.4\ pb^{-1}$, collected for all triggers, in attempt to estimate the fraction $F_b$ of B-produced $J/\psi$ s. By examining muon impact parameters for the $J/\psi$ we have calculated that $F_b = 0.35 \pm 0.09(stat) \pm 0.10(sys)$ for a mean value of $J/\psi$ $p_T$ given by $\langle p_T(J/\psi)\rangle = 11.73$ $GeV/c$. Again this value of $F_b$ agrees well with similar results obtained by CDF. Based upon the cross section for inclusive $J/\psi$ production and the value of $F_b$ we have been able to compute a $b$-quark cross section integrated over $p_T(b)$ above a minimum value of $p_T^{min}(b) = 9.9$ $GeV/c$. We obtain a value of $\sigma(p_T^b > p_T^{min}) = 2.25 \pm 0.60(stat) \pm 1.01(sys)$ $\mu b$. This value is consistent with similar observations based on inclusive single muon studies. In addition these observations appear to be in good agreement with NLO theory calculations of b-quark production. It has not been necessarry to stretch the range of factorization-renormalization scales as far as they have been for the $J/\psi$ itself. A value of $\mu = \frac{1}{2} \cdot \mu_0$ appears to be sufficient to bring theory into line with the experimental observations collected at the Tevatron's two collider detectors.

The production of $J/\psi$ s via the decay of $\chi_c$ states has also been touched upon and we have quoted the results of a study which give a value of $F_\chi = 30 \pm 7(stat) \pm^{4.2}_{5.6}$ % for the fraction of $J/\psi$ events that originate from $\chi_c$ radiative decays.

The isolation properties of the $J/\psi$ have been explored and we have estimated that the fraction of $J/\psi$ events which appear to be non-isolated is $F_{non-iso} = 0.57 \pm 0.12$, while conversely the fraction of isolated events has been observed to be $F_{iso} = 0.43 \pm 0.12$.

The numerous different mechanisms involved in $J/\psi$ production has prompted us to attempt to organize our observations in terms of a simple classification scheme that is based upon whether an event is prompt or not, and whether the event is isolated or not. We have implemented the simplifying assumption that B-produced $J/\psi$ events are non-isolated and that they are further non-prompt in nature. Utilizing this classification scheme we have concluded that $49 \pm 37\%$ of the prompt and isolated $J/\psi$ events are unexplained by current theories of $J/\psi$ production. Similarly, we have concluded that $38 \pm 32\%$ of the prompt and non-isolated events may likewise be unexplainable in terms of present theoretical models (although the fragmentation mechanism may hold the possibility of being sufficiently refined to account for this apparent discrepancy). In total this amounts to approximately $43 \pm 23\%$ of all $J/\psi$ production that appears to be insufficiently described by theory (we note that all these problematic events are of the prompt variety). Hopefully these matters will be cleared up in the near future. Part of this will depend on $J/\psi$ sample sizes that have a much greater statistical significance than we have been able to achieve in Run 1A. As this thesis is being written Run 1B is already well underway and the DØ collaboration has more than tripled the $J/\psi$ sample size as compared with Run 1A. Also the SAMUS detector has begun to collect very pretty and clear evidence of forward produced $J/\psi$ and $\Upsilon$ events. At the moment however it would appear that the theorists are far from finished in dealing with the "well known" $J/\psi$.

# Bibliography


[1] E. Abers and B. W. Lee, Phys.Rep.C, 9, 1 (1973)

[2] C. N. Yang and R. L. Mills, Phys.Rev., 96, 191 (1954)

[3] S. Gashow, Nucl. Phys., 22, 579 (1961); S. Weinberg, Phys. Lett., 12, 132 (1967) A. Salam, "Elementary Particle Physics", ed. N. Svartholm, 367 (1968)

[4] W. Marciano and H. Pagels, Phys.Rep.C, 36, 137 (1978)

[5] S. Glashow, J. Iliopoulos, L. Maiani, Phys. Rev. D, 2, 1285 (1970)

[6] J. Goldstone and S. Weinberg, Phys.Rev., 127, 965 (1962)

[7] P. W. Higgs, Phys.Lett., 12, 132 (1964); Phys.Rev.Lett., 13, 508 (1964)

[8] P. Langacker, Phys.Rep.C, 72, 185 (1981)

[9] J. J. Aubert et. al., Phys. Rev. Lett., 33, 1404 (1974)

[10] J. E. Augustin et. al., Phys. Rev. Lett., 33, 1406 (1974)

[11] M. Aguilar-Benitez et al., Phys.Rev.D, Particles and Fields, 50, "Review of Particle Properties", August 1994

[12] G. Miller et. al., Phys. Rev., D5, 528 (1972)

[13] R. P. Feynman, Phys. Rev. Lett., 23, 1415 (1969); "Photon-Hadron Interactions", W. A. Benjamin, N. Y., 1972

[14] G. Altarelli and G. Parisi, Nucl.Phys., B126, 298 (1977)

[15] D. Gross and F. Wilczek, Phys. Rev. Lett., 30, 1343 (1973); H. Politzer, Phys. Rev. Lett., 30, 1346 (1973)

[16] R. Baier and R. Rückl, Z. Phys. C, 19, 251 (1983)

[17] B. Humpert, Phys.Lett.B, 184, 105 (1987)

[18] R. Gastmans, W. Troost, and T. Wu, Phys.Lett.B, 184, 257 (1987)

[19] E. Eichten, K. Gottfried, T. Kinoshita, et.al., Phys. Rev. Lett., 34, 369 (1974)

[20] H. Fritzsch, Phys. Lett. B, 86, 343 (1979); H. Fritzsch, Phys. Lett. B, 86, 164 (1979)

[21] E. Glover, et. al., Phys. Lett. B,185, 441 (1986); F. Halzen, et. al., Phys. Rev. D, 30, 700 (1984)

[22] C. Albajar, et. al., Phys. Lett. B, 256, 112 (1990); C. Albajar, et. al., Phys. Lett. B, 200, 381 (1987)

[23] F. Abe, et. al., Phys. Rev. Lett., 69, 3704 (19992)

[24] P. Nason, S. Dawson, R. K. Ellis, Nucl. Phys. B, 303, 607 (1988); P. Nason, S. Dawson, R. K. Ellis, Nucl. Phys. B, 327, 49 (1989)

[25] M. Mangano, P. Nason, G. Ridolfi, Nucl. Phys. B, 373, 295 (1992)

[26] C. Peterson, et. al., Phys. Rev. D, 27, 105 (1982)

[27] R. Rückl, Weak Decays of Heavy Flavor, Cern Print (Oct. 1983); M. Bauer, B. Stech, M. Wirbel, Z. Phys. C, 34, 103 (1987); J. Kuhn, S. Nussinov, R. Rückl, Z. Phys. C, 5, 117 (1980); J. Ellis, M. Gaillard, D. Nanopoulos, Nucl. Phys. B, 100, 313 (1975)

[28] J. Björken, SLAC-PUB-5389 (1990)

[29] D. Fakirov, B. Stech, Nucl. Phys. B, 133, 315 (1977)

[30] M. Wirbel, B. Stech, M. Bauer, Z. Phys. C,29, 637 (1985) and Z. Phys. C, 34, 103 (1987)

[31] J. Kühn, R. Rückl, Phys. Lett. B, 135, 477 (1983)

[32] P. Cox, et.al., Phys. Rev. D, 32, 1157 (1985)

[33] G. Bodwin, et. al., Phys. Rev. D, 46, 3703 (1992)

[34] H. Albrecht, et. al., Phys. Lett. B, 277, 209 (1992)

[35] E. Braaten, T. C. Yuan, Phys. Rev. Lett., 71, 1673 (1993); M. Doncheski, et. al., FermiLab-Conf-93/348-T

[36] E. Braaten, T. C. Yuan, FermiLab-Pub-94/040-T

[37] L. M. Lederman, "The Tevatron", Sci.Am., Vol.264, Num.3, p.52

[38] S. Abachi et.al., Nucl. Instr. and Meth., A338, 185 (1994)

[39] A. R. Clark et.al., Nucl. Instr. and Meth., A279, 243 (1989)

[40] A. R. Clark et.al., Nucl. Instr. and Meth., A315, 193 (1992)

[41] F. Feinstein, *Etude d'un Detecteura Rayonnement de Transition pour l'Experience DØ au FNAL*, Ph.D. thesis, A l'University de Paris-Sud, Centre d'Orsay, December 1987 (unpublished)

[42] T. Behnke, Ph.D. thesis, SUNY at Stony Brook, *The Central Drift Chamber for the DØ Experiment: Design, Construction, and Test*, August 1989 (unpublished)

[43] J. Bantly, Ph.D. thesis, Northwestern University, *The DØ Detector Forward Drift Chamber Performance and Physics Capability in the 1990 FNAL Testbeam Run*, June 1992 (unpublished)

[44] S. Abachi et.al., Nucl. Instr. and Meth., A324, 53 (1993)

[45] S. Aronson et.al., Nucl. Instr. and Meth., A269, 492 (1988)

[46] S. J. Wimpenny et.al., Nucl. Instr. and Meth., A279, 107 (1989)

[47] J. Yu, Ph.D. thesis, SUNY at Stony Brook, *Determination of the Strong Coupling Constant ($\alpha_s$) and a Test of Perturbative QCD Using W + Jets Processes in the DØ Detector*, August 1993 (unpublished)

[48] C. Brown et.al., Nucl. Instr. and Meth., A279, 331 (1989)

[49] J. Butler et.al., Nucl. Instr. and Meth., A290, 122 (1990)

[50] D. Green et.al., Nucl. Instr. and Meth., A256, 305 (1987)

[51] M. Fortner et.al., IEEE Trans. Nucl. Sci. NS-38, 480 (1991)

[52] K. Bazizi, DØ NOTE 1618 (1993)

[53] Ting Hu, DØ NOTE 1811 (1993)

[54] C. Gerber and P. Quintas, DØ NOTE 1985 (1993)

[55] S. Abachi et. al., Phys. Rev. Lett., 74, in print (1995)

[56] A. Milder and R. Astur, DØ NOTE 1657 (1993)

[57] F. Abe, et. al., FermiLab-Pub-92 (1992)

[58] M. Paterno, DØ NOTE 1782 (1993)

[59] R. Engelmann, et. al., Nuclr. Instr. and Methods, 216A, 45 (1983)

[60] F. Paige and S. Protopopescu, ISAJET 6.49: A Monte Carlo Event Generator for $pp$ and $\bar{p}p$ Interactions, FermiLab Computing Division, PM0059 (August 1992); H. Bengtsson and T.Sjöstrand, PYTHIA, The Lund Monte Carlo for Hadronic Processes, Proceedings of Snowmass '86, p.311 (1986); G. Marchesini, et. al., HERWIG: Version 5.1, Cavendish-Hep-91-26, May 1991 (unpublished)

[61] E. Eichten, et. al., Rev. Mod. Phys., 56, 579 (1984)

[62] G. Fox and S. Wolfram, Nucl. Phys. B, 168, 285 (1980)

[63] R. Field and R. Feynman, Nucl. Phys. B, 136, 1 (1978)

[64] R. Brun, et. al., CERN Program Library, GEANT 3.15 program manual

[65] J. Linnemann, "Triggering the DØ Experiment", FermiLab Meeting DPF92, Vol. 2, 1642 (19992)

[66] A. Smith, University of Arizona, "Low Meson Resonance MC Event Simulator", DØ Software

[67] G. D'Agostini, "A Multidimensional Unfolding Method Based on Bayes' Theorem", DESY 94-099, June 1994

[68] M. L. Mangano, private communications

[69] A. Smith, Ph.D. thesis, University of Arizona, *Measurement of the $\Upsilon$ and Drell-Yan Production Cross Sections at $\sqrt{s} = 1.8$ TeV Using Di-Muons*, May 1994 (unpublished)

[70] The CDF Collaboration, F. Abe et.al., Fermilab-Conf-94/134-E; Fermilab-Conf-94/141-E

[71] V. Barger and R. Phillips, "Collider Physics", Addison-Wesley Publishing Company, p.85 (1987)

[72] M. Pang et.al., DØ NOTE 2331, October 1994

[73] The OPAL Collaboration, R. Akers et.al., Phys.Lett.B, 316, 435 (1993); The ALEPH Collaboration, D. Buskulic et.al., Phys.Lett.B, 295, 174 and 396 (1992); The DELPHI Collaboration, P. Abreu et.al., Z.Phys.C, 53, 567 (1992); The CDF Collaboration, F. Abe et.al., Fermilab-Pub-94-03-E, January 1994; The OPAL Collaboration, "Measurement of the Average b-Baryon Lifetime", OPAL note PN146, July 1994

[74] The UA1 Collaboration, C. Alabajar et.al., Phys.Lett.B, 213, 405 (1988); 256, 121 (1991); The CDF Collaboration, F. Abe et.al., Phys.Rev.Lett., 68, 3403 (1992); 69, 3704 (1992); 71, 500 (1993)

[75] The CDF Collaboration, F. Abe et.al., "$J/\psi, \psi^{'} \rightarrow \mu^+\mu^-$ and $B \rightarrow J/\psi, \psi^{'}$ Cross Sections", Fermilab-Conf-94/136-E

[76] R. Demina, Ph.D. thesis, Northeastern University, $\chi_c$ *Production in* $p\bar{p}$ *Collisions at* $\sqrt{s} = 1.8\ TeV$, December 1994 (unpublished)